UQAC
Université du Québec
à Chicoutimi

Lightweight Al-based entropy alloys for elevated-temperature applications

By

Liying Cui

Under the supervision of Prof. X.-Grant Chen, co-supervision of

Prof. Zhan Zhang

Thesis presented to the University of Quebec at Chicoutimi with a view to obtaining the degree of Philosophy Doctor (Ph. D.) in Engineering

Defended on 20 February 2024

BOARD OF EXAMINERS:

Prof. Mousa Javidani, department of Applied Sciences at UQAC, President of the board of examiners

Prof. X.-Grant Chen, department of Applied Sciences at UQAC, Internal Member of examiners

Prof. Zhan Zhang, department of Applied Sciences at UQAC, Internal Member of examiners

Prof. Emad Elgallad, department of Applied Sciences at UQAC, Internal Member of examiners

Prof. Daniel Larouche, Université Laval, External Member of examiners

Québec, Canada

© Liying Cui, 2024

Résumé

Avec le développement de l'économie verte, la demande de alliages d'aluminium (Al) légers présentant un comportement mécanique supérieur à des températures élevées est en constante augmentation. Cependant, les propriétés mécaniques des alliages conventionnels d'Al peuvent se détériorer considérablement à des températures élevées en raison de la grossièreté des précipités et de la nature des alliages. L'émergence des alliages d'entropie a introduit de nouvelles stratégies de conception pour les alliages conventionnels. En intégrant le concept d'entropie dans le développement potentiel des alliages d'Al, les alliages d'entropie à base d'Al sont proposés comme des matériaux prometteurs pour obtenir à la fois des propriétés légères et résistantes. Cependant, en tant que matériaux émergents, les alliages d'entropie à base d'Al ont une courte période de développement et la recherche n'est pas encore systématique et suffisante. Par conséquent, ce projet vise à fournir un aperçu de ce domaine grâce à une enquête approfondie sur les études actuelles. Deux séries d'alliages d'entropie légers à base d'Al, avec des densités inférieures à 4,0 g/cm^3, ont été développées pour des applications à des températures élevées (≥ 300 °C). Les mécanismes de renforcement ont également été discutés plus en détail.

Dans la première partie, une revue de la littérature sur les alliages d'entropie à base d'Al est présentée. Cette revue offre un aperçu des alliages d'entropie à base d'Al légers, couvrant leur contexte de développement, les principes de conception, les méthodes de fabrication, les microstructures et les propriétés mécaniques, ainsi que les alliages adaptés aux applications à haute température. Une enquête approfondie sur la recherche actuelle sur les alliages d'entropie à base d'Al avec une densité inférieure à 4,0 g/cm^3 a été menée sur 122 alliages différents. La relation entre la microstructure et les paramètres thermodynamiques a été analysée. Les alliages d'entropie à base d'Al légers pourraient combler le fossé entre les alliages d'Al conventionnels et ceux de titane en termes de propriétés mécaniques et de densité. Les excellentes stabilités thermiques de ces alliages les rendent attractifs comme matériaux structurels pour une utilisation à des températures élevées. Enfin, les tendances futures dans le domaine des alliages d'entropie à base d'Al légers sont discutées.

Dans la deuxième partie, l'évolution microstructurale et les propriétés mécaniques de cinq alliages d'entropie légers Al-Cu-Mg-Zn ($Al_{85}Cu_5Zn_5Mg_5$, $Al_{74}Cu_{10}Zn_8Mg_8$, $Al_{93}Cu_4Zn_1Mg_1Cr_1$, $Al_{84}Cu_{10}Zn_3Mg_2Cr_1$, et $Al_{77}Cu_{17}Zn_3Mg_2Cr_1$) ont été étudiées. Les cinq alliages expérimentaux présentaient des caractéristiques légères avec des valeurs de densité allant de 2,95 à 3,63 g/cm^3 et des caractéristiques multi-phasées. Les évolutions microstructurales et de phase à des températures élevées ont été caractérisées à l'aide de diffraction des rayons X et de microscopies optique, électronique à balayage et électronique en transmission. Avec l'augmentation de la teneur en Cu, la fraction volumique des composés intermétalliques (CI) a augmenté, entraînant une limite d'élasticité améliorée et une plasticité réduite. La zone GP et les précipités fins de η' étaient des sources efficaces de renforcement dans le fcc-Al, mais ils étaient instables à 300 °C et se transformaient en particules grossières et

submicroniques. La principale source de renforcement dans la série d'alliages était le réseau de CI bien interconnecté. Parmi les cinq alliages étudiés, l'$Al_{77}Cu_{17}Zn_3Mg_2Cr_1$ présentait la limite d'élasticité la plus élevée de 588 MPa à RT et la limite d'élasticité la plus élevée de 199 MPa à 300 °C après une exposition thermique de 100 h. Compte tenu de sa haute résistance et de sa bonne stabilité thermique à 300 °C, cet alliage présente un potentiel prometteur pour des applications à des températures élevées.

Dans la troisième partie, une série d'alliages d'entropie légers à base d'Al contenant Cu, Zn, Cr, V, Ti et Fe a été conçue pour des applications à haute température. La microstructure, les propriétés mécaniques à température ambiante et élevée, et la stabilité thermique de six alliages d'entropie ($Al_{93}Cu_4Zn_1Cr_1Fe_1$, $Al_{85}Cu_{11}Zn_2Cr_1Fe_1$, $Al_{85}Cu_{11}Zn_1Cr_2V_1$, $Al_{78}Cu_{18}Zn_2Cr_1Fe_1$, $Al_{78}Cu_{18}Zn_1Cr_2Ti_1$, et $Al_{78}Cu_{18}Zn_1Cr_2V_1$) ont été étudiées. En raison de la grande différence chimique et de l'enthalpie négative élevée entre Al et les éléments d'alliage, la génération d'une grande quantité de CI était inévitable. Avec l'augmentation de la teneur en Cu, la fraction volumique des CI a augmenté de manière significative. Les trois alliages à haute teneur en Cu ($Al_{78}Cu_{18}Zn_2Cr_1Fe_1$, $Al_{78}Cu_{18}Zn_1Cr_2Ti_1$ et $Al_{78}Cu_{18}Zn_1Cr_2V_1$) présentaient des résistances à la limite d'élasticité de plus de 200 MPa et une excellente stabilité thermique à 300 °C. Ces valeurs sont considérablement supérieures à celles de la plupart des alliages d'Al conventionnels. Les mécanismes de renforcement à température ambiante et élevée ont été discutés. La stabilité thermique favorable et les bonnes propriétés mécaniques des alliages à haute teneur en Cu jusqu'à 450 °C indiquent leur potentiel significatif pour des applications à haute température.

Dans la quatrième partie, les distributions spatiales des différentes phases dans trois alliages d'entropie à base d'Al ont été étudiées. Un réseau de CI étroit composé de phases Al_2Cu et $Al_{45}Cr_7$ a été identifié. Une modélisation par éléments finis (FE) a été réalisée sur la base de la microstructure tridimensionnelle reconstruite pour simuler le comportement de déformation sous compression. Le réseau de CI a servi de principal support de contrainte pendant la déformation. Les sections minces dans le réseau de Al_2Cu étaient les sites faibles où la concentration de contrainte et les dommages se produisaient en premier. Cependant, la rupture de cette région limitée contribue à une déformation relativement coordonnée et à une plasticité étendue. La rupture de grosses particules explique la défaillance finale de l'alliage. Les résultats du modèle FE ont été comparés au comportement contrainte-déformation mesuré expérimentalement et aux propriétés mécaniques, montrant un très bon accord. Étant donné la distribution non uniforme de la déformation et de la contrainte pendant la déformation, un modèle de renforcement, combinant les modèles Voigt et Reuss, a également été développé pour prédire les propriétés mécaniques des alliages d'entropie à base d'Al dans le but de faciliter le développement des alliages d'entropie à base d'Al.

Abstract

With the development of the green economy, there is a growing demand for lightweight aluminum (Al) alloys exhibiting superior mechanical behavior at elevated temperatures. Nevertheless, the mechanical properties of conventional Al alloys often suffer significant deterioration at high temperatures due to coarsened precipitates and inherent alloy characteristics. The advent of entropy alloys has introduced novel design strategies for conventional alloys. By integrating the concept of entropy into the potential development of Al alloys, Al-based entropy alloys are proposed as promising materials for achieving both lightweight and high-strength properties. However, as emerging materials, Al-based entropy alloys have a limited development history, and research in this area is not yet systematic or sufficient. Therefore, this project aims to provide a comprehensive overview through an in-depth investigation in this field. Two series of lightweight Al-based entropy alloys have been developed for elevated-temperature (≥ 300 °C) applications. The strengthening mechanisms employed in these alloys have been further discussed.

In the first part, a literature review on the Al-based entropy alloys is presented. This review provides an overview of lightweight Al-based entropy alloys, covering their developmental background, design principles, fabrication methods, microstructures, and mechanical properties, as well as alloys suitable for high-temperature applications. A comprehensive investigation of current research on Al-based entropy alloys with a density lower than 4.0 g/cm^3 was conducted from 122 different alloys. The relationship between microstructure and thermodynamic parameters was analyzed. Lightweight Al-based entropy alloys could bridge the gap between conventional Al and Ti alloys in terms of mechanical properties and density. The excellent thermal stabilities of these alloys make them attractive structural materials for use at elevated temperatures. Finally, future trends in the field of lightweight Al-based entropy alloys are discussed.

In the second part, the microstructural evolution and mechanical properties of five lightweight Al–Cu–Mg–Zn entropy alloys ($Al_{85}Cu_5Zn_5Mg_5$, $Al_{74}Cu_{10}Zn_8Mg_8$, $Al_{93}Cu_4Zn_1Mg_1Cr_1$, $Al_{84}Cu_{10}Zn_3Mg_2Cr_1$, and $Al_{77}Cu_{17}Zn_3Mg_2Cr_1$) were investigated. The five experimental alloys revealed lightweight characteristics with density values ranging from 2.95 to 3.63 g/cm^3 and multiphase features. The microstructural and phase evolutions at elevated-temperature were characterized using X-ray diffraction and optical, scanning, and transmission electron microscopy. With the increase in Cu, the volume fraction of intermetallic compounds (ICs) increased, resulting in an improved yield strength (YS) and reduced plasticity. The GP zone and fine η' precipitates were effective strengthening sources in fcc-Al, but they were unstable at 300 °C and transformed into coarse and submicron-sized particles. The main source of strengthening in the alloy series was the well-interconnected intermetallic compound (IC) network. Among the five alloys studied, $Al_{77}Cu_{17}Zn_3Mg_2Cr_1$ exhibited the highest YS of 588 MPa at room temperature and retained the highest YS of 199 MPa at 300 °C after thermal exposure for 100 h. Combining its high strength and good thermal

stability at 300 °C, this alloy exhibits promising potential for elevated-temperature applications.

In the third part, a series of lightweight Al-based entropy alloys containing Cu, Zn, Cr, V, Ti and Fe has been designed for elevated temperature applications. The microstructure, mechanical properties at room and elevated temperatures, and the thermal stability of six entropy alloys ($Al_{93}Cu_4Zn_1Cr_1Fe_1$, $Al_{85}Cu_{11}Zn_2Cr_1Fe_1$, $Al_{85}Cu_{11}Zn_1Cr_2V_1$, $Al_{78}Cu_{18}Zn_2Cr_1Fe_1$, $Al_{78}Cu_{18}Zn_1Cr_2Ti_1$, and $Al_{78}Cu_{18}Zn_1Cr_2V_1$) were investigated. Owing to the large chemical difference and high negative enthalpy between Al and the alloying elements, the generation of a large quantity of ICs was inevitable. With increasing Cu content, the volume fraction of ICs increased significantly. The three high-Cu alloys ($Al_{78}Cu_{18}Zn_2Cr_1Fe_1$, $Al_{78}Cu_{18}Zn_1Cr_2Ti_1$, and $Al_{78}Cu_{18}Zn_1Cr_2V_1$) exhibited high yield strengths of more than 200 MPa and excellent thermal stability at 300 °C. These values are considerably superior to those of most conventional aluminum alloys. The strengthening mechanisms at room and elevated temperatures have been discussed. The favorable thermal stability and good mechanical properties of the high-Cu alloys up to 450 °C indicate their significant potential for high-temperature applications.

In the fourth part, the spatial distributions of various phases in three Al-based entropy alloys were investigated. A closely IC network comprising Al_2Cu and $Al_{45}Cr_7$ phases was identified. Finite element (FE) modeling was conducted based on the reconstructed three-dimensional microstructure to simulate compressive deformation behavior. The IC network served as the main stress bearer during deformation. Thin sections in the Al_2Cu network were the weak sites where stress concentration and damage first occurred. However, the breakage of this limited region contributes to relatively coordinated deformation and extended plasticity. The breakage of large particles accounts for the final alloy failure. The results of the FE model were compared with the experimentally measured stress-strain behavior and mechanical properties, showing very good agreement. Given the non-uniform distribution of strain and stress during deformation, a strengthening model, merging the Voigt and Reuss models, was also developed to predict the mechanical properties of Al-based entropy alloys with the aim of facilitating Al-based entropy alloy development.

Table of Contents

Résumé iii
Abstract v
Table of Contents vii
List of Tables x
List of Figures xi
List of Symbols xv
List of Abbrevations xviii
Dedication xx
Acknowledgements xxi

Chapter 1
Introduction 1
1.1 Background 1
1.2 Problem statement 4
1.3 Objectives 5
1.4 Originality statement 6
1.5 Thesis outlines 7
References 9

Chapter 2
Literature review: Lightweight Al-based entropy alloys – Overview and future trend 12
Abstract 12
2.1 Introduction 13
2.2 Concepts, design, and fabrication methods 15
2.2.1 Key concepts in entropy alloys 15
2.2.2 Design methods 19
2.2.3 Fabrication methods 23
2.3 Microstructure and mechanical properties 26
2.3.1 Microstructural characteristics of lightweight Al-based entropy alloys 26
2.3.2 Mechanical properties of lightweight Al-based entropy alloys 31
2.4 Al-based entropy alloys for elevated-temperature applications 35

2.4.1 Commonly studied alloy systems 35
2.4.2 Microstructural characteristics at elevated temperatures 37
2.4.3 Mechanical properties at elevated temperatures and thermal stability 38
2.5 Potential of machine learning in lightweight Al-based entropy alloys 40
2.6 Future trends and prospects 44
2.6.1 High-strength-orientated alloy design strategy 44
2.6.2 Computer-assisted techniques for alloy development 47
2.6.3 Lightweight Al-based entropy alloys for elevated temperature applications 47
2.7 Conclusion and remarks 48
References 49

Chapter 3

Microstructure and mechanical properties of novel Al–Cu–Mg–Zn lightweight entropy alloys for elevated-temperature applications 60
Abstract 60
3.1 Introduction 61
3.2 Experimental procedures 63
3.3 Results and discussion 65
3.3.1 Microstructure and phase formation of as-cast alloys 65
3.3.2 Mechanical performance at room and elevated temperatures 69
3.3.3 Evolution of the microstructures during thermal exposure 73
3.3.4 Role of the IC network on strengthening 77
3.3.5 Comparison of the strength and density data for various aluminum alloys 80
3.4 Conclusions 84
References 86

Chapter 4

Development of lightweight Al-based entropy alloys for elevated temperature applications 91
Abstract 91
4.1 Introduction 92
4.2 Experimental procedures 95
4.3 Results 97

4.3.1 Microstructures and phase constituents 97
4.3.2 Mechanical properties and thermal stability 105
4.4 Discussion 108
4.4.1 Thermodynamic parameters and phase formation 108
4.4.2 Relationship between mechanical behavior and microstructure 112
4.4.3 Comparison of elevated temperature strength for various aluminum alloys 119
4.5 Conclusions 122
References 123

Chapter 5

Spatial reconstruction, microstructure-based modeling of compressive deformation behavior, and prediction of mechanical properties in lightweight Al-based entropy alloys 128
Abstract 128
5.1 Introduction 129
5.2 Materials and experimental procedure 132
5.3 Results and discussion 135
5.3.1 Microstructural characterization from 3D visualization 135
5.3.2 FE simulation of compression tests 137
5.3.3 Structural efficiency of IC network 142
5.3.4 Damage of IC network 145
5.3.5 Strengthening model of Al-based entropy alloys 148
5.4 Conclusions 153
References 154

Chapter 6

General conclusions and recommendations 159
6.1 General conclusions 159
6.2 Recommendations 161

List of publications 163

List of Tables

Table 2.1 Summary of commonly used parameters in HEAs. 20

Table 3.1 Chemical compositions of five experimental alloys. 64

Table 3.2 Chemical composition and volume fraction of each phase in the as-cast alloys. 68

Table 3.3 Physical properties of intermetallic phases in as-cast Alloys 1–5. 69

Table 4.1 Chemical compositions of experimental alloys. 96

Table 4.2 The phase type, volume fraction and phase composition in the corresponding microstructure regions of Fig. 4.4. 104

Table 4.3 Room-temperature compressive mechanical properties of the as-cast alloys. 105

Table 4.4 Thermodynamic parameters and mixing density of the experimental alloys. 111

Table 4.5 Quantification results of θ' precipitates after thermal exposure. 117

Table 4.6 Comparison of the YS at 300-315 °C (MPa) between various aluminum alloys. 121

Table 5.1 Chemical compositions of the experimental alloys (at.%). 132

Table 5.2 Volume fraction of each phase from 3D reconstruction in Figs. 5.4–5.6 and compared to 2D quantification. 137

Table 5.3 Parameters used for the FE simulation [36-40, 42-44]. 141

Table 5.4 Experimental and simulated strengths of Alloys 1–3. 142

Table 5.5 Predicted strengths and their deviations with experimental data using Eqs. 8–9 in Alloys 1–3. 153

List of Figures

Fig. 1.1 Rising trend of alloy chemical complexity versus time [9]. Copyright 2017, Springer. 2

Fig. 2.1 Distribution of parameters δ and Ω in HEAs having various phase formation, wherein, S and I indicate the alloys comprise only SS and ICs, respectively; and S+I indicates the simultaneous existence of both SS and ICs; B indicates the alloys include bulk metallic glasses (BMGs) [56]. Copyright 2011, Elsevier. 21

Fig. 2.2 The usage of (a) fabrication methods and (b) constituent elements in 122 Al-based entropy alloys. 25

Fig. 2.3 Microstructure classification by (a) phase type and (b) number of phases (SS, ICs, and SS+ICs indicate the alloys comprise only SS, only ICs, and the combination of SS and ICs, respectively; 1-phase indicates the alloys only comprise 1 phase, 2-phase indicates the alloys only comprise 2 phases, and so on). 28

Fig. 2.4 The number of occurrences of the 10 most frequently occurring phases. 28

Fig. 2.5 Phase formation vs. thermodynamics parameters of Al-based entropy alloys. The size of bubble in Fig. 2.5c-d represents the magnitude of Ω. 30

Fig. 2.6 Distribution of strengths of Al-based entropy alloys at RT. 33

Fig. 2.7 (a) Ashby diagram of strength vs. density for various materials at RT [96], Copyright 2011, Elsevier, and (b) locally enlarged diagram with modification to the upper limits of YS for conventional Al and Ti alloys. 35

Fig. 2.8 SEM images of (a-c) as-cast and (d-f) 300 °C/100 h thermally exposed alloys: (a, d) $Al_{93}Cu_4Zn_1Cr_1Fe_1$, (b, e) $Al_{85}Cu_{11}Zn_1Cr_2V_1$, (c, f) $Al_{78}Cu_{18}Zn_1Cr_2V_1$. Wherein, the red marks A-D stand for different phase component: A is fcc-Al, B is Al_2Cu, C is $Al_{45}Cr_7$, and D is Al_7Cu_2Fe [16]. Copyright 2022, Elsevier. 38

Fig. 2.9 YS vs. density of Al-based entropy alloys and conventional Al alloys at (a) ambient temperature, (b) 300 °C, and (c) 300 °C after thermal exposure [81]. Copyright 2023, Elsevier. 40

Fig. 2.10 Machine learning workflow in the field of alloy design [112]. Copyright 2022, Elsevier. 43

Fig. 2.11 Commonly used machine learning algorithms in materials science [113]. Copyright 2017, Elsevier. 44

Fig. 3.1 XRD patterns of as-cast alloys: (a) Alloy 1, (b) Alloy 2, (c) Alloy 3, (d) Alloy 4, and (e) Alloy 5. 66

Fig. 3.2 SEM backscattered electron images of the as-cast alloys: (a) Alloy 1, (b) Alloy 2, (c) Alloy 3, (d) Alloy 4, and (e) Alloy 5. 67

Fig. 3.3 Room-temperature mechanical properties: (a) true stress–strain curves and (b) YS and IC contents of the as-cast alloys. 70

Fig. 3.4 Mechanical properties of the as-cast alloys at 300 °C: (a) true stress–strain curves and (b) yield and maximum strengths. 71

Fig. 3.5 (a) Microhardness of alloys at room temperature with various exposure times, (b) compressive strengths at 300 °C after 300 °C/100 h exposure, and (c) percentages of HV and YS reduction after 300 °C/100 h exposure vs. the content of fcc-Al. 72

Fig. 3.6 Bright-field TEM images showing η′ precipitates in fcc-Al along $<001>_{Al}$: (a) as-cast Alloy 1, (b) as-cast Alloy 3, and (c) DSC curves of as-cast Alloys 1–5. 74

Fig. 3.7 Bright-field TEM images of fcc-Al in (a, b) Alloy 1, (c, d) Alloy 3, (a, c) after thermal exposure for 5 h and (b, d) after thermal exposure for 100 h at 300 °C. 75

Fig. 3.8 XRD patterns and SEM backscattered electron images after 300 °C/100 h exposure: (a, d) Alloy 1, (b, e) Alloy 2, and (c, f) Alloy 5. 76

Fig. 3.9 Yield strengths of Alloys 1–5 at 300 °C as a function of the content of ICs. 77

Fig. 3.10 3D phase distribution in as-cast Alloy 4: (a) all phases, (b) Al_2Cu phase, (c) $Al_{45}Cr_7$ phase, and (d) integrated IC network. 79

Fig. 3.11 3D phase distribution in as-cast Alloy 5: (a) all phases, (b) Al_2Cu phase, (c) $Al_{45}Cr_7$ phase, and (d) integrated IC network. 80

Fig. 3.12 Comparison of the YS and density of Al-based entropy alloys and conventional Al alloys at (a) room temperature, (b) 300 °C, and (c) 300 °C after thermal exposure for 100 h. 83

Fig. 4.1 Calculated equilibrium phase diagrams showing the mole fraction of all phases as a function of temperature: (a) Alloy 1, (b) Alloy 2, (c) Alloy 3, (d) Alloy 4, (e) Alloy 5 and (f) Alloy 6. 99

Fig. 4.2 Simulated phase formation using Scheil's model showing the mole fraction of all phases as a function of temperature: (a) Alloy 1, (b) Alloy 2, (c) Alloy 3, (d) Alloy 4, (e) Alloy 5 and (f) Alloy 6. 100

Fig. 4.3 XRD patterns of the as-cast alloys: (a) Alloy 1, (b) Alloy 2, (c) Alloy 3, (d) Alloy 4, (e) Alloy 5 and (f) Alloy 6. 101

Fig. 4.4 SEM images of the as-cast microstructure: (a) Alloy 1, (b) Alloy 2, (c) Alloy 3, (d) Alloy 4, (e) Alloy 5 and (f) Alloy 6. 104

Fig. 4.5 Room-temperature compressive stress-strain curves of the as-cast alloys. . 105

Fig. 4.6 Compressive mechanical properties of the as-cast alloys at 300 °C, (a) true stress-strain curves and (b) yield strength and maximum compressive strength. 106

Fig. 4.7 Compressive mechanical properties at 300 °C for the samples after thermal exposure at 300 °C/100 h, (a) true stress-strain curves and (b) yield strength and maximum compressive strength. 107

Fig. 4.8 Evolution of maximum compressive strength and yield strength of as-cast and thermally exposed Alloy 5 as a function of test temperature. 108

Fig. 4.9 SEM images of as-cast (a) Alloy 1 and (b) Alloy 4 after room-temperature compression tests. 114

Fig. 4.10 Linear relationship between the YS at 300 °C and the volume fraction of ICs. 115

Fig. 4.11 Bright-field TEM images of after thermal exposure at 300 °C/100 h and compression test at 300 °C, (a) Alloy 5 and (b) Alloy 1. 115

Fig. 4.12 SEM images of the thermally exposed alloys: (a) Alloy 1, (b) Alloy 3, (c) Alloy 6, (d) an enlarged view showing precipitates in the fcc-Al phase of Alloy 6. 116

Fig. 4.13 DSC heating curves of as-cast Alloys 4-6 showing no phase transformation until the melting point (~523 °C). 119

Fig. 5.1 SEM images of (a) Alloy 1, (b) Alloy 2, and (c) Alloy 3. 134

Fig. 5.2 Corresponded images of Fig. 1 processed by ImageJ software to assign a uniform color to each phase, (a) Alloy 1, (b) Alloy 2, and (c) Alloy 3. 134

Fig. 5.3 Flow chart for the 3D reconstruction and numerical simulation process. ... 135

Fig. 5.4 3D phase distribution in Alloy 1: (a) all phases, (b) Al_2Cu and $Al_{45}Cr_7$ phases, and (c) Al_2Cu phase. 136

Fig. 5.5 3D phase distribution in Alloy 2: (a) all phases, (b) Al_2Cu and $Al_{45}Cr_7$ phases, and (c) Al_2Cu phase. 136

Fig. 5.6 3D phase distribution in Alloy 3: (a) all phases, (b) Al_2Cu and $Al_{45}Cr_7$ phases, and (c) Al_2Cu phase. 137

Fig. 5.7 FE modeling assembly for Alloy 2, where the purple, yellow, and cyan regions representing the fcc-Al, Al_2Cu, and $Al_{45}Cr_7$ phases, respectively. 141

Fig. 5.8 True strain-stress curves of experimental and simulation results of Alloys 1–3. 142

Fig. 5.9 Distribution of local stress in Alloy 1 at a total strain of 3%: (a) all phases, (b) Al_2Cu and $Al_{45}Cr_7$ phases, and (c) Al_2Cu phase. 143

Fig. 5.10 (a) Compression simulation on single fcc phase and (b) simulated true strain-stress curves of overall phases and single fcc-Al phase in Alloy 1 144

Fig. 5.11 Distribution of local stress in Alloy 3 of fcc-Al and Al_2Cu phases at a total strain of (a) 0.5%, (b) 0.7%, and (c) 0.9 %. The green and red colors represent the Al_2Cu phase, and the remaining blue and cyan regions correspond to the fcc-Al phase. 145

Fig. 5.12 Distribution of (a) local stress at a total strain of 1% and (b) local strain at a total strain of 1.1% of the Al_2Cu phase in Alloy 1.....146

Fig. 5.13 SEM images of broken particles in the deformed Alloy 1.....147

Fig. 5.14 Distribution of local strain of (a, c) Al_2Cu and (b, d) $Al_{45}Cr_7$ phases in Alloy 3 at a total strain of (a, b) 0.05% and (c, d) 1.7%. 148

Fig. 5.15 (a) YS and (b) compressive strengths calculated from the Reuss and Voigt models and obtained from experimental results.....151

Fig. 5.16 Distribution of local strain of fcc-Al phase at yield point of (a) Alloy 1, (b) Alloy 2, and (c) Alloy 3. 152

List of Symbols

Al	Aluminum
Cu	Copper
Mg	Magnesium
Zn	Zinc
Fe	Iron
Cr	Chromium
Si	Silicon
Mn	Manganese
Sn	Tin
Ti	Titanium
V (element)	Vanadium
Zr	Zirconium
Sc	Scandium
Ni	Nickle
La	Lanthanum
Co	Cobalt
Y	Yttrium
Ag	Silver
B	Boron
Ce	Cerium
Be	Beryllium
N	Nitrogen
O	Oxygen
C	Carbon
Ca	Calcium
℃	temperature unit on Celsius scale
K	temperature unit on Kelvin scale

J	energy unit of joule
kJ	kilojoule
mol	mole
%	percentage
wt.%	weight percentage
at.%	atomic percentage
vol.%	volume fraction
MPa	pressure unit of megapascal
GPa	pressure unit of gigapascal
h	hour
min	minute
s	second
g	gram
cm	centimeter
mm	millimeter
μm	micrometer
nm	nanometer
V (unit)	voltage
kV	kilovolt
ml	milliliter
HV	unit of Vickers hardness
θ″	theta double prime phase
θ′	theta prime phase
θ	equilibrium theta phase
η’	eta prime phase
η	equilibrium eta phase
fcc-Al	matrix of aluminum
T_m	absolute melting temperature

T_{mix}	mixing melting temperature
ΔT_{mix}	mixing melting temperature difference
ρ_{mix}	theoretical density
ΔS_{mix}	mixing entropy
ΔH_{mix}	mixing enthalpy
Ω	ratio of entropy to enthalpy
δ	atomic size difference
$\Delta\chi$	electronegativity difference
c_i	atomic percentages of the i^{th} element
c_j	atomic percentages of the j^{th} element
σ_y	yield strength
σ_{max}/ σ_m	compressive strength
ε_{max}	maximum strain
K_{IC}	fracture toughness
f_v	volume fraction
$\Delta\sigma_{SS}$	solid solution strengthening
σ_p	precipitation strengthening
N_v	number density
t_t	effective thickness
d_t	effective width
b	Burger's vector
ν	Poisson's ratio
G	shear modulus.
F	degree of freedom
C	number of elements
P	number of phases
R	ideal gas constant
M	Taylor factor

List of Abbrevations

OM	optical microscopy
SEM	scanning electron microscopy
TEM	transmission electron microscopy
EDS	energy-dispersive X-ray spectroscopy
DSC	Differential scanning calorimetry
XRD	X-ray diffraction
SADP	selected area diffraction pattern
HEAs	high-entropy alloys
MEAs	medium-entropy alloys
LEAs	low-entropy alloys
SS	solid solution
FCC	face-centered cubic
HCP	hexagonal close-packed
BCC	body-centered cubic
BMGs	bulk metallic glasses
VEC	valance electron concentration
GP	Guinier Preston
YS	yield strength
HT	high-throughput
ML	machine learning
CALPHAD	Calculation of Phase Diagrams
IC	intermetallic
ICs	intermetallic compounds
3D	three-dimensional
2D	two-dimensional

HTs	high temperatures
RT	room temperature
FE	finite element
FEM	finite element method
RVE	representative volume element

Dedication

I dedicate this thesis to my respectful parents, Mengzhong Cui and Lingshuang Qin, and my brother Licheng Cui and my sister-in-law Linlin Ma, for their unwavering support and encouragement throughout my life.

At the same time, I extend a special dedication to my beloved husband, Peng Hu. Without his constant inspiration and unwavering support, both spiritually and academically, this work would not have been possible.

Acknowledgements

I would like to express my sincere gratitude to everyone who has helped, encouraged, and supported me during my Ph.D. journey at the University of Quebec at Chicoutimi (UQAC).

First and foremost, I would like to convey my deepest gratitude to my supervisor, Prof. X.-Grant Chen, for offering me the opportunity to pursue my studies in Canada. I also extend profound appreciation for his continuous trust, invaluable guidance, and unwavering support. His insightful expertise, innovative thinking, and rigorous academic attitude will always be a lasting influence on my academic journey.

Secondly, I would like to extend my deepest thanks to my co-supervisor Prof. Zhan Zhang, for inspiring me to explore new possibilities and encouraging me to overcome difficulties. His consistent guidance, inspiration, and timely assistance have played a pivotal role in the successful completion of my Ph.D. research.

My deep appreciation also goes to Prof. Kun Liu for his scientific insights, technical support, and generous allocation of time. His contributions were instrumental in bringing my side project on Al-Cu hot-rolled alloys to a fruitful achievement.

I am deeply grateful to Prof. Emad Elgallad, Prof. Duygu Kocaefe, Prof. Dilip Sarkar, and Prof. Mousa Javidani for their warm assistance and whole-hearted support in providing technical guidance and engaging in scientific discussions.

I am also indebted to the dedicated technicians, Mr. Samuel Dessureault and Mr. Félix Tremblay, whose unwavering technical support has greatly contributed to the conduction of my Ph.D. research. Additionally, I extend my gratitude to Mr. Zhixing Chen for his help during the TEM sample preparation and observation.

I sincerely thank all my colleagues working alongside me at CURAL. Their collaborative efforts, scientific insights, and positive life attitude have greatly enriched my Ph.D. journey in Chicoutimi. I would like to mention Jovid Rakhmonov, Abhishek Ghosh, Mohammadreza Mofarrehi, Siamak Nikzad Khangholi, Ahmed Y. Al-Gendy, Ali Elashery, Mohamed Qassem, Mohamed Ahmed, Peng Hu, Mohammad Khoshghadam, Alyaa Aly, Chaima Hajji, Zimeng Wang, Shuai Wang, Cong Li, Dong Li, Esmaeil Pourkhorshid, Quan Shao, Farnaz Yavari, Behrouz Abnar, Ali Faraj, Layla Mohammadzadeh, Musa Muhammed, Siavash Imanian Ghazanlou, and Eric Kojo Kweitsu.

I would like to acknowledge the financial support of the Natural Sciences and Engineering Research Council of Canada (NSERC) and Rio Tinto Aluminum through the Research Chair in the Metallurgy of Aluminum Transformation at University of Quebec at Chicoutimi.

Best for last, I wish to reiterate my profound gratitude to my family members, friends, and my husband Peng Hu. Thank you all for being with me all the time!

Chapter 1

Introduction

1.1 Background

With the development of the green economy, the demand for lightweight materials has increased in many fields, such as transportation, construction, aerospace, etc. A lot of emphasis has been given to the lightweight structural components, which have a lower cost, higher strength, and longer service life [1-3]. Aluminum (Al) is one of the lightest metals and its alloys are widely adopted because of their light weight, moderate cost, and good mechanical performance including specific stiffness, specific strength, ductility, and fracture toughness [4]. There is a strong need for lightweight Al alloys served at high temperatures (HTs), for instance, the internal combustion engine pistons, cylinder heads, and heat exchangers in the aerospace and automobile fields to reduce part weight and cost. Although several Al structural alloys meet the high-strength criteria at room temperature (RT), the general low strength of the Al alloys at HTs significantly limits their widespread applications. For example, the elevated temperature strengths of a typical high-strength 7075 aluminum alloy at 200 ℃ and 300 ℃ are approximately 30 % and 10 % of its RT strengths, respectively [5]. To further advance lightweight Al alloys for elevated temperature applications, two requirements are essential: (1) enhanced strength at HTs and (2) maintenance of excellent thermal stability during the prolonged HT service [6].

For thousands of years, practical alloy systems have typically been based on one or two principal elements. To break this limitation, Yeh et al. [7] and Cantor et al. [8]

introduced multi-principal elements in the alloy and proposed an entirely new class of alloys coined as high-entropy alloys (HEAs) in 2004, as illustrated in Fig. 1.1 [9]. The design concept behind HEAs is to obtain a high entropy value by adding multiple principal elements in equal or near-equal atomic ratios to facilitate the formation of disordered solid solution (SS) and endow the alloys with unique properties [10, 11], especially outstanding mechanical properties [12, 13].

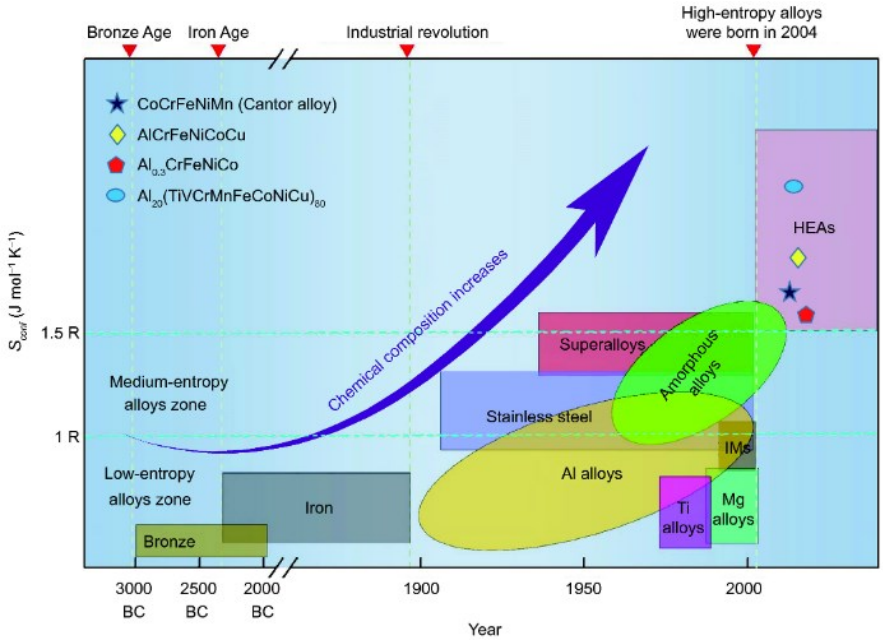

Fig. 1.1 Rising trend of alloy chemical complexity versus time [9]. Copyright 2017, Springer.

Among different types of HEAs, lightweight HEAs have attracted much attention for transportation and energy-saving reasons and potential outstanding mechanical and physical properties. However, the density of lightweight HEAs usually above 6 g/cm^3 [14, 15], which is much higher compared to Al alloys. To further reduce the density of lightweight HEAs, the content of heavy elements may decrease while the proportion of light element Al may increase.

Over the years, the concept of HEAs has expanded and it motivates the development of entropy alloys, including high-entropy, medium-entropy, and low-entropy alloys, and many of them possess good performance from various aspects [16-19]. Meanwhile, the phase formation of entropy alloys is not limited solely to a single SS phase [16].

Combining the concept of entropy with the potential development of Al alloys, Al-based entropy alloys are proposed as promising materials for achieving both lightweight and high-strength properties. Yang et al. [20] reported two Al-based entropy alloys $Al_{80}Li_5Mg_5Zn_5Sn_5$ and $Al_{80}Li_5Mg_5Zn_5Cu_5$, consisting of fcc-Al and intermetallic compounds (ICs) such as Al_2Cu, $AlCu_3$, Mg_2Sn, Li_2MgSn and Sn. These alloys exhibited a low density of approximately 3 g/cm^3 and a high compressive fracture strength of >830 MPa with a plasticity of >16%. Another example is $Al_{55}(TiVCr)_{45}$, which consisted of two SS phases and one intermetallic compound (IC) phase, reported to exhibit a high yield strength of 825 MPa with a large uniform strain of 25.8% [21].

The favorable mechanical properties of Al-based entropy alloys at RT indicate their potential for high-temperature applications, offering a novel approach to improving the mechanical properties of Al alloys at elevated temperatures. Therefore, this project aims to develop a series of Al-based entropy alloys for elevated-temperature applications.

1.2 Problem statement

The field of Al-based entropy alloys is relatively new, with the earliest report on this topic dating back to 2014 [20]. Due to the limited development time, current research lacks systematic exploration. The existing reports on Al-based entropy alloys are varied, lacking a systematic review and analysis across various aspects such as manufacture methods, phase composition, properties, and future development trends, etc.

There are basically two design approaches for Al-based entropy alloys, empirical thermophysical parameters method and Calculation of Phase Diagrams (CALPHAD) molding [22]. Both need experimental databases. However, due to the limited studies in this field, the database is incomplete. Meanwhile, Al-based entropy alloys could exhibit poor liquidity and castability due to the high concentration of multiple elements [23]. Appropriate alloy design strategy should be adopted to address this issue.

Currently, the emphasis in research predominantly centers on the mechanical behavior of alloys at RT, while their performance at higher temperatures is seldom investigated. In the meantime, for Al-based entropy alloys, secondary phases commonly appear, sometimes constituting a significant portion of the alloy [24]. However, their role in strengthening is not fully considered. There is a need for comprehensive exploration and analysis of how these secondary phases act in Al-based entropy alloys during deformation. Furthermore, the strengthening mechanisms in Al-based entropy alloys remains inadequately discussed.

1.3 Objectives

The general objective of this project is to develop lightweight Al-based entropy alloys that can be used for elevated-temperature applications (≥ 300 °C). To achieve this goal, 3 parts of specific objectives have been defined and listed as follows:

Part 1: Design of lightweight Al-based entropy alloys

a. Develop several series of alloys based on appropriate design approaches, including empirical thermophysical parameters method and CALPHAD molding.
b. Adopt high-melting point elements for the good of the potential elevated-temperature properties.
c. Control the designed lightweight alloys with a density less than 4.0 g/cm^3.

Part 2: Casting and characterization

a. Explore suitable casting procedure. Entropy alloys usually possess weak liquidity, castability, and considerable compositional inhomogeneity, due to their multiple elements with high concentrations. Therefore, their casting is usually more difficult than that of conventional Al alloys. Exact casting procedures for this project were developed.
b. Evaluate mechanical behaviors of the experimental alloys through hardness test and compression test at RT (20 °C) and HTs (≥ 300 °C).
c. Analyze phase constitution, microstructure characteristics in as-cast and thermally exposed alloys.

Part 3: Investigation on strengthening mechanisms

a. Study the relationship between mechanical behaviors and microstructure.

b. Reconstruct three-dimensional (3D) microstructure of the experimental.

c. Conduct mechanical simulations by incorporating the actual 3D morphologies and explore an intuitive strengthening model to predict the strengths of Al-based entropy alloys.

d. Provide a systematic review of the current findings in the filed of Al-based entropy alloys combining with the experimental results in the project, with the intention of presenting existing regulations and emphasizing the future trend.

1.4 Originality statement

1) Two Groups, a total of 11 lightweight Al-based entropy alloys with densities ranging from 2.95 to 3.74 g/cm^3 were developed for the first time.

2) The elevated-temperature properties and the thermal stability of the entropy alloys were systematically investigated.

3) ICs network was reconstructed through three-dimensional visualization, and its support role was emphasized. The strengthening mechanisms in the experimental alloys were proposed and analyzed.

4) A finite element simulation was conducted using microstructure-based modeling to study the compressive behavior of lightweight Al-based entropy alloys. A practical strengthening model was developed to predict the strengths of these alloys.

5) A comprehensive summary on the empirical thermophysical parameters and phase formation was made based on the experimental results combined with current findings reported in the references.

1.5 Thesis outlines

The current Ph.D. thesis consists of six parts.

Chapter 1 provides a concise background of the project and highlights current challenges in this field. Additionally, it outlines the objectives, originality, and structure of this thesis.

Chapter 2 presents a literature review "Lightweight Al-based entropy alloys: Overview and future trend", published in Science China Materials (2024, https://doi.org/10.1007/s40843-023-2699-2). The review involved a thorough investigation of 122 existing Al-based entropy alloys with a density lower than 4.0 g/cm^3, incorporating the 11 alloys developed in this project, as detailed in Chapters 3 and 4. It provided an overview of the current studies of lightweight Al-based entropy alloys and discussed the future trends in this field.

Chapter 3 highlights the investigation "Microstructure and mechanical properties of novel Al–Cu–Mg–Zn lightweight entropy alloys for elevated-temperature applications", published in Materials Characterization (2023, https://doi.org/10.1016/j.matchar.2023.112927). The first series Al-based entropy alloys in this project: five lightweight Al–Cu–Mg–Zn alloys ($Al_{85}Cu_5Zn_5Mg_5$,

$Al_{74}Cu_{10}Zn_8Mg_8$, $Al_{93}Cu_4Zn_1Mg_1Cr_1$, $Al_{84}Cu_{10}Zn_3Mg_2Cr_1$, and $Al_{77}Cu_{17}Zn_3Mg_2Cr_1$) were developed. Their microstructure evolution, mechanical behavior at both RT and 300 °C, and the strengthening mechanisms were investigated. Because the simultaneous addition of Mg and Zn gave rise to primary secondary phase $MgZn_2$, which was not thermal stable, and precipitates η', which immediately dissolved into fcc-Al at HTs. In the subsequent alloy development in Chapter 4, Mg was no longer added, so as to further improve the thermal stability of alloys.

Chapter 4 shows the research "Development of lightweight Al-based entropy alloys for elevated temperature applications", published in Journal of Alloys and Compounds (2023, https://doi.org/10.1016/j.jallcom.2022.168619). The second series Al-based entropy alloys in this project: six lightweight Al–Cu–Zn–Cr entropy alloys ($Al_{93}Cu_4Zn_1Cr_1Fe_1$, $Al_{85}Cu_{11}Zn_2Cr_1Fe_1$, $Al_{85}Cu_{11}Zn_1Cr_2V_1$, $Al_{78}Cu_{18}Zn_2Cr_1Fe_1$, $Al_{78}Cu_{18}Zn_1Cr_2Ti_1$, and $Al_{78}Cu_{18}Zn_1Cr_2V_1$) were designed for elevated temperature applications. The microstructures were thermally stable at HTs. The three high-Cu alloys ($Al_{78}Cu_{18}Zn_2Cr_1Fe_1$, $Al_{78}Cu_{18}Zn_1Cr_2Ti_1$, and $Al_{78}Cu_{18}Zn_1Cr_2V_1$) exhibited high yield strengths of more than 200 MPa at 300 °C and excellent thermal stability up to 450 °C. Among the six alloys, an increase in Cu content led to a significant rise in the volume fraction of ICs, and it was qualitatively concluded that a higher content of ICs could result in increased strength and reduced plasticity. In order to quantitively explore the strengthening role of ICs, the compressive behavior of the alloys was investigated through finite element modeling in Chapter 5.

Chapter 5 shows the research "Three-dimensional visualization and microstructure-based modeling of compressive behavior in lightweight Al-based

entropy alloys", which is under submission. Three Al-based entropy alloys ($Al_{93}Cu_4Zn_1Cr_1Fe_1$, $Al_{85}Cu_{11}Zn_2Cr_1Fe_1$, and $Al_{78}Cu_{18}Zn_2Cr_1Fe_1$) with different ICs content were chosen from the second series alloys reported in Chapter 4. The spatial distribution of various phases in these alloys was reconstructed. The finite element modeling was conducted based on the actual microstructure. Structural efficiency and damage analysis of IC network were discussed. Finally, a practical strengthening model was provided to quantitively predict the strengths of Al-based entropy alloys.

In Chapter 6, the general conclusions and recommendations for the future work were drawn. Subsequent to the primary chapters, a list of publications is provided.

References

[1] D. Raabe, C.C. Tasan, E.A. Olivetti, Strategies for improving the sustainability of structural metals, Nature, 575(7781) (2019) 64-74. https://doi.org/10.1038/s41586-019-1702-5

[2] J. Hirsch, Aluminium in innovative light-weight car design, Mater. Trans. 52(5) (2011) 818-824. https://doi.org/10.2320/matertrans.L-MZ201132

[3] W. Zhang, J. Xu, Advanced lightweight materials for Automobiles: A review, Mater. Des. 221(2022) 10994. https://doi.org/10.1016/j.matdes.2022.110994

[4] Mouritz, A.P., 2012. Introduction to aerospace materials. Elsevier.

[5] I. J. Polmear, M. J. Couper, Design and development of an experimental wrought aluminum alloy for use at elevated temperatures, Metall. Trans. A 19 (1988) 1027-1035. https://doi.org/10.1007/BF02628387

[6] M. Asadikiya, S. Yang, Y. Zhang, C. Lemay, D. Apelian, Y. Zhong, A review of the design of high-entropy aluminum alloys: a pathway for novel Al alloys, J. Mater. Sci. 56(21) (2021) 12093-12110. https://doi.org/10.1007/s10853-021-06042-6

[7] J.W. Yeh, S.K. Chen, S.J. Lin, J.Y. Gan, T.S. Chin, T.T. Shun, C.H. Tsau, S.Y. Chang, Nanostructured high-entropy alloys with multiple principal elements: novel alloy design concepts and outcomes, Adv. Eng. Mater. 6(5) (2004) 299-303. https://doi.org/10.1002/adem.200300567

[8] B. Cantor, I.T.H. Chang, P. Knight, A.J.B. Vincent, Microstructural development in equiatomic multicomponent alloys, Mater. Sci. Eng. A 375 (2004) 213-218. https://doi.org/10.1016/j.msea.2003.10.257

[9] Q.F. He, Z.Y. Ding, Y.F. Ye, Y. Yang, Design of high-entropy alloy: a perspective from nonideal mixing, JOM, 69 (2017) 2092-2098. https://doi.org/10.1007/s11837-017-2452-1

[10] Y. Zhang, T.T. Zuo, Z. Tang, M.C. Gao, K.A. Dahmen, P.K. Liaw, Z.P. Lu, Microstructures and properties of high-entropy alloys, Progress in materials science 61 (2014) 1-93. https://doi.org/10.1016/j.pmatsci.2013.10.001

[11] S. Praveen, H.S. Kim, High-entropy alloys: potential candidates for high-temperature applications–an overview, Advanced Engineering Materials 20(1) (2018) 1700645. https://doi.org/10.1002/adem.201700645

[12] Z. Lyu, C. Lee, S.Y. Wang, X. Fan, J.W. Yeh, P.K. Liaw, Effects of constituent elements and fabrication methods on mechanical behavior of high-entropy alloys: A review, Metall. Mater. Trans. A 50 (2019) 1-28. https://doi.org/10.1007/s11661-018-4970-z

[13] N.D. Stepanov, D.G. Shaysultanov, G.A. Salishchev, M.A. Tikhonovsky, Structure and mechanical properties of a light-weight AlNbTiV high entropy alloy, Mater. Lett. 142 (2015) 153-155.

[14] R. Feng, M. Gao, C. Lee, M. Mathes, T. Zuo, S. Chen, J.A. Hawk, Y. Zhang, P.K. Liaw, Design of light-weight high-entropy alloys, Entropy, 18(9) (2016) 333. https://doi.org/10.3390/e18090333

[15] Feng, R., M.C. Gao, C. Zhang, W. Guo, J.D. Poplawsky, F. Zhang, J.A. Hawk, J.C. Neuefeind, Y. Ren, P.K. Liaw, Phase stability and transformation in a light-weight high-entropy alloy, Acta Mater. 146 (2018) 280-293. https://doi.org/10.1016/j.actamat.2017.12.061

[16] D.B. Miracle, O.N. Senkov, A critical review of high entropy alloys and related concepts, Acta Mater. 122 (2017) 448-511. https://doi.org/10.1016/j.actamat.2016.08.081

[17] J.W. Yeh, Alloy design strategies and future trends in high-entropy alloys, JOM 65(12) (2013) 1759-1771. https://doi.org/10.1007/s11837-013-0761-6

[18] J.M. Sanchez, I. Vicario, J. Albizuri, T. Guraya, E.M. Acuña, Design, microstructure and mechanical properties of cast medium entropy aluminium alloys, Sci. Rep. 9(1) (2019) 1-12. https://doi.org/10.1038/s41598-019-43329-w

[19] Y.E.H. Jien-Wei, Recent progress in high entropy alloys, Ann. Chim. Sci. Mat. 31 (6) (2006) 633–648. https://doi.org/10.3166/acsm.31.633-648

[20] X. Yang, S.Y. Chen, J.D. Cotton, Y. Zhang, Phase stability of low-density, multiprincipal component alloys containing aluminum, magnesium, and lithium, JOM 66 (10) (2014) 2009–2020. https://doi.org/10.1007/s11837-014-1059-z

[21] M.J. Kai, Y.J. Ma, G.Y. Zhai, H. Ma, G.J. Li, J.B. Hu, Z.H. Cao, Simultaneous strength-plasticity enhancement of dual-phase light-weight medium entropy alloy, J. Alloys Compd. 923 (2022) 166406. https://doi.org/10.1016/j.jallcom.2022.166406

[22] A. Kumar, M. Gupta, An insight into evolution of light weight high entropy alloys: a review, Metals, 6(9) (2016) 199. https://doi.org/10.3390/met6090199

[23] J. Wen, Y. Liu, Y. Huang, Y. Zhao, Effects of electromagnetic stirring and subsequent homogenization treatment on the microstructure and mechanical properties of Al70Zn10Mg10Cu5Si5 multi-component alloy, J. Alloys Compd. 960 (2023) 170725. https://doi.org/10.1016/j.jallcom.2023.170725

[24] Y. Li, Y. Zhang, Light-weight and flexible high-entropy alloys, In Engineering Steels and High Entropy-Alloys, IntechOpen, 2019.

Chapter 2

Literature review: Lightweight Al-based entropy alloys – Overview and future trend

(Accepted by *Science China Materials*)

Abstract

The emergence of a new generation of alloys, namely high-entropy alloys, has revealed the significance of the entropy effect in alloy design. Inspired by this concept, lightweight Al-based entropy alloys have been proposed recently. With increasing demand for low-density structural materials, these new alloys have significant potential for diverse applications. This review provides an overview of lightweight Al-based entropy alloys, covering their developmental background, design principles, fabrication methods, microstructures, and mechanical properties, as well as alloys suitable for high-temperature applications. A comprehensive investigation of current research on Al-based entropy alloys with a density lower than 4.0 g/cm^3 was conducted from 122 different alloys. Lightweight Al-based entropy alloys could bridge the gap between conventional Al and Ti alloys in terms of mechanical properties and density. The excellent thermal stabilities of these alloys make them attractive structural materials for use at elevated temperatures. In addition, machine learning has been suggested as an effective computational tool for alloy development. Finally, future trends in the field of lightweight Al-based entropy alloys are discussed.

Keywords: Aluminum, Entropy, Lightweight alloys, Microstructure, Mechanical properties.

2.1 Introduction

With the development of the green economy, a notable surge has occurred in the demand for lightweight materials across multiple domains, including the construction, automotive, aerospace, and marine industries. Considerable attention has been devoted to lightweight structural components that possess advantages such as reduced cost, enhanced strength, and extended service life [1-3]. Aluminum (Al) is one of the lightest metals, and Al alloys are widely used as structural materials because of their exceptional strength-to-weight ratios [4]. To attain desirable properties such as high strength, good corrosion resistance, and durable wear resistance, Al alloys typically undergo diverse heat treatments, selective element addition, severe deformation, and special surface treatments. The application of Al alloys is limited by their weak mechanical performance at elevated temperatures. Several approaches have been proposed to overcome this problem, including the introduction of microalloying elements, heat-resistant dispersoids, and fine composites [5-8]. However, these methods exhibit only limited effectiveness or require intricate and costly procedures. Similarly, improvements in the other properties of Al alloys are limited by the nature of these alloys.

A groundbreaking alloy system was proposed in 2004. Termed high-entropy alloys (HEAs), the new system subverted the traditional concept [9, 10]. Unlike conventional alloys that typically comprise one primary element, HEAs contain four or more principal elements in approximately equal proportions. Entropy is a measurement of the chaos of a system. The original idea behind HEAs was to form a disordered solid solution (SS) phase by enhancing the entropy of alloys. Their unique

compositions and structures could provide HEAs with distinct properties that make them suitable for various applications. One of the exemplary HEAs is AlCrFeCoNi, which is fabricated by mixing five elements in equal atomic ratios. This alloy has a simple, single-phase body-centered cubic (BCC) structure and exhibits excellent mechanical behavior, with a remarkable yield strength (YS) of 1.2 GPa and a notable plastic strain of 32.7% at room temperature (RT) [11]. Several HEA-related concepts have been developed over the years. According to the definition of composition, HEAs do not need to be equimolar and can have a concentration of principal elements between 5 and 35 at.%. Furthermore, HEAs may contain minor elements that modify the material properties of the base HEA, with no specific requirements for either the entropy value or the formation of a single-phase SS, resulting in significant expansion of the range and number of HEAs [12]. Simultaneously, different types of HEAs have emerged, such as eutectic HEAs [13], high-entropy intermetallic compounds [14], and lightweight HEAs [15]. The phase formation of such HEAs is far more than a single-phase SS, it and can include complex intermetallic compounds (ICs) or even amorphous phases [10]. In addition, research on entropy alloys is not limited to HEAs but expands to medium-entropy and low-entropy alloys [16, 17].

The emergence of entropy alloys has provided new design strategies for conventional alloys [16, 18]. To meet the demand for lightweight alloys, considerable research efforts have been devoted to the development of entropy alloys. Among the light elements, namely lithium (Li, 0.53 g/cm^3), beryllium (Be, 1.85 g/cm^3), magnesium (Mg, 1.74 g/cm^3), calcium (Ca, 1.55 g/cm^3), Al (2.7 g/cm^3), and titanium (Ti, 4.51 g/cm^3), Al is adopted widely in the study of lightweight entropy alloys

because of its low cost, adequate stability, high boiling point, and relatively good compatibility with transition elements [12, 19-21]. Numerous Al-based entropy alloys exhibit densities comparable to those of conventional Al alloys. The current study focuses on lightweight Al-based entropy alloys, in which the Al content surpasses that of the other elements in the alloy, such as $Al_{35}Mg_{25}Zn_{30}Cu_5Si_5$ and $Al_{80}Zn_{14}Li_2Mg_2Cu_2$ [22, 23], and the alloys incorporate a significantly larger number of alloying elements than conventional Al alloys. Some classic lightweight entropy alloys in which Al is largely involved are also discussed, such as $Al_{20}Be_{20}Fe_{10}Si_{15}Ti_{35}$ and $Al_{20}Li_{20}Mg_{10}Sc_{20}Ti_{30}$ [24, 25]. The definition of lightweight varies based on different service scenarios [21, 26-28]. This review specifically considers lightweight Al-based entropy alloys with a density restriction of less than 4 g/cm³.

2.2 Concepts, design, and fabrication methods

2.2.1 Key concepts in entropy alloys

Considering the distinct chemical compositions of HEAs, Yeh et al. [29] proposed four core effects for HEAs from the aspects of thermodynamics, structures, kinetics, and properties, which summarize the unique characteristics of entropy alloys.

1. High-entropy effect

Entropy is a thermodynamic concept for measuring system disorder. Total mixing entropy is the sum of four types of entropy, namely configurational entropy, vibrational entropy, magnetic dipole entropy, and electronic randomness entropy. In an alloy system, configurational entropy (ΔS_{conf}) is the dominant contributor and represents

total mixing entropy. Combined with the Boltzmann equation, the mixing entropy (ΔS_{mix}) of n-component solutions can be estimated as follows [30]:

$$\triangle S_{mix} \approx \triangle S_{conf} = -R \sum_1^n x_i ln x_i \quad (1)$$

where R is the gas constant and x_i is the mole fraction of the i^{th} component. This calculation is conducted primarily for alloys in high-temperature states; however, it is also often used for discussing alloys at ambient temperatures because it is convenient and consistent [31]. From Eq. 1, a maximum ΔS_{mix} occurs when $x_i = 1/n$, i.e., the equimolar alloys. Therefore, HEAs comprising four or more equiatomic or near-equiatomic elements exhibit higher entropy values than conventional alloys.

The high-entropy effect is a signature concept of HEAs. The Boltzmann equation provides a straightforward method to estimate ΔS_{mix} from the alloy composition. Based on the magnitude of entropy calculated using Eq. 1, alloys can be classified as low-entropy alloys (LEAs), medium-entropy alloys (MEAs), and HEAs, where their entropy values fall within the ranges <1R, 1R–1.5R, and >1.5R [32], offering vast opportunities to discover novel alloys with exceptional properties and practical usage. High entropy favors the formation of disordered SS phases and suppresses the formation of ICs [33]. However, this is not the decisive criterion for the formation of SS, as the chemical properties of the elements also play a part [34, 35]. HEAs may comprise only intermetallic compounds (ICs) [36, 37], whereas a single SS may appear in MEAs [38, 39].

2. Severe lattice distortion effect

Because a large quantity of multiple elements is added, instead of arranging in a highly ordered repeating pattern as in the traditional structure of one dominant element SS, each atom in the SS phase of HEAs is surrounded by various atoms with different sizes and chemical properties, thereby inducing lattice strain and stress. These distortions are much more severe than those observed in conventional alloys. Severe lattice distortion effect can affect the performance of alloys, e.g., promoting mechanical strengths [40], reducing thermal effects [32]. It was found recently that lattice distortion benefits the ICs in HEAs, making them strong yet malleable [41].

3. Sluggish diffusion effect

Diffusion kinetics is proposed to be sluggish in HEAs, as atoms are trapped in low-energy sites because of the higher activation of lattice potential energy and diffusion is slowed down [42]. The sluggish diffusion effect could benefit HEAs by lowering phase transformation, promoting nanoprecipitation, and increasing creep resistance [32]. Although several studies have investigated the decreased diffusion coefficients in HEAs [42-44], this effect is not considered conclusive, as the slowed down diffusion kinetics could be associated with normal variability in diffusion data. Accordingly, carefully designed experiments are required for the validation of this aspect [45-47].

4. Cocktail effect

The cocktail effect refers to a synergistic combination in which the ultimate outcome is both unforeseeable and surpasses the combined potential of the individuals [12], thereby addressing the remarkable and unexpected properties of HEAs. The

performance of multicomponent alloys typically exceeds the expectation of linear property changes resulting from the combinations of different elements. The exceptional material properties in HEAs, such as ultra high strength with good fracture toughness, fatigue properties, and ductility are often observed to result from unpredictable synergies.

Along with the development of HEAs, several alloys with wider definitions and excellent properties have been developed [12, 48]. Single-phase SS is not the only final goal, as the eutectic microstructure and the ICs play important roles in alloy performance. For example, alloy $Fe_{0.75}Co_{0.75}Ni_{0.75}Cu_{0.75}TiZrHf$ with a fully ICs structure shows a high YS of 2.25 GPa with exceptional high-temperature phase stability [14].

Inspired by the novel concepts of HEAs and the potentially excellent performance brought about by the increased entropy, several researchers have designed low-density alloys with an entropy value higher than that of conventional alloys, such as the Mg-based entropy alloy $Mg_{62}Li_{13}Zn_{12}Cu_{10}Y_3$ [49], Al-based entropy alloy $Al_{63}Mg_{27}Zn_{4.5}Cu_{4.5}Si_1$ [50], and Ti-based entropy alloy $Ti_{65}(AlCrNb)_{35}$ [51]. Notably, the entropy values of these lightweight-element-based alloys may not reach the same level as those of the HEAs. However, these alloys have the potential to leverage the benefits of their lower density and higher entropy, which could give rise to exceptional properties. Such properties facilitate bridging the gap between conventional alloys and classic HEAs, thereby offering a promising avenue for material development.

2.2.2 Design methods

The emergence of HEAs poses new challenges for establishing the traditional relationships between their chemical compositions, microstructures, and material properties. The vast range of chemical compositions significantly increases the number of possible alloys and the complexity of their microstructures. Even in the same alloy family, changing one element or its content could significantly affect the microstructure and properties. Two primary approaches are conventionally followed in alloy design for predicting phase formation in entropy alloys. The first approach involves a series of empirical thermophysical parameters based on the Hume-Rothery rules. The other approach is the Calculation of Phase Diagrams (CALPHAD) method, which is a computational method that could accelerate alloy development by predicting phase diagrams and phase stabilities based on multicomponent thermodynamic databases.

1. Empirical thermophysical parameters

Empirical thermophysical parameters are the earliest and most practical methods following the Hume-Rothery rules [52]. Table 2.1 shows a summary of the conventionally used parameters and corresponding brief introductions. Experimental results have indicated that the calculated parameters are usually associated with phase formation. For example, the extremely negative ΔH_{mix} (<-12 kJ/mol) favors the appearance of the amorphous phase [53]; the VEC could be used to quantitatively predict the phase stability for BCC and face-centered cubic (FCC) phases in HEAs [54]. The formation of a disordered SS is anticipated when ΔS_{mix} is sufficiently high to

offset the impact of ΔH_{mix}, which is crucial to prevent segregation and the formation of ordered ICs [55]. Fig. 2.1 shows the relationship between parameters δ and Ω in determining the phase formation in HEAs [56], indicating that Ω≥1.1 and δ ≤6.6% could be a criterion for forming SS in HEAs. Similar expectations exist for other parameters, e.g., $\Delta\chi \leq 0.175$, -22 kJ/mol $\leq\Delta H_{mix} \leq$ 5 kJ/mol.

As regards lightweight entropy alloys, because of the significantly different chemical properties of low-density elements, the values of empirical parameters could differ from those of HEAs based on transition elements, e.g., $\delta < 4.5\%$, -1 kJ/mol $\leq\Delta H_{mix} \leq$ 5 kJ/mol, $\Omega > 1.1$ [50, 57]. Our previous work shows that a higher Ω value correlates to a lower tendency to form complex phases in Al-based multicomponent alloys [16]. During the alloy design process, the type and content of the constituents could be tailored and adjusted to ensure that each parameter falls within a specific range.

This method has two shortcomings. First, the parameters can be approximate and inaccurate, particularly when ICs form. Second, the specific phase formation cannot be predicted. However, the method is easy to implement and can serve as a preliminary guideline for alloy design [58, 59]. Chauhan et al. [60] designed alloy $Al_{35}Cr_{14}Mg_6Ti_{35}V_{10}$ by adjusting the thermodynamic parameters values, and the alloy was confirmed to possess a relatively simple phase formation.

Table 2.1 Summary of commonly used parameters in HEAs.

Parameters	Equation	Description
Mixing entropy	Referring to equation (1)	-

Mixing enthalpy	$\triangle H_{mix} = \sum_{i=1, i<j}^{n} 4 \triangle H_{AB}^{mix} c_i c_j$	$\triangle H_{AB}^{mix}$ is the mixing enthalpy of the binary A and B elements, c_i, c_j are the molar content of i^{th} and j^{th} element
Mixing temperature	$T_{mix} = \sum_{i=1}^{n} c_i (T_m)_i$	$(T_m)_i$ is the melting temperature of the i^{th} element
Melting temperature difference	$\triangle T_{mix} = \sqrt{\sum_{i=1}^{n} c_i [(T_m)_i - T_{mix}]^2}$	-
Ratio of entropy to enthalpy	$\Omega = \frac{\triangle S_{mix} T_{mix}}{\lvert \triangle H_{mix} \rvert}$	-
Atomic size difference	$\delta = \sqrt{\sum_{i=1}^{n} c_i (1 - \frac{r_i}{\sum_{i=1}^{n} c_i r_i})^2}$	r_i is the atomic radius of the i^{th} element
Valance electron concentration	$VEC = \sum_{i=1}^{n} c_i (VEC)_i$	$(VEC)_i$ is the VEC of the i^{th} element
Pauling electronegativity difference	$\triangle \chi = \sqrt{\sum_{i=1}^{n} c_i (\chi_i - \sum_{i=1}^{n} c_i \chi_i)^2}$	χ_i is the Pauling electronegativity for the i^{th} element
Theoretical densities	$\rho_{mix} = \frac{\sum_{i=1}^{n} c_i A_i}{\sum_{i=1}^{n} c_i A_i / \rho_i}$	A_i and ρ_i are the atomic weight and density of the i^{th} element

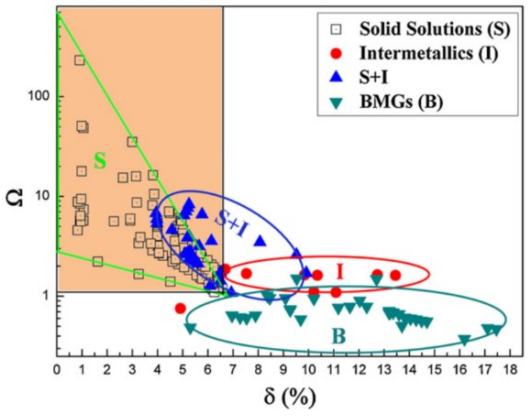

Fig. 2.1 Distribution of parameters δ and Ω in HEAs having various phase formation, wherein, S and I indicate the alloys comprise only SS and ICs, respectively; and S+I indicates the simultaneous existence of both SS and ICs; B indicates the alloys include bulk metallic glasses (BMGs) [56]. Copyright 2011, Elsevier.

2. CALPHAD method

The CALPHAD method is a robust approach for entropy alloy design that calculates phase stability by modeling the Gibbs free energy [30, 61]. Phase prediction software based on CALPHAD methodology is adopted widely in Al-based entropy alloy design, e.g., Thermo-Calc and Pandat [62-65]. This approach can be used to predict specific phases, phase compositions, volume fractions, and transformation temperatures. Prediction accuracy is highly related to the thermodynamic database. Most commercial thermodynamic databases are based on one-principal element alloys, but in multi-primary element alloy systems, these databases remain largely unexplored. Although some HEA databases have been developed, they are restricted to transition-element-based HEAs. Standard databases for Al alloys are commonly adopted for Al-based entropy alloys, and several studies have confirmed that the prediction accuracy of phase formation is acceptable [62, 66-69]. By expanding the databases to include more studies on a particular element group relevant to Al-based entropy alloys, the discrepancies between CALPHAD simulation and experimental results are expected to decrease.

Several authors have also developed alloys based on promising previous studies by modifying the content of specific elements [23, 70]. To date, the design methods for lightweight Al-based entropy alloys are relatively limited. With the assistance of computer science, some approaches with high efficiency have been developed recently, such as CALPHAD-based high-throughput calculation, which screens the target alloys

from a vast composition space [71], and machine learning, which will be discussed in detail in Section 2.5.

2.2.3 Fabrication methods

Fabrication methods employed for producing 122 lightweight Al-based entropy alloys are summarized in Fig. 2.2a. The melting and casting method is employed mostly, which includes induction melting and melting in an electric resistance furnace, etc. Casting is the next step in the fabrication process. In some instances, other routes such as mechanical alloying and deposition have been adopted. Among the various fabrication methods, induction melting has emerged as the predominant technique, constituting approximately 70% of the total fabrication process, as shown in Fig. 2.2a. This method differs from the method followed for refractory HEAs based on transition elements, i.e., arc melting, which is the main route because the high temperature (> 3000 °C) melts the constituent elements [28]. For Al-based entropy alloys, the lower melting points of the constituent elements could be accommodated using an induction melting furnace. Moreover, the electromagnetic forces generated within the induction furnace aid in stirring the molten metals, resulting in improved mixing during the fabrication process.

Melting and casting routes are conventionally accessible in most laboratories, which are cost effective and relatively user-friendly. Therefore, it is a practical and efficient method for producing Al-based entropy alloys. However, due to the high concentration of multiple elements, Al-based entropy alloys could exhibit poor liquidity and castability compared to the conventional alloys [72]. The casting in most

of the recent studies is reported to be carried out on relatively small lab-scale, while many defects, such as compositional inhomogeneity and porosity, could appear in the ingots [49, 67, 73-75]. To address this issue, it is necessary to remelt the ingots several times to achieve a homogeneous distribution of the alloying elements, thereby improving the overall quality of the cast ingots [50, 76]. The increase in ingot size may lower the solidification rate and elevate the risk of defects. Consequently, the industrial-scale manufacture of entropy alloys remains challenging [67]. Reportedly, the introduction of a eutectic microstructure could enhance the castability of alloys [16, 50]. Lu et al. [13] achieved the production of industrial-scale $AlCoCrFeNi_x$ (x= 2.0, 2.1 and 2.2) ingots by incorporating a eutectic microstructure, and all the ingots exhibited excellent castability. This presents a promising avenue for the industrial-scale manufacture of Al-based entropy alloys. Additionally, Li et al. [23] reported that a Zn content of 10 at.% can contribute to high castability of the Al-based entropy alloys, attributed to the attainment of the eutectic point. Moreover, researchers have also explored various techniques during the melting and casting process to enhance the quality of the cast metal, such as supergravity [73], ultrasonic vibration [77], and electromagnetic stirring [72]. Baek et al. [62] reported that the ultrasonic melt treatment can completely remove pores in the ingots through a degassing effect, thereby improving overall ingot quality.

Fig. 2.2b shows the use of elements in lightweight Al-based entropy alloys. A total of 26 alloying elements were used in combination with Al in 122 alloys. Mg, Zn, Cu and Si are the elements most often used. The adoption of flammable and explosive elements, such as Li and Ca, makes the melting process challenging. Moreover, the

significantly different melting points of the elements could cause the loss of low-melting-point elements. For example, Cr has a melting point of 1860 °C, which is much higher than that of Zn (419 °C) and even higher than the boiling point of Zn (907 °C). Further, vacuum melting could lead to the early evaporation of low-melting-point metals, making element loss more severe. An efficient approach to overcome this issue involves maintaining the metals at a suitable temperature below their boiling points for a prolonged period. This method enables thorough mixing of the elements through liquid diffusion [16]. However, this technique is effective when the content of high-melting-point elements is not excessive. In such situations, the excessive addition of low-melting-point elements could compensate for the losses encountered during the process. This technique helps maintain the desired alloy composition.

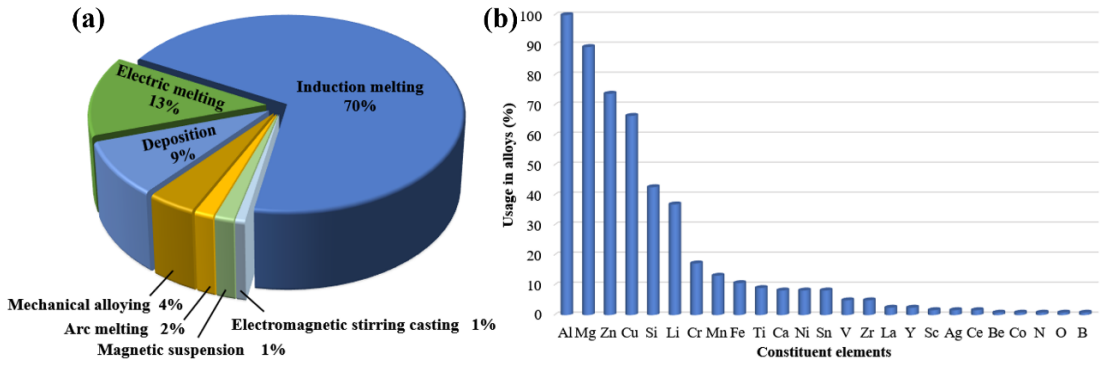

Fig. 2.2 The usage of (a) fabrication methods and (b) constituent elements in 122 Al-based entropy alloys.

Mechanical alloying is a non-equilibrium powder alloying process that could prevent evaporation during fabrication. Singh et al. [78] synthesized MgAlSiCrFe by mixing pure elements. After 60 h of high-energy ball milling, the powder contained a major body-centered cubic (BCC) phase, with a minor amount of undissolved Si. However, this structure is not thermally stable at temperatures above 400 °C, causing

the formation of various phases during annealing. Several researchers [25, 60, 78] have observed the formation of a simple phase in the milled powder, but subsequent annealing or sintering processes could generate complex phases [79]. Moreover, mechanical alloying usually requires long-term milling, which makes the process relatively expensive.

2.3 Microstructure and mechanical properties

2.3.1 Microstructural characteristics of lightweight Al-based entropy alloys

Fig. 2.3 summarizes 116 reports on the microstructure classifications of the lightweight Al-based entropy alloys. As Fig. 2.3a shows, the mixture of SS and ICs microstructures is the most reported phase formation (87 reports, comprising 75% of the total), and the subclassifications show that most (SS+ICs) alloys contain 3–6 phases. Among the alloys, 22% (25 reports) only comprise ICs and 3% (four reports) simply comprise SS. Fig. 2.3b shows that the SS phase occurs in only 3% of the alloys (three reports), 2% (two reports) have a high phase number of 8, and 71% of the alloys (82 reports) include 3–5 phases.

Of the 116 reports analyzed, the SS phase occurs 94 times, FCC phase 83 times, hexagonal close-packed (HCP) phase 6 times, and the BCC phase 5 times. Fine precipitates are observed in some as-cast alloys [62, 80, 81]. These findings provide insight into the prevalence of different phases in the studied Al-based entropy alloys. Fig. 2.4 shows the number of occurrences of the 10 most frequently occurring phases. The FCC phase is the most observed phase, which, typically, indicates the presence of fcc-Al with significant amounts of solute atoms such as Cu, Zn, and Mg [27].

Additionally, nine types of ICs occur frequently in the alloy system, including Al_2Cu, Mg_2Si, $MgZn_2$, and others. It can be seen that the lightweight Al-based entropy alloys usually comprise disordered fcc-Al and ordered ICs. Fig. 2.3a indicates the high occurrence of ICs, with a total rate of 97%. Consequently, the formation of ICs in Al-based entropy alloys is almost inevitable.

As ICs are usually hard and brittle, the ductility of alloys could be reduced. However, strong ICs could reinforce fcc-Al, thereby improving the mechanical behavior of the alloys, particularly at high temperatures [16, 81-83]. Further, ICs have been reported to ameliorate other properties such as thermal stability, anti-oxidation, and wear resistance [74, 83, 84].

The grain size of Al-based entropy alloys, which is affected by the chemical composition, fabrication route, and mechanical treatment, varies from nanoscale to microscale. Youssef et al. produced nanocrystalline $Al_{20}Li_{20}Mg_{10}Sc_{20}Ti_{30}$ with a grain size of 12 nm by mechanical alloying [25]. Alloy $Al_{78}Zn_{13}Mg_5Li_2Cu_2$ fabricated by droplet ejection exhibits a grain size of 2–5 μm [85].

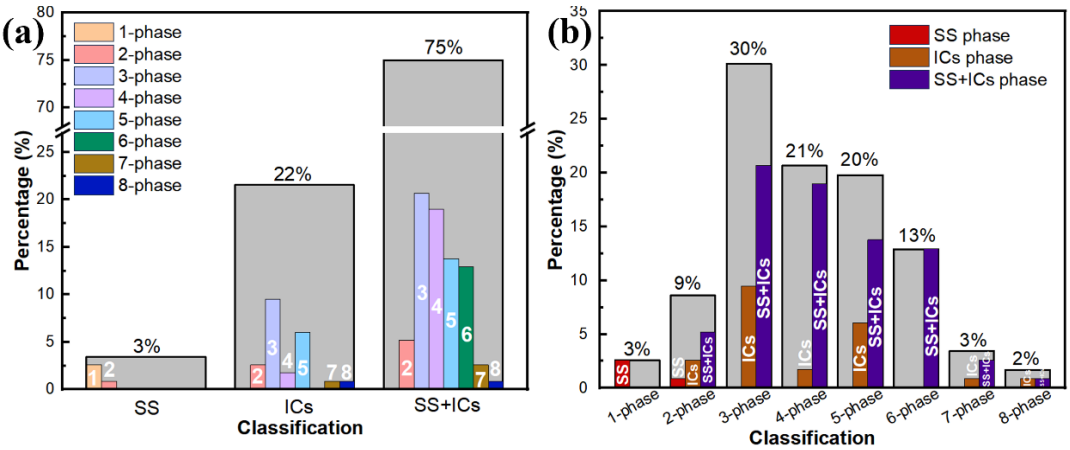

Fig. 2.3 Microstructure classification by (a) phase type and (b) number of phases (SS, ICs, and SS+ICs indicate the alloys comprise only SS, only ICs, and the combination of SS and ICs, respectively; 1-phase indicates the alloys only comprise 1 phase, 2-phase indicates the alloys only comprise 2 phases, and so on).

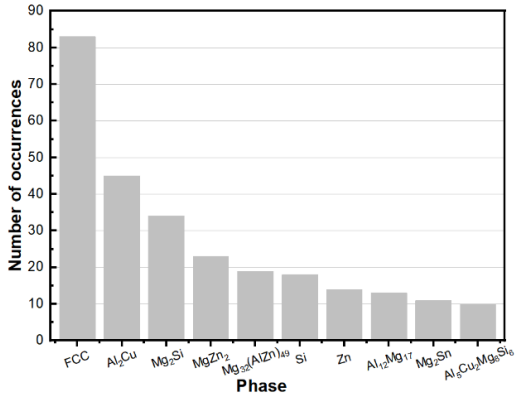

Fig. 2.4 The number of occurrences of the 10 most frequently occurring phases.

The average grain size of $Al_{80}Zn_{14}Li_2Mg_2Cu_2$ obtained through melting and casting is approximately 100 μm [23]. Ultrasonic treatment during the melting process and ultrasonic hammering treatment toward ingots have been shown to significantly decrease the grain size [62, 86]. According to Zhang et al. [87], the addition of Cu reduces the grain size. The enclosed ICs network could isolate the grains [80, 88]; however, the distribution of ICs within the alloys does not necessarily occur along the boundaries to induce grain boundary breakage [62, 70, 86], but could be affected by the chemical composition and fabrication conditions.

Compared with transition-element-based HEAs, lightweight Al-based entropy alloys always exhibit complex phase formation (Figs. 2.3–2.4) even if they meet the criteria for being classified as HEAs [48]. For example, $Al_{35}Li_{20}Mg_{20}Si_{15}Zn_{10}$, $Al_{35}Li_{20}Zn_{20}Si_{15}Mg_{10}$, and $AlLi_{0.5}MgZn_{0.5}Cu_{0.2}$ only comprise ICs [57, 89]. From a thermodynamic perspective, this phenomenon is ascribed to the effect of entropy (the

tendency to form SS) not offsetting the effect of enthalpy (the tendency to form ICs) [55]. This result could also derive from the high electronegativity difference and strong interatomic interactions among the light elements [23]. Yang et al. analyzed the phase formation rules and suggested that the multiphase feature could result from the lack of d-orbitals in the lightweight elements, which prevents higher-order hybridization [57]. Roy et al. [90] studied 329 entropy alloys and concluded that the strongest contributions to phase formation derive from the parameters, including mixing melting temperature T_{mix}, and electronegativity difference $\Delta\chi$.

The relationship between phase formation and thermodynamic parameters was analyzed for 122 entropy alloys. Fig. 2.5 shows five typical diagrams concerning ΔT_{mix}, ρ_{mix} (theoretical density), ΔS_{mix} (mixing entropy), ΔH_{mix} (mixing enthalpy), and Ω (ratio of entropy to enthalpy) for phase formation. Among the parameters, the melting temperature difference ΔT_{mix} and mixing density ρ_{mix} have a relatively close correlation with the phase number, as shown in Fig. 2.5a–b. The phase number would probably be greater with an increase of ΔT_{mix} and ρ_{mix}. The melting temperature was found analogous to the bonding energy. Elements with higher melting temperatures inhibit the incorporation of elements with low bonding energies to prevent the formation of complex phases [90]. Therefore, an increase in ΔT_{mix} leads to a high likelihood of multiple phase formation. The addition of heavy elements, which possess properties differing significantly from those of lightweight elements, could cause complex phase formation.

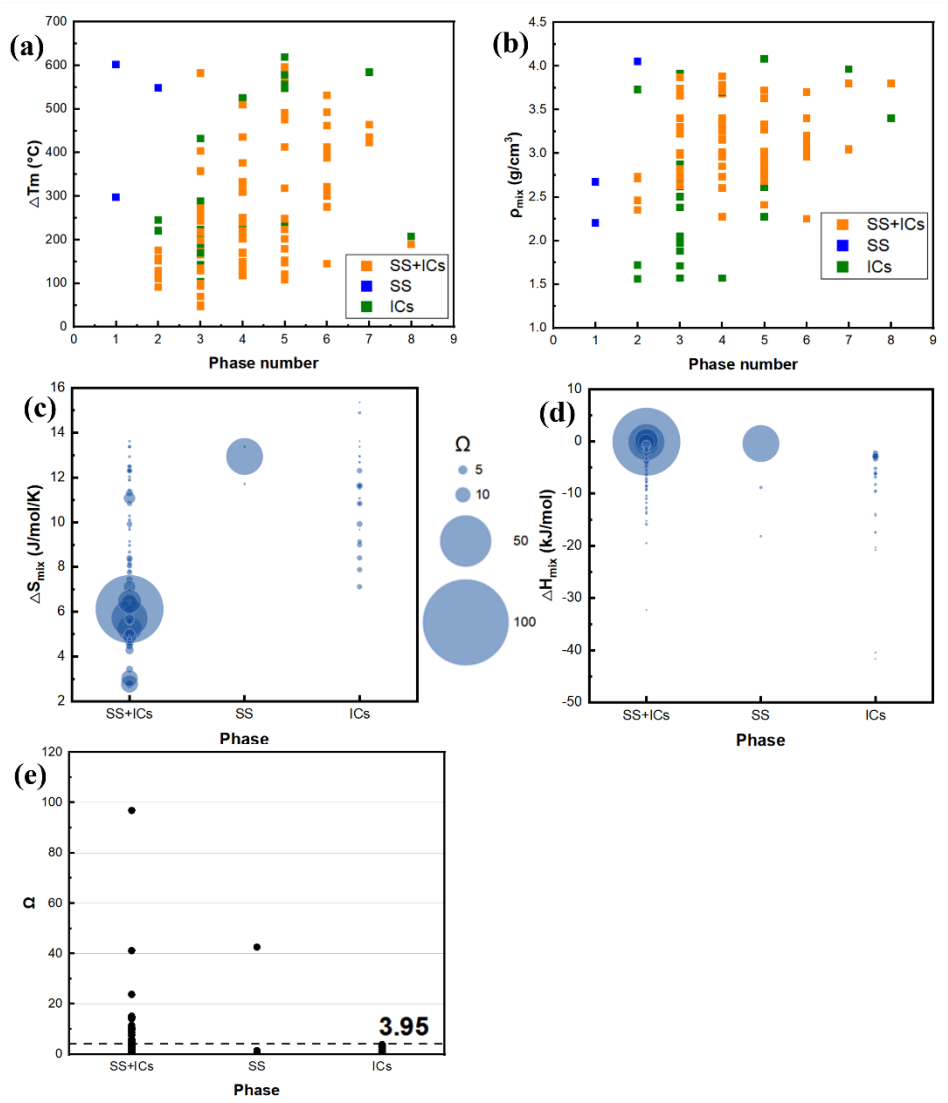

Fig. 2.5 Phase formation vs. thermodynamics parameters of Al-based entropy alloys. The size of bubble in Fig. 2.5c-d represents the magnitude of Ω.

The effect of two core thermodynamic parameters, ΔS_{mix} and ΔH_{mix}, is shown in Fig. 2.5c–d. Alloys solely comprising SS have a high mixing entropy value. However, high ΔS_{mix} is not the decisive factor for SS, as several alloys containing ICs also possess high ΔS_{mix}. For example, alloy AlMgLiCaCuZn has a high ΔS_{mix} up to 14.9 J/mol/K (1.79R), but comprises only ICs. As regards ΔH_{mix}, most SS or (SS+ICs) alloys, i.e., SS-containing alloys, commonly have a value close to zero, and tend to be higher than that of ICs alloys. Therefore, the role of ΔH_{mix} appears to be more important than that

of ΔS_{mix} in determining SS+ICs phase formation. The bubble size represents the magnitude of Ω. Although some ICs have a high ΔS_{mix}, their Ω values are low, ranging from 0.54 to 3.95, as indicated in Fig. 2.5e. This finding implies that Ω plays a crucial role in determining phase formation.

2.3.2 Mechanical properties of lightweight Al-based entropy alloys

Mechanical properties are vital for structural materials. Lightweight Al-based entropy alloys have potential suitability for high-strength applications. Because most lightweight Al-based entropy alloys are currently fabricated at small laboratory scale, which is limited by the sample size, their mechanical properties are usually measured by hardness and compression tests as an initial screening of mechanical performance. Sanchez et al. [27] fabricated an alloy $Al_{65}Cu_5Cr_5Si_{15}Mn_5Ti_5$ with a hardness of 889 HV. According to a report by Yang et al. [57], the entropy alloy $Al_{80}Li_5Mg_5Zn_5Cu_5$ exhibits a low density of 3.08 g/cm^3, high compressive fracture strength of 879 MPa, and good plasticity of 17%. Shao et al. [50] investigated Al–Mg series entropy alloys with low densities ranging from 2.64 to 2.75 g/cm^3, with the $Al_{85}Mg_{10.5}Zn_{2.025}Cu_{2.025}Si_{0.45}$ alloy showing outstanding compressive strength of 814 MPa and excellent plasticity up to 24.8%. Li et al. [23] produced a high-Zn Al-based entropy alloy, namely $Al_{80}Zn_{14}Li_2Mg_2Cu_2$, which exhibited remarkable compressive strength (>1 GPa) and high plasticity (>20%).

Fig. 2.6 shows the distribution of the strengths of alloys at RT. As shown in Fig. 2.6a–b, as the density increases, both the compressive strength and the YS tended to increase. An increase in the density resulted in a greater phase number (Fig. 2.5b),

which increased the possibility of obtaining a higher YS (Fig. 2.6c). Among the multiple phase constitutes, ICs accounted for the majority. Consequently, ICs play an important role in material strengthening. However, the green points in Fig. 2.6a indicate that the alloys comprising only ICs have low compressive strength. This was caused by the brittleness of ICs, as samples broke at an extremely low strain at the beginning of the test, and no YS (at a 0.2% offset strain) could be measured for these ICs alloys. Therefore, ICs alloys do not exhibit favorable mechanical properties at RT. Incorporating an optimal number of ICs along with SS could confer high strength and a certain degree of plasticity to alloys. The presence of SS could facilitate coordinated plastic deformation and is, therefore, preferred in entropy alloys. As discussed in Section 2.3.1, a Ω value higher than 3.95 could be set on purpose during alloy design to avoid ICs alloys.

Fig. 2.6d shows that Al-based entropy alloys generally have high strength and low strain. Some Al-based entropy alloys possess high YS of over 600 MPa even in the as-cast state, which is unachievable for conventional Al cast alloys. The relationship between YS and strain follows 'banana-like behaviour' (Fig. 2.6d), that is, the increase of YS comes at the cost of reduced ductility. High ΔS_{mix} is usually associated with high YS in Al-based entropy alloys (Fig. 2.6e), with this correlation being ascribed to two main factors. First, higher ΔS_{mix} in Al-based entropy alloys could cause a greater number of phases, which contribute to strengthening the alloys. Second, higher ΔS_{mix} could cause a more pronounced sluggish diffusion effect and induce significant lattice distortion in the alloys [27, 47], enhancing the concentration of solute atoms in each phase, thereby improving the resistance for dislocation movement.

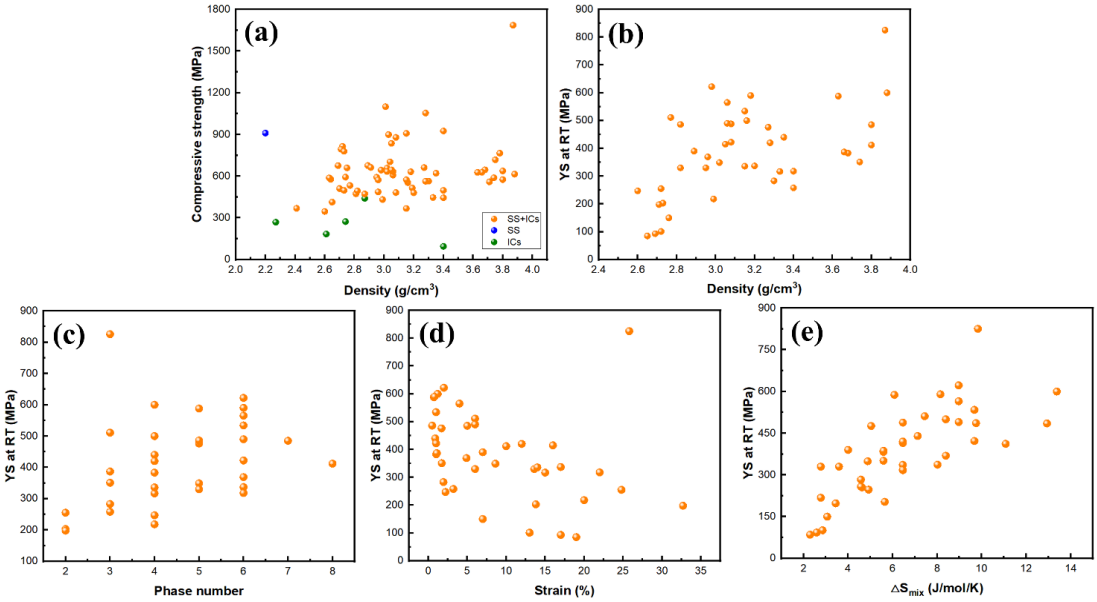

Fig. 2.6 Distribution of strengths of Al-based entropy alloys at RT.

Generally, the strengthening mechanisms of Al-based entropy alloys are considered dislocation hardening, grain-boundary strengthening, solid-solution strengthening, and precipitation strengthening [22, 23, 85]. The sluggish diffusion effect could have increased the concentration of solute atoms in the fcc-Al matrix, resulting in higher solid-solution strengthening and precipitation strengthening in the as-cast alloys [27, 62, 80, 91]. Moreover, a well-connected ICs network could be vital support for the matrix during deformation, thereby increasing its hardness and strength [16, 67, 81]. However, brittle ICs could severely decrease the ductility, resulting in extremely low strain (Fig. 2.6d). Several approaches have been proposed to balance the tradeoff between strength and ductility caused by coarse secondary phases [75, 92, 93]. Xie et al. [75] adopted severe plastic deformation to break ICs and improve the mechanical properties of Al–Li–Mg–Zn–Cu lightweight HEAs. This deformation-driven modification brought about $Al_{80}Li_5Mg_5Zn_5Cu_5$, which increased tensile strength from 200 MPa to 674 MPa and tenable ductility from 0.5% to 7.5%.

Based on the strengthening mechanisms, various approaches have been suggested to further improve the mechanical properties. For instance, an appropriate electromagnetic frequency during electromagnetic stir casting could effectively refine uniform grains and secondary phases, and increase the solid solubility of alloys, thereby increasing their strength [94]. Similarly, ultrasonic melt treatment helps reduce the porosity and size of the grains, resulting in improved strength and increased fracture strain [62]. Li et al. [86] applied ultrasonic hammering treatment to $Al_{80}Li_5Mg_5Zn_5Cu_5$ entropy alloy, which significantly reduced the grain size from 200 μm to 5 μm, and induced dislocation strengthening, resulting in improved hardness and elastic modulus. Cooling rates after solution treatment reportedly also affect mechanical behavior by inducing precipitation strengthening or solid-solution strengthening [95].

Fig. 2.7a shows the Ashby diagram of strength vs. density for the various materials at RT [96]. The location of Al-based entropy alloys marked by red points indicates their low-density and high-strength characteristics in the metal field. The locally enlarged diagram, focusing on conventional Al, Ti alloys, and Al-based entropy alloys, is presented in Fig. 2.7b. Wherein, combined with new progress reported in recent years [97-99], the upper limits of YS for conventional Al and Ti alloys have been modified to 590 MPa and 1443 MPa, respectively, relative to those depicted in Fig. 2.7a. From Fig. 2.7b, the Al-based entropy alloys could possess high YS which conventional Al alloys cannot achieve, and they bridge the gap between conventional Al and Ti alloys.

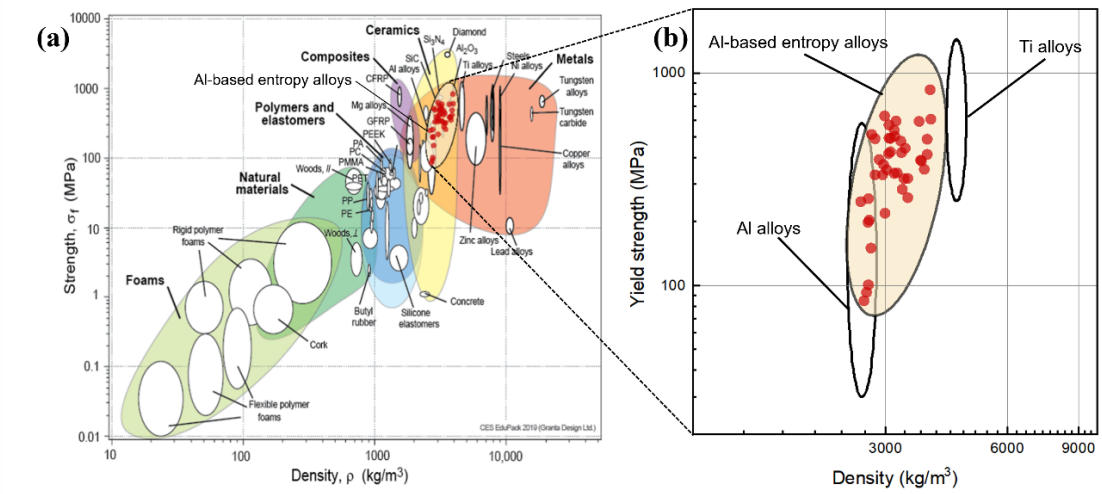

Fig. 2.7 (a) Ashby diagram of strength vs. density for various materials at RT [96], Copyright 2011, Elsevier, and (b) locally enlarged diagram with modification to the upper limits of YS for conventional Al and Ti alloys.

2.4 Al-based entropy alloys for elevated-temperature applications

2.4.1 Commonly studied alloy systems

With the major transformation toward a green economy, the demand for lightweight Al alloys with outstanding microstructural stability and resistance to softening at elevated temperatures is increasing significantly. Several conventional heat-treatable Al alloys, such as Al–Cu 2xxx and Al–Zn–Mg 7xxx alloys can achieve high strength at ambient temperatures. For example, the tensile strength of a typical high-strength AA7050-T6 alloy can exceed 570 MPa at ambient temperature [100]. However, the yield strength of AA7075 alloy at 200 ℃ and 300 ℃ is merely 30% and 10%, respectively, in comparison with its ambient temperature strength. The main limitation for elevated-temperature applications of Al alloys is the degradation of their mechanical properties and the instability of their microstructure along with the rise in temperature (general overaging effect). The Al-based entropy alloys could potentially

offer new perspectives and advantages in the field of elevated-temperature applications because of their distinctive properties, such as strength retention at elevated temperatures, excellent thermal stability, and good oxidation resistance [12]. The currently studied systems of Al-based entropy alloys are mostly Al–Mg, Al–Cu, Al–Zn, and Al–Li. Among these studies, few have investigated elevated-temperature properties. Until now, the development of elevated-temperature applications of Al-based entropy alloys has been limited to a few systems, namely the Al–Cu, Al–Mg–Si, and Al–Mg–Zn systems.

The Al–Cu system is the most extensively studied among the three categories. Our previous studies explored 11 Al–Cu-based entropy alloys [16, 81]. These alloys significantly increase the chemical composition space of conventional Al–Cu alloys by adding large quantities of Cu, Zn, Cr, Fe, Ti, and V. High Cu content is added to improve mechanical performance at elevated temperatures. High melting point elements, such as Cr, Fe, and Ti, are added to a system to facilitate the formation of heat-resistant phases at high temperatures. The high-Cu content alloys, e.g., $Al_{78}Cu_{18}Zn_2Cr_1Fe_1$, $Al_{78}Cu_{18}Zn_1Cr_2Ti_1$, and $Al_{78}Cu_{18}Zn_1Cr_2V_1$ showed high serving temperatures up to 450 °C. Other researchers [101, 102] have also designed multicomponent alloys Al-27%Cu-5%Si (wt.%), which have fine ternary eutectic microstructure and show high tensile strength under 400 °C. Further, Al–Mg–Si (e.g., $Al_{70}Mg_{10}Si_{10}Cu_5Zn_5$) and Al–Mg–Zn (e.g., $Al_{35}Mg_{35}Zn_{15}Cu_{10}Mn_5$ were investigated and exhibited desirable properties at elevated temperatures [62, 83].

2.4.2 Microstructural characteristics at elevated temperatures

The phase components of alloys operating at elevated temperatures are expected to be heat-resistant. Al_2Cu is a common IC in the Al–Cu system, and the continuous Al_2Cu network in the microstructure could provide alloys with excellent load support at elevated temperatures, making the Al–Cu alloys promising candidates for elevated-temperature applications [81]. Heat-resistant phases could be selected using the CALPHAD method, e.g., phase prediction with a change in temperature. In a previous study, we used this method to ensure microstructural stability after long-term thermal exposure, as shown in Fig. 2.8 [16]. After exposure at 300 °C for 100 h, the main phases remained the same as those of the as-cast alloys, and were expected to remain stable up to 500 °C. As discussed above, multiple ICs could increase the brittleness of alloys at ambient temperature; however, this is not an issue at elevated temperatures any longer because of their good ductility at high temperatures. Multiple ICs could yield alloys with enhanced strengths at elevated temperatures.

As regards the Al–Mg–Zn system, the simultaneous addition of Mg and Zn leads to the formation of secondary Mg–Zn phases, such as $MgZn_2$, Mg_2Zn_{11}, and $Mg_{32}(Al, Zn)_{49}$. However, these components are typically unstable at high temperatures [62, 66, 95, 103, 104]. The visual characteristics and chemical composition transformation of the Mg–Zn phase have been confirmed at a temperature of 300 °C [104]. The instability of these phases could cause uncertainty about the properties of the alloy at higher temperatures; therefore, the simultaneous addition of Mg and Zn should be approached with caution.

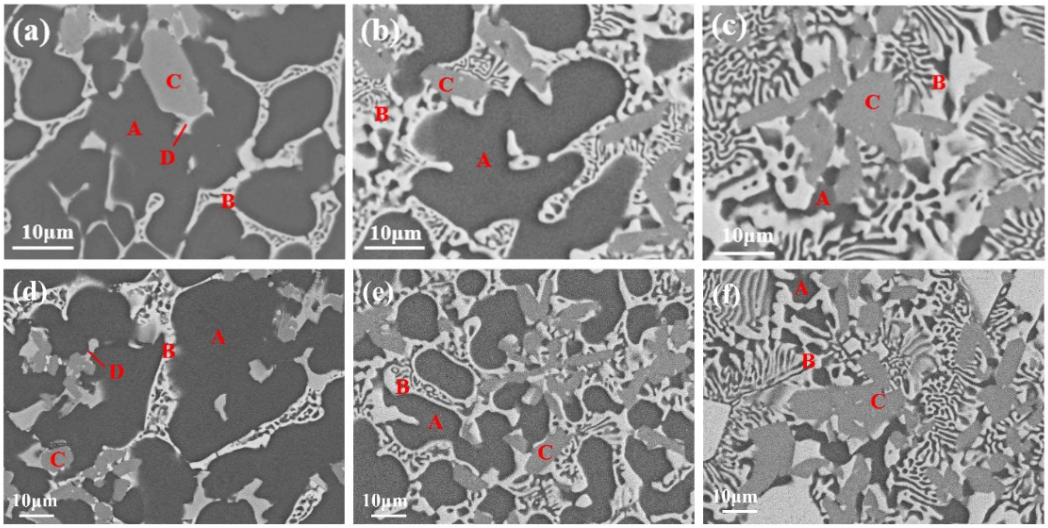

Fig. 2.8 SEM images of (a-c) as-cast and (d-f) 300 °C/100 h thermally exposed alloys: (a, d) $Al_{93}Cu_4Zn_1Cr_1Fe_1$, (b, e) $Al_{85}Cu_{11}Zn_1Cr_2V_1$, (c, f) $Al_{78}Cu_{18}Zn_1Cr_2V_1$. Wherein, the red marks A-D stand for different phase component: A is fcc-Al, B is Al_2Cu, C is $Al_{45}Cr_7$, and D is Al_7Cu_2Fe [16]. Copyright 2022, Elsevier.

2.4.3 Mechanical properties at elevated temperatures and thermal stability

Fig. 2.9 summarizes the YS vs. density of Al-based entropy alloys and conventional Al alloys at ambient temperature and 300 °C before and after thermal exposure [81]. As regards ambient-temperature strength (Fig. 2.9a) in comparison with conventional Al alloys, the Al-based entropy alloys exhibit a wider distribution of data points. The solid marks in the yellow area in Fig. 2.9a significantly outnumber those at 300 °C (Fig. 2.9b–c), indicating that mechanical behavior study on Al-based entropy alloys is currently mainly focused on ambient temperature.

Conventional Al alloys usually suffer from strength reduction at elevated temperatures owing to the coarsening of the precipitates [105]. Sadeghi et al. [83] examined the entropy alloy $Al_{35}Mg_{35}Zn_{15}Cu_{10}Mn_5$ and observed a minor decrease (only 5%) in the compression strength when subjected to a temperature change from

ambient temperature to 350 °C. Thermal stability is of utmost significance for alloys utilized in elevated-temperature applications. As shown in Fig. 2.9b–c, after thermal exposure at 300 °C for 100 h, the YS of conventional Al alloys in the blue area decreased by approximately 50 MPa, whereas the YS of some Al-based entropy alloys barely changed after thermal exposure, indicating their excellent thermal stability. This exceptional thermal stability feature extends to temperatures exceeding 300 °C. In comparison with conventional Al alloys, alloy $Al_{78}Cu_{18}Zn_1Cr_2Ti_1$ was found to possess significantly superior thermal stability and high YS of 78 MPa at 450 °C after being thermally exposed for 100 h [16].

Typically, Al-based entropy alloys contain a significant proportion of robust phases that exhibit thermal stability at high temperatures. These phases play a crucial role in supporting the alloy structure during plastic deformation by impeding the movement of dislocations and migration of grain boundaries. As discussed in Section 2.3.1, ICs appear in most lightweight Al-based entropy alloys, which leads to low plasticity as a compromise for high strength at ambient temperature. However, this problem could be alleviated significantly at high temperatures because of higher thermal activation and easier dislocation movement at elevated-temperature. As the presence of multiple phases in alloys is nearly unavoidable, they could be leveraged to enhance their mechanical properties by incorporating heat-resistant ICs. Currently, most studies on Al-based alloys are conducted at ambient temperatures, leaving elevated-temperature properties largely unexplored.

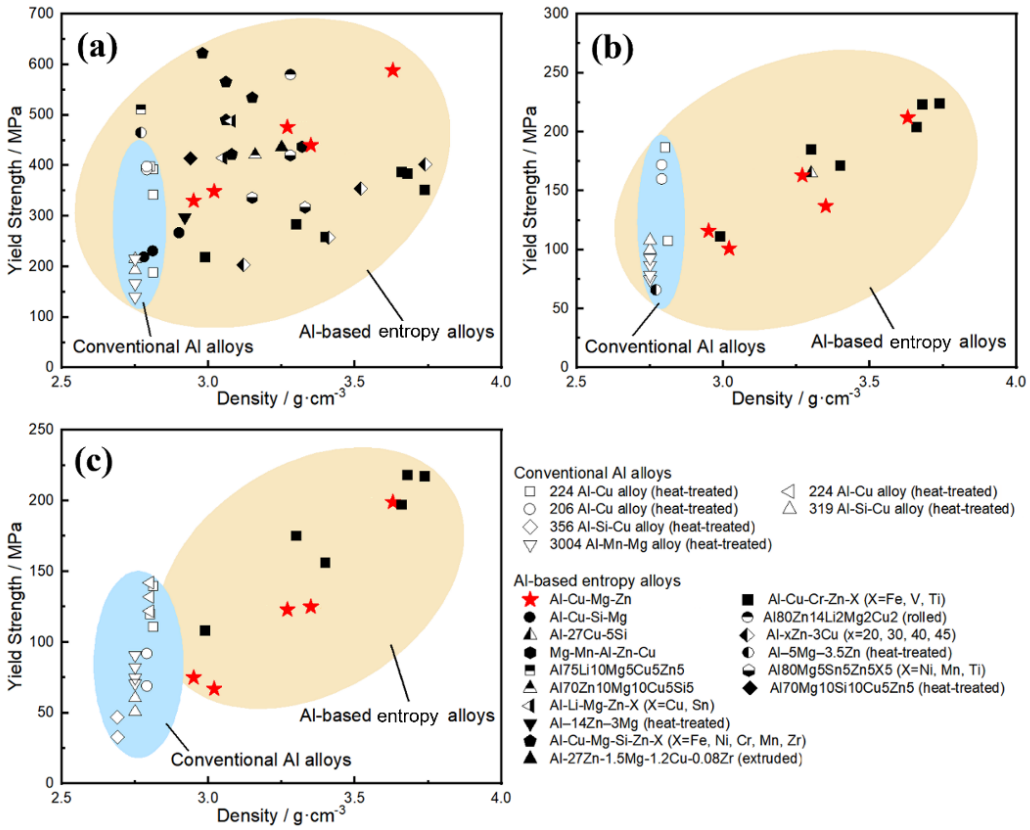

Fig. 2.9 YS vs. density of Al-based entropy alloys and conventional Al alloys at (a) ambient temperature, (b) 300 °C, and (c) 300 °C after thermal exposure [81]. Copyright 2023, Elsevier.

2.5 Potential of machine learning in lightweight Al-based entropy alloys

The concept of entropy has opened a vast design space for Al alloys. With the inclusion of multiple elements and large compositional dimensions, the combinations of elements and, therefore, the number of potential entropy alloys has become astronomical [31]. Previously, metallurgists and materials engineers have used the single-element substitution method to explore different composition and property relationships within a specific alloy family. However, for entropy alloys, the traditional 'trial-and-error' experimental approach is too expensive and time consuming [106, 107]. With the advancement of computer technology, computational simulation and

modeling methods such as the CALPHAD method (Section 2.2.2) have become increasingly crucial for alloy design. Lately, machine learning (ML), a data-driven method, is being adopted increasingly in alloy design and development for screening and predicting of alloys [108-111]. The ML method is a subset of artificial intelligence that involves the development of algorithms and statistical models, allowing computers to learn from and make predictions or decisions based on existing data. This innovative approach has emerged as a powerful tool that significantly improves efficiency within the field. ML is a promising approach for Al-based entropy alloys and could aid in the discovery of high-performance alloys.

Fig. 2.10 shows the ML workflow for property-oriented alloy design [112]. The initial step is to determine the research goals, i.e., the targeted properties as the output, such as strengths, elastic properties, fatigue properties, corrosion resistance, and electrical resistance. The relevant input data, e.g., chemical composition, structure, elemental intrinsic parameters, and experimental conditions or external properties, should be collected subsequently. The data are divided into two sets, one is the training set to train ML models as ‘active learning’, and the other is the testing set to evaluate the model. Appropriate features must be selected to train the ML model effectively. The goal is to retain useful features while eliminating redundant or irrelevant ones, which ensures that the model has the most informative features, resulting in improved performance and efficiency.

The model selection procedure is the most important step and is related directly to the accuracy of the predicted results. Numerous algorithms have been developed, including artificial neural networks, random forests, linear regression, and k-nearest

neighbors. These algorithms are classified into four main categories: classification probability estimation, primarily utilized for new material discovery; regression, clustering, and classification, commonly employed in predicting material properties and extensively adopted in the development of entropy alloys. Fig. 2.11 shows a summary of ML algorithms frequently employed in the field of material science [113]. As there is no universally optimal ML model for all problems, multiple algorithms are often adopted simultaneously, and the most appropriate or combined algorithms could be selected based on the subsequent evaluation results [114]. The data in the training set are used by the computer to learn the correlation between the features and properties, and the data in the testing set are used to evaluate the model by comparing the predicted and experimental properties.

An optimal model is constructed eventually that does not over- or underfit. This model can be applied to assist in alloy design and development, expediting or simplifying material characterization. For instance, by inputting the composition of the candidate alloys into a well-trained ML model, the predicted properties are output. Furthermore, ML could be combined with other techniques. When integrated with a high-throughput method, compositions can be input automatically into the ML model in batches, resulting in batched predictions of properties. Subsequently, these batches are screened for values that meet the desired criteria, further significantly enhancing the design efficiency.

There are several applications of ML in the field of lightweight alloys [112, 115-119]. Jiang et al. [117] adopted ML with a property-oriented strategy to develop conventional Al–Zn alloys with ultra ultimate tensile strength of 700–750 MPa and

elongation of 8%–10%. Pei et al. [120] used ML to mine 6.4 million entropy papers and finally screened nearly 500 promising HEAs out of 2.6 million candidates. By incorporating ML techniques, Wu et al. [114] found that among various thermophysical parameters, lower VEC, higher Tm, and near-zero ΔH_{mix} exerted the strongest contributions to the strength–ductility trade-off, with 70 multi-principal element alloys with YS more than 1 GPa and ductility greater than 20% provided.

Employing ML in Al-based entropy alloys remains to be explored. Vast amounts of data are the key factors for ML to be an accurate and efficient prediction tool for training models. Islam et al. [121] selected 118 data to analyze the correlation between five thermophysical parameters that lead to phase selection, with an average predictive accuracy of ~80% obtained. Zhang et al. [122] used 550 samples to predict the phase formation of HEA, with an accuracy of ~90%. Yan et al. [123] investigated single-phase refractory HEAs based on 1807 entries with the assistance of ML algorithms, and a high accuracy of 96.41% was achieved. With the rapid progress in lightweight Al-based entropy alloys, ML has the potential to improve alloy design and accelerate the discovery and development of new alloys in the near future.

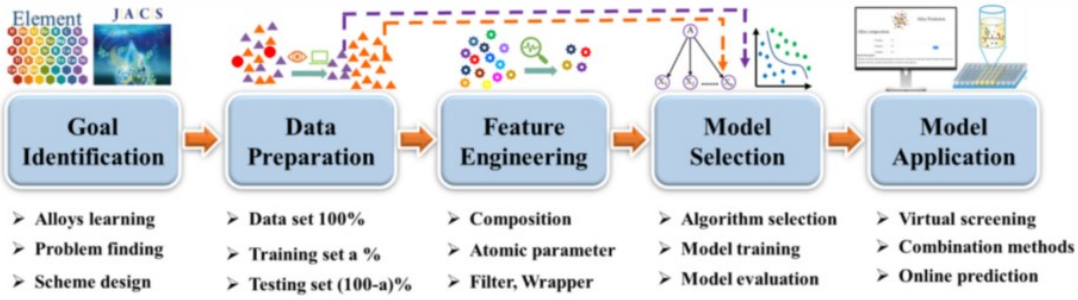

Fig. 2.10 Machine learning workflow in the field of alloy design [112]. Copyright 2022, Elsevier.

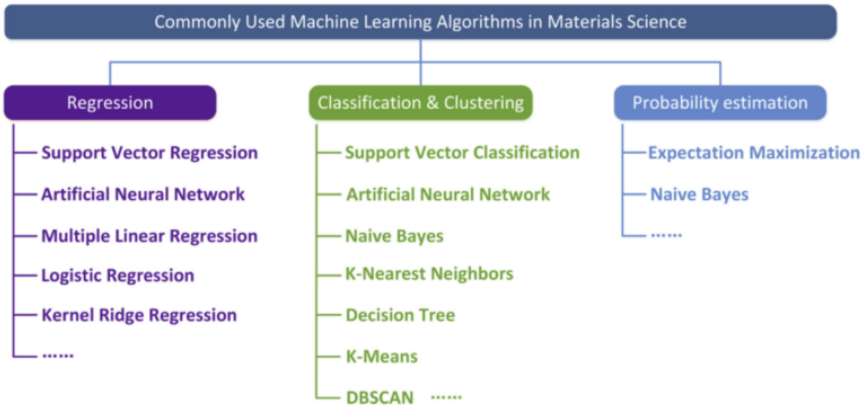

Fig. 2.11 Commonly used machine learning algorithms in materials science [113]. Copyright 2017, Elsevier.

2.6 Future trends and prospects

2.6.1 High-strength-orientated alloy design strategy

Lightweight Al-based entropy alloys fill the blank between Al alloys and Ti alloys (Fig. 2.7). These alloys possess a distinct combination of low density and high strength, making them highly promising structural materials. To fully exploit their mechanical advantages, various alloy design strategies could be implemented during alloy development.

1. Introducing suitable secondary phases

The secondary phases in these alloys could be classified into two categories, namely precipitates with nanoscale size, and relatively coarse ICs. Precipitates are known to increase the contribution from precipitation strengthening. In traditional Al alloys, precipitates emerge after heat treatment. However, in Al-based entropy alloys, they can appear directly in the as-cast state because of a sluggish diffusion effect [23, 80, 81]. These precipitates in fcc-Al promote alloy strength at ambient temperatures.

Because of the poor heat resistance of most precipitates, ICs could be considered candidates for improving mechanical behavior at elevated temperatures.

The ICs could be considered reinforcement networks in alloys that transfer external loads from soft fcc-Al to stiff secondary phases [62, 82, 124]. When the ICs are thermally stable, the stability of the mechanical performance at elevated temperatures is assured. Previous research has shown that the simultaneous addition of Mg and Zn could lead to phase instability, whereas high-melting-point elements (e.g., Cr, V, Ti) could introduce ICs that exhibit exceptional thermal stability [16, 81]. A unique nanosized Al_3Y/Al_3Ni ICs network has been reported for $Al_{87}La_{1.5}Ni_7Co_1Y_{3.5}$ [76]. This rigid frame distributes around fcc-Al grains and strengthens the alloy, and the alloy exhibits an excellent combination of high strength of 1.1 GPa and large plasticity of 11% at RT. However, its performance at high temperatures is yet to be investigated.

The eutectic microstructures of Al–Mg, Al–Cu, Al–Si, and Al–Ni, etc., are also a potential trend that could help alloys achieve a balance between strength and ductility. Meanwhile, the eutectic microstructure could improve the castability of entropy alloys [50, 125].

2. Al-based entropy composites

Al-based metal-matrix composites are of great interest because of their high specific strength; however, the main problems are poor compatibility and weak interfacial bonding between the Al matrix and reinforcement agents (i.e., ceramic and carbon fibers) [126, 127]. The particles of the high-strength entropy alloy could be

added as reinforcement to Al alloys. Lu et al. [128] separately introduced the entropy alloy $CoNiFeAl_{0.4}Ti_{0.6}Cr_{0.5}$ and typical reinforcement SiC into the 7075 Al alloy to fabricate two composites. The former was found to exhibit higher strength and toughness as well as superior interface bonding between the matrix and reinforcement. It has been reported that in an Al-based metal matrix composite reinforced with B2 type entropy alloy AlSiCrMnFeNiCu, a transitional layer with a thickness of 400–500 nm formed at the interfaces, which resulted in an enhanced microhardness of 1.81 GPa [129]. To date, studies on entropy alloy reinforcement have focused primarily on HEAs. Lightweight Al-based entropy alloy could also be a promising option. Because of the good chemical compatibility between Al-based entropy alloys and Al alloys, the reinforcement particles of entropy alloys could further improve the effectiveness and stability of interface bonding.

3. Studies on other properties

Currently, the primary focus of research on lightweight Al-based entropy alloys is examining their microstructures and mechanical properties. To fully explore the application potential of these alloys, other properties such as thermal stability, anti-oxidation, anti-corrosion, wear, corrosion resistance, and functional properties should also be studied [24, 74, 130, 131]. The rules for entropy alloys could differ from those for conventional alloys. For example, reportedly, a high Si-Mg ratio promotes the intergranular corrosion in 6xxx Al alloys [132]. However, in entropy alloy $Al_{35}Mg_{30-x}Zn_{30}Cu_5Si_x$, corrosion resistance was found to improve with the increase of the Si-Mg ratio [22].

2.6.2 Computer-assisted techniques for alloy development

With the extensive use of computer technology, computer-assisted techniques present promising prospects for advancing alloy development. In addition to the CALPHAD method (Section 2.2.2) and ML (Section 2.5), various computational techniques, including molecular dynamics simulations, density functional theory calculations, high-throughput (HT) calculations, finite element modeling, and data mining, could be valuable tools for alloy design, phase, and property prediction [120, 133-135]. These methods could expedite the development of lightweight Al-based entropy alloys.

Considering the enormous number of potential Al-based entropy alloys, the HT technique, which could automatically evaluate hundreds of thousands of candidates in a short period, is an effective approach for alloy development [71]. The HT usually functions in collaboration with other computational techniques [18, 112, 136, 137], such as ML-HT mentioned in Section 2.5. The CALPHAD-based HT computational method combines thermodynamic simulations, HT calculations, and screening, providing an efficient approach to selecting alloys with targeted thermodynamic parameters in an expansive composition space [31, 138, 139].

2.6.3 Lightweight Al-based entropy alloys for elevated temperature applications

Most current studies in this field focus primarily on the mechanical properties at ambient temperature. Indeed, some lightweight Al-based entropy alloys exhibit high or ultra high strength at ambient temperature. High strength usually results in limited ductility owing to the large IC content. Considering the inevitable occurrence of ICs

phases in most Al-based entropy alloys, it is worthy to exploit their presence. By deliberately introducing heat-resistant ICs, it is possible to significantly enhance the mechanical performance of materials (e.g., strength, creep, and fatigue resistance) not only at ambient but also at high temperatures. Two previous studies conducted by our research group have confirmed the significant potential of Al-based entropy alloys as lightweight structural materials for high-temperature applications (up to 450–500 °C) [16, 81].

2.7 Conclusion and remarks

Lightweight Al-based entropy alloys comprise multiple elements, with Al being the predominant constituent, and have a density below 4.0 g/cm^3. The inclusion of multiple elements in these alloys has led to notable effects, such as sluggish diffusion and lattice distortion, which could endow these alloys with exceptional potential for unique properties. Design methodologies typically involve empirical thermophysical parameters and calculation of phase diagrams using computational approaches. Induction melting is a widely adopted technique for fabricating Al-based entropy alloys. Nevertheless, challenges related to castability, element loss, and nonuniformity during melting persist because of the disparate melting points of the multiple constituent elements.

Phase formation in lightweight Al-based entropy alloys exhibits multiphase features. Robust ICs in these alloys could be exploited to enhance their mechanical properties. A total of 97% Al-based entropy alloys contains ICs, whereas the presence of fcc-Al is crucial for imparting sufficient ductility to alloys. Al-based entropy alloys

solely comprising ICs tend to be excessively brittle, hindering their practical use. However, with the Ω value higher than 3.95, this factor (alloys comprising only ICs) can be avoided.

Al-based entropy alloys offer a unique combination of low density and high strength, bridging the gap between conventional Al and Ti alloys at ambient temperatures. Because ICs are almost inevitable in alloys, strong ICs with good thermal stability could be introduced to reinforce fcc-Al, providing alloys with high strength at ambient as well as high temperatures. Some alloys have been proven to exhibit good heat resistance, making them promising candidates for high-temperature applications.

Conventional trial-and-error methods for alloy development are expensive and time consuming. However, the data-driven ML approach has emerged as a promising solution for predicting properties and screening suitable alloy candidates. As more experimental data becomes available, ML holds significant potential for advancing the development of Al-based entropy alloys.

References

[1] Raabe D, Tasan CC, Olivetti EA. Strategies for improving the sustainability of structural metals. Nature, 2019, 575: 64-74.

[2] Hirsch J. Aluminium in innovative light-weight car design. Mater. Trans., 2011, 52: 818-824.

[3] Zhang W, Xu J. Advanced lightweight materials for Automobiles: A review. Mater. Des., 2022, 221: 110994.

[4] Mouritz AP. Introduction to aerospace materials. Sawston, Cambridge, 2012.

[5] Hu P, Liu K, Pan L, Chen XG. Effect of Mg microalloying on elevated-temperature creep resistance of Al–Cu 224 cast alloys. Mater. Sci. Eng. A, 2022, 851: 143649.

[6] Poplawsky JD, Milligan BK, Allard LF, et al. The synergistic role of Mn and Zr/Ti in producing θ′/L12 co-precipitates in Al-Cu alloys. Acta Mater., 2020, 194: 577-586.

[7] Ma L, Zhang X, Duan Y, et al. Achieving exceptional high-temperature resistant Al matrix composites via two-dimensional BN pinning grain rotation. Compos. B: Eng., 2023, 253: 110570.

[8] Hu P, Liu K, Pan L, Chen XG. Effect of Mg on elevated-temperature low cycle fatigue and thermo-mechanical fatigue behaviors of Al-Cu cast alloys. Mater. Sci. Eng. A, 2023, 885: 145588.

[9] Yeh JW, Chen SK, Lin SJ, et al. Nanostructured high-entropy alloys with multiple principal elements: novel alloy design concepts and outcomes. Adv. Eng. Mater., 2004, 6: 299-303.

[10] Cantor B, Chang ITH, Knight P, Vincent AJB. Microstructural development in equiatomic multicomponent alloys. Mater. Sci. Eng. A, 2004, 375: 213-218.

[11] Wang YP, Li BS, Ren MX, Yang C, Fu HZ. Microstructure and compressive properties of AlCrFeCoNi high entropy alloy. Mater. Sci. Eng. A, 2008, 491: 154-158.

[12] Miracle DB, Senkov ON. A critical review of high entropy alloys and related concepts. Acta Mater., 2017, 122: 448-511.

[13] Lu Y, Gao X, Jiang L, et al. Directly cast bulk eutectic and near-eutectic high entropy alloys with balanced strength and ductility in a wide temperature range. Acta Mater., 2017, 124: 143-150.

[14] Yao K, Liu L, Ren J, et al. High-entropy intermetallic compound with ultra-high strength and thermal stability. Scr. Mater., 2021, 194: 113674.

[15] Feng R, Gao MC, Zhang C, et al. Phase stability and transformation in a light-weight high-entropy alloy. Acta Mater., 2018, 146: 280-293.

[16] Cui L, Zhang Z, Chen XG. Development of lightweight Al-based entropy alloys for elevated temperature applications. J. Alloys Compd., 2023, 938: 168619.

[17] Huang EW, Yu D, Yeh JW, et a. A study of lattice elasticity from low entropy metals to medium and high entropy alloys. Scr. Mater., 2015, 101: 32-35.

[18] Asadikiya M, Yang S, Zhang Y, et al. A review of the design of high-entropy aluminum alloys: a pathway for novel Al alloys. J. Mater. Sci., 2021, 56: 12093-12110.

[19] Cai Z, Guo Y, Liu J, et al. Progress in light-weight high entropy alloys. J. Wuhan Univ. Technol.-Mat. Sci. Edit., 2021, 36: 737-753.

[20] Sun W, Huang X, Luo AA. Phase formations in low density high entropy alloys. Calphad, 2017, 56: 19-28.

[21] Li Y, Zhang Y. Light-weight and flexible high-entropy alloys. In Engineering Steels and High Entropy-Alloys, IntechOpen, 2019.

[22] Ji C, Ma A, Jiang J. Mechanical properties and corrosion behavior of novel Al-Mg-Zn-Cu-Si lightweight high entropy alloys. J. Alloys Compd., 2022, 900: 163508.

[23] Li R, Ren Z, Wu Y, et al. Mechanical behaviors and precipitation transformation of the lightweight high-Zn-content Al–Zn–Li–Mg–Cu alloy. Mater. Sci. Eng. A, 2021, 802: 140637.

[24] Tseng K, Yang Y, Juan C, et al. A light-weight high-entropy alloy Al20Be20Fe10Si15Ti35. Sci. China Technol. Sci., 2018, 61: 184-188.

[25] Youssef KM, Zaddach AJ, Niu C, Irving DL, Koch CC. A novel low-density, high-hardness, high-entropy alloy with close-packed single-phase nanocrystalline structures. Mater. Res. Lett., 2015, 3: 95-99.

[26] Wang Z, Chen S, Yang S, et al. Light-weight refractory high-entropy alloys: a comprehensive review. J. Mater. Sci. Technol., 2023, 151: 41-65.

[27] Sanchez JM, Vicario I, Albizuri J, Guraya T, Garcia JC. Phase prediction, microstructure and high hardness of novel light-weight high entropy alloys. J. Mater. Res. Technol., 2019, 8: 795-803.

[28] Kumar A, Gupta M. An insight into evolution of light weight high entropy alloys: a review. Metals, 2016, 6: 199.

[29] Jien-Wei YEH. Recent progress in high entropy alloys. Ann. Chim. Sci. Mat., 2006, 31: 633-648.

[30] Zhang C, Gao MC, Yeh JW, Liaw PK, Zhang Y. High-Entropy alloys: fundamentals and applications. Springer, 2016.

[31] Miracle DB, Miller JD, Senkov ON, et al. Exploration and development of high entropy alloys for structural applications. Entropy, 2014, 16: 494-525.

[32] Yeh JW. Alloy design strategies and future trends in high-entropy alloys. JOM, 2013, 65: 1759-1771.

[33] George EP, Curtin WA, Tasan CC. High entropy alloys: A focused review of mechanical properties and deformation mechanisms. Acta Mater., 2020, 188: 435-474.

[34] Gorsse S, Tancret F. Current and emerging practices of CALPHAD toward the development of high entropy alloys and complex concentrated alloys. J. Mater. Res., 2018, 33: 2899-2923.

[35] Maulik O, Kumar D, Kumar S, Dewangan SK, Kumar V. Structure and properties of lightweight high entropy alloys: A brief review. Mater. Res. Express., 2018, 5: 052001.

[36] Kao YF, Chen SK, Sheu JH, et al. Hydrogen storage properties of multi-principal-component CoFeMnTixVyZrz alloys. Int. J. Hydrog. Energy, 2010, 35: 9046-9059.

[37] Gorban VF, Krapivka NA, Firstov SA. High-entropy alloys: Interrelations between electron concentration, phase composition, lattice parameter, and properties. Phys. Met. Metallogr., 2017, 118: 970-981.

[38] Li D, Dong Y, Zhang Z, et al. An as-cast Ti-V-Cr-Al light-weight medium entropy alloy with outstanding tensile properties. J. Alloys Compd., 2021, 877: 160199.

[39] Qiu Y, Hu YJ, Taylor A, et al. A lightweight single-phase AlTiVCr compositionally complex alloy. Acta Mater., 2017, 123: 115-124.

[40] Ding Q, Zhang Y, Chen X, et al. Tuning element distribution, structure and properties by composition in high-entropy alloys. Nature, 2019, 574: 223-227.

[41] Wang H, He QF, Yang Y. High-entropy intermetallics: from alloy design to structural and functional properties. Rare Met., 2022, 41: 1989-2001.

[42] Tsai KY, Tsai MH, Yeh JW. Sluggish diffusion in co–cr–fe–mn–ni high-entropy alloys. Acta Mater., 2013, 61: 4887-4897.

[43] Dąbrowa J, Kucza W, Cieślak G, et al. Interdiffusion in the FCC-structured Al-Co-Cr-Fe-Ni high entropy alloys: experimental studies and numerical simulations. J. Alloys Compd., 2016, 674: 455-462.

[44] Beke DL, Erdélyi G. On the diffusion in high-entropy alloys. Mater. Lett., 2016, 164: 111-113.

[45] Vaidya M, Trubel S, Murty BS, Wilde G, Divinski SV. Ni tracer diffusion in CoCrFeNi and CoCrFeMnNi high entropy alloys. J. Alloys Compd., 2016, 688: 994-1001.

[46] Zhang C, Zhang F, Jin K, et al. Understanding of the elemental diffusion behavior in concentrated solid solution alloys. J. Ph. Equilibria Diffus., 2017, 38: 434-444.

[47] Li Z, Zhao S, Ritchie RO, Meyers MA. Mechanical properties of high-entropy alloys with emphasis on face-centered cubic alloys. Prog. Mater. Sci., 2019, 102: 296-345.

[48] Zhang W, Liaw PK, Zhang Y. Science and technology in high-entropy alloys. Sci. China Mater, 2018, 61: 2-22.

[49] Tun KS, Charadva V, Gupta M. Lightweight medium entropy magnesium alloy with exceptional compressive strength and ductility combination. J. Mater. Eng. Perform., 2021, 30: 2422-2432.

[50] Shao L, Zhang T, Li L, et al. A low-cost lightweight entropic alloy with high strength. J. Mater. Eng. Perform., 2018, 27: 6648-6656.

[51] Liao YC, Li TH, Tsai PH, et al. Designing novel lightweight, high-strength and high-plasticity Tix(AlCrNb)100-x medium-entropy alloys. Intermetallics, 2020, 117: 106673.

[52] Zhang Y, Zhou YJ, Lin JP, Chen GL, Liaw PK. Solid-solution phase formation rules for multi-component alloys. Adv. Eng. Mater., 2008, 10: 534-538.

[53] Guo S, Hu Q, Ng C, Liu CT. More than entropy in high-entropy alloys: Forming solid solutions or amorphous phase. Intermetallics, 2013, 41: 96-103.

[54] Guo S, Ng C, Lu J, Liu CT. Effect of valence electron concentration on stability of fcc or bcc phase in high entropy alloys. J. Appl. Phys., 2011, 109: 103505.

[55] Couzinié JP, Dirras G. Body-centered cubic high-entropy alloys: From processing to underlying deformation mechanisms. Mater. Charact., 2019, 147: 533-544.

[56] Yang X, Zhang Y. Prediction of high-entropy stabilized solid-solution in multi-component alloys. Mater. Chem. Phys., 2012, 132: 233-238.

[57] Yang X, Chen SY, Cotton JD, Zhang Y. Phase stability of low-density, multiprincipal component alloys containing aluminum, magnesium, and lithium. JOM, 2014, 66: 2009-2020.

[58] Heydari H, Tajally M, Habibolahzadeh A. Computational analysis of novel AlLiMgTiX light high entropy alloys. Mater. Chem. Phys., 2022, 280: 125834.

[59] Heydari H, Tajally M, Habibolahzadeh A. Calculations to introduce some light high entropy alloys based on phase formation rules. J. Alloys Compd., 2022, 912: 165222.

[60] Chauhan P, Yebaji S, Nadakuduru VN, Shanmugasundaram T. Development of a novel light weight Al35Cr14Mg6Ti35V10 high entropy alloy using mechanical alloying and spark plasma sintering. J. Alloys Compd., 2020, 820: 153367.

[61] Kaufman L, Ågren J. CALPHAD, first and second generation–Birth of the materials genome. Scr. Mater., 2014, 70: 3-6.

[62] Baek EJ, Ahn TY, Jung JG, et al. Effects of ultrasonic melt treatment and solution treatment on the microstructure and mechanical properties of low-density multicomponent Al70Mg10Si10Cu5Zn5 alloy. J. Alloys Compd., 2017, 696: 450-459.

[63] Asadikiya M, Zhang Y, Wang L, Apelian D, Zhong Y. Design of ternary high-entropy aluminum alloys (HEAls). J. Alloys Compd., 2022, 891: 161836.

[64] Sanchez JM, Pascual A, Vicario I, et al. Microstructure and Phase Formation of Novel Al80Mg5Sn5Zn5X5 Light-Weight Complex Concentrated Aluminum Alloys. Metals, 2021, 11: 1944.

[65] Gobernik A, Lemay CM, Haddad JG. Modelling and Testing Aluminum Based High Entropy Alloys. Worcester Polytechnic Institute, 2018.

[66] Ahn TY, Jung JG, Baek EJ, Hwang SS, Euh K. Temperature dependence of precipitation behavior of Al–6Mg–9Si–10Cu–10Zn–3Ni natural composite and its impact on mechanical properties. Mater. Sci. Eng. A, 2017, 695: 45-54.

[67] Sanchez JM, Vicario I, Albizuri J, Guraya T, Acuña EM. Design, microstructure and mechanical properties of cast medium entropy aluminium alloys. Sci. Rep., 2019, 9: 6792.

[68] Bilbao Y, Trujillo JJ, Vicario I, et al. X-ray Thermo-Diffraction Study of the Aluminum-Based Multicomponent Alloy Al58Zn28Si8Mg6. Materials, 2022, 15: 5056.

[69] Kim JH, Jung JG, Baek EJ, Choi YS, Euh K. Microstructures and mechanical properties of multiphase-reinforced in situ aluminum matrix composites. Met. Mater. Int., 2019, 25: 353-363.

[70] Li Y, Li R, Zhang Y. Effects of Si addition on microstructure, properties and serration behaviors of lightweight Al-Mg-Zn-Cu medium-entropy alloys. Research and Application of Materials Science, 2019, 1: 13-22.

[71] Feng R, Zhang C, Gao MC, et al. High-throughput design of high-performance lightweight high-entropy alloys. Nat. Commun., 2021, 12: 4329.

[72] Wen J, Liu Y, Huang Y, Zhao Y. Effects of electromagnetic stirring and subsequent homogenization treatment on the microstructure and mechanical properties of Al70Zn10Mg10Cu5Si5 multi-component alloy. J. Alloys Compd., 2023, 960: 170725.

[73] Li R, Wang Z, Guo Z, et al. Graded microstructures of Al-Li-Mg-Zn-Cu entropic alloys under supergravity. Sci. China Mater, 2019, 62: 736-744.

[74] Sahin H, Zengin H. Microstructure, mechanical and wear properties of low-density cast medium and high entropy aluminium alloys. Int. J. Met., 2022, 16: 1976-1984.

[75] Xie Y, Meng X, Zang R, et al. Deformation-driven modification towards strength-ductility enhancement in Al–Li–Mg–Zn–Cu lightweight high-entropy alloys. Mater. Sci. Eng. A, 2022, 830: 142332.

[76] Chen ZP, Yu H, Wu Y, et al. Nano-network mediated high strength and large plasticity in an Al-based alloy. Mater. Lett., 2012, 84: 59-62.

[77] Li Z, Li X, Huang Z, et al. Ultrasonic-vibration-enhanced plasticity of an entropic alloy at room temperature. Acta Mater., 2022, 225: 117569.

[78] Singh N, Shadangi Y, Mukhopadhyay NK. Phase evolution and thermal stability of low-density MgAlSiCrFe high-entropy alloy processed through mechanical alloying. Trans. Indian Inst. Met., 2020, 73: 2377-2386.

[79] Singh N, Shadangi Y, Goud GS, et al. Fabrication of MgAlSiCrFe low-density high-entropy alloy by mechanical alloying and spark plasma sintering. Trans. Indian Inst. Met., 2021, 74: 2203-2219.

[80] Wu S, Zhu B, Jiang W, Qiu H, Guo Y. Hot Deformation Behavior and Microstructure Evolution of a Novel Al-Zn-Mg-Li-Cu Alloy. Materials, 2022, 15: 6769.

[81] Cui L, Zhang Z, Chen XG. Microstructure and mechanical properties of novel Al–Cu–Mg–Zn lightweight entropy alloys for elevated-temperature applications. Mater. Charact., 2023, 200: 112927.

[82] Kim I, Song M, Kim J. Effects of Ti–B and Si additions on microstructure and mechanical properties of Al–Cu–Mg based aluminum matrix composites. J. Alloys Compd., 2020, 832: 154827.

[83] Sadeghi M, Niroumand B. Design and characterization of a novel MgAlZnCuMn low melting point light weight high entropy alloy (LMLW-HEA). Intermetallics, 2022, 151: 107658.

[84] Li R, Gao JC, Fan K. Microstructure and mechanical properties of MgMnAlZnCu high entropy alloy cooling in three conditions. In Materials Science Forum, 2011, 686: 235-241.

[85] Jiang W, Tao S, Qiu H, Wu S, Zhu B. Precipitation transformation and strengthening mechanism of droplet ejection lightweight medium-entropy AlZnMgCuLi alloy. J. Alloys Compd., 2022, 922: 166152.

[86] Li R, Li X, Ma J, Zhang Y. Sub-grain formation in Al–Li–Mg–Zn–Cu lightweight entropic alloy by ultrasonic hammering. Intermetallics, 2020, 121: 106780.

[87] Zhang B, Liaw PK, Brechtl J, et al. Effects of Cu and Zn on microstructures and mechanical behavior of the medium-entropy aluminum alloy. J. Alloys Compd., 2020, 820: 153092.

[88] Hu Y, Liu YY, Zhao LZ, et al. Investigation on microstructures and properties of semi-solid Al80Mg5Li5Zn5Cu5 light-weight high-entropy alloy during isothermal heat treatment process. China Foundry, 2022, 19: 519-527.

[89] Srivatsan TS, Gupta M. High entropy alloys: innovations, advances, and applications. Boca Raton, 2020.

[90] Roy A, Babuska T, Krick B, Balasubramanian G. Machine learned feature identification for predicting phase and Young's modulus of low-, medium-and high-entropy alloys. Scr. Mater., 2020, 185: 152-158.

[91] Chaskis S, Stachouli E, Gavalas E, Bouzouni M, Papaefthymiou S. Microstructure, Phase Formation and Heat-Treating of Novel Cast Al-Mg-Zn-Cu-Si Lightweight Complex Concentrated Aluminum Based Alloy. Materials, 2022, 15: 3169.

[92] Kilmametov A, Kulagin R, Mazilkin A, et al. High-pressure torsion driven mechanical alloying of CoCrFeMnNi high entropy alloy. Scr. Mater., 2019, 158: 29-33.

[93] Nguyen NTC, Asghari-Rad P, Sathiyamoorthi P, et al. Ultrahigh high-strain-rate superplasticity in a nanostructured high-entropy alloy. Nat. Commun., 2020, 11(1): 2736.

[94] Huang Y, Wen J, Liu Y, Zhao Y. Effects of electromagnetic frequency on the microstructure and mechanical properties of Al70Zn10Mg10Cu5Si5 medium entropy alloy. J. Mater. Res. Technol., 2022, 17: 3105-3117.

[95] Seo N, Jeon J, Lee SH, et al. Revealing complex precipitation behavior of multicomponent Al83Zn5Cu5Mg5Li2 alloy. J. Alloys Compd., 2023, 944: 169192.

[96] Ashby MF. Materials Selection in Mechanical Design. Burlington, 2011.

[97] Leng L, Zhang ZJ, Duan QQ, Zhang P, Zhang ZF. Improving the fatigue strength of 7075 alloy through aging. Mater. Sci. Eng. A, 2018, 738: 24-30.

[98] Zou Y, Wu X, Tang S, et al. Investigation on microstructure and mechanical properties of Al-Zn-Mg-Cu alloys with various Zn/Mg ratios. J. Mater. Sci. Technol., 2021, 85: 106-117.

[99] Jeon C, Kim CP, Joo SH, Kim HS, Lee S. High tensile ductility of Ti-based amorphous matrix composites modified from conventional Ti–6Al–4V titanium alloy. Acta Mater., 2013, 61: 3012-3026.

[100] Polmear IJ, Couper MJ. Design and development of an experimental wrought aluminum alloy for use at elevated temperatures. Metall. Trans. A, 1988, 19: 1027-1035.

[101] Awe SA. Elevated temperature tensile properties of a ternary eutectic Al–27% Cu–5% Si cast alloy. Int. J. Lightweight Mater., 2021, 4: 18-26.

[102] Awe SA, Seifeddine S, Jarfors A EW, Lee C, Dahle AK. Development of new Al-Cu-Si alloys for high temperature performance. Adv. Mater. Lett., 2017, 8: 695-701.

[103] Ahn TY, Jung JG, Baek EJ, Hwang SS, Euh K. Temporal evolution of precipitates in multicomponent Al–6Mg–9Si–10Cu–10Zn–3Ni alloy studied by complementary experimental methods. J. Alloys Compd., 2017, 701: 660-668.

[104] Cui L, Zhang Z, Sarkar DK, Kocaefe D, Chen XG. A Study on Aluminum-Based Lightweight Entropic Alloys with High Strength at Elevated Temperature. In: Proceedings of the 61st Conference of Metallurgists, 2022, 413-423.

[105] Cui L, Liu K, Zhang Z, Chen XG. Enhanced elevated-temperature mechanical properties of hot-rolled Al–Cu alloys: effect of zirconium addition and homogenization. J. Mater. Sci., 2023, 58: 11424–11439.

[106] Ibrahim PA, Özkul İ, Canbay CA. An overview of high-entropy alloys. Emergent Mater., 2022, 5: 1779-1796.

[107] Luo AA, Sachdev AK, Apelian D. Alloy development and process innovations for light metals casting. J. Mater. Process. Technol., 2022, 306: 117606.

[108] Zhang H, Fu H, Zhu S, Yong W, Xie J. Machine learning assisted composition effective design for precipitation strengthened copper alloys. Acta Mater., 2021, 215: 117118.

[109] Dai D, Xu T, Wei X, et al. Using machine learning and feature engineering to characterize limited material datasets of high-entropy alloys. Comput. Mater. Sci., 2020, 175: 109618.

[110] Wang AYT, Murdock RJ, Kauwe SK, et al. Machine learning for materials scientists: an introductory guide toward best practices. Chem. Mater., 2020, 32: 4954-4965.

[111] Kaufmann K, Vecchio KS. Searching for high entropy alloys: A machine learning approach. Acta Mater., 2020, 198: 178-222.

[112] Liu X, Xu P, Zhao J, et al. Material machine learning for alloys: Applications, challenges and perspectives. J. Alloys Compd., 2022, 921: 165984.

[113] Liu Y, Zhao T, Ju W, Shi S. Materials discovery and design using machine learning. J. Materiomics., 2017, 3: 159-177.

[114] Wu L, Wei G, Wang G, Wang H, Ren J. Creating win-wins from strength-ductility trade-off in multi-principal element alloys by machine learning. Mater. Today Commun., 2022, 32: 104010.

[115] Lian Z, Li M, Lu W. Fatigue life prediction of aluminum alloy via knowledge-based machine learning. Int. J. Fatigue, 2022, 157: 106716.

[116] Jaafreh R, Chaudry UM, Hamad K, Abuhmed T. Age-hardening behavior guided by the multi-objective evolutionary algorithm and machine learning. J. Alloys Compd., 2022, 893: 162104.

[117] Jiang L, Wang C, Fu H, et al. Discovery of aluminum alloys with ultra-strength and high-toughness via a property-oriented design strategy. J. Mater. Sci. Technol., 2022, 98: 33-43.

[118] Li H, Li X, Li Y, et al. Machine learning assisted design of aluminum-lithium alloy with high specific modulus and specific strength. Mater. Des., 2023, 225: 111483.

[119] Juan Y, Niu G, Jiang H, et al. Machine Learning-Assisted Design of Al-Zn-Mg-Cu Alloys with Dramatically Enhanced Combination of Mechanical Strength and Plasticity. Available at SSRN 4244660, 2022.

[120] Pei Z, Yin J, Liaw PK, Raabe D. Toward the design of ultrahigh-entropy alloys via mining six million texts. Nat. Commun., 2023, 14: 54.

[121] Islam N, Huang W, Zhuang HL. Machine learning for phase selection in multi-principal element alloys. Comput. Mater. Sci., 2018, 150: 230-235.

[122] Zhang Y, Wen C, Wang C, et al. Phase prediction in high entropy alloys with a rational selection of materials descriptors and machine learning models. Acta Mater., 2020, 185: 528-539.

[123] Yan Y, Lu D, Wang K. Accelerated discovery of single-phase refractory high entropy alloys assisted by machine learning. Comput. Mater. Sci., 2021, 199: 110723.

[124] Euh K, Jung JG, Baek EJ, Lee JM, Kim HW. Effect of heat-treatment on microstructure and mechanical properties of sonicated multicomponent AlMgSiCuZn alloy. In Light Metals, 2017, 379-383.

[125] Huang Z, Dai Y, Li Z, et al. Investigation on surface morphology and crystalline phase deformation of Al80Li5Mg5Zn5Cu5 high-entropy alloy by ultra-precision cutting. Mater. Des., 2020, 186: 108367.

[126] Wang N, Wu B, Wu W, et al. Microstructure and properties of aluminium-high entropy alloy composites fabricated by mechanical alloying and spark plasma sintering. Mater. Today Commun., 202, 25: 101366.

[127] Yang X, Zhang H, Dong P, Yan Z, Wang W. A study on the formation of multiple intermetallic compounds of friction stir processed high entropy alloy particles reinforced Al matrix composites. Mater. Charact., 2022, 183: 111646.

[128] Lu T, Scudino S, Chen W, et al. The influence of nanocrystalline CoNiFeAl0.4Ti0.6Cr0.5 high-entropy alloy particles addition on microstructure and mechanical properties of SiCp/7075Al composites. Mater. Sci. Eng. A, 2018, 726: 126-136.

[129] Shadangi Y, Chattopadhyay K, Mukhopadhyay NK. Powder metallurgical processing of Al matrix composite reinforced with AlSiCrMnFeNiCu high-entropy alloys: Microstructure, thermal stability, and microhardness. J. Mater. Res., 2023, 38: 248-264.

[130] Sudha P, Tun KS, Gupta M, Mourad AHI, Vincent S. Electrochemical characterization of a novel multicomponent Al75Mg5Li10Zn5Cu5 low entropy alloy in different pH environments. Mater. Corros., 2022, 73: 2071-2083.

[131] Xie Y, Meng X, Mao D, et al. Deformation-driven modification of Al-Li-Mg-Zn-Cu high-alloy aluminum as anodes for primary aluminum-air batteries. Scr. Mater., 2022, 212: 114551.

[132] Kairy SK, Rometsch PA, Davies CHJ, Birbilis N. On the intergranular corrosion and hardness evolution of 6xxx series Al alloys as a function of Si: Mg ratio, Cu content, and aging condition. Corrosion, 2017, 73: 1280-1295.

[133] Feng R, Gao MC, Lee C, et al. Design of light-weight high-entropy alloys. Entropy, 2016, 18: 333.

[134] Yi W, Liu G, Gao J, Zhang L. Boosting for concept design of casting aluminum alloys driven by combining computational thermodynamics and machine learning techniques. Journal of Materials Informatics, 2021, 1: 11.

[135] Jeong IS, Lee JH. Single-phase lightweight high-entropy alloys with enhanced mechanical properties. Mater. Des., 2023, 227: 111709.

[136] Saal JE, Kirklin S, Aykol M, Meredig B, Wolverton C. Materials design and discovery with high-throughput density functional theory: the open quantum materials database (OQMD). JOM, 2013, 65: 1501-1509.

[137] Li R, Xie L, Wang WY, Liaw PK, Zhang Y. High-throughput calculations for high-entropy alloys: a brief review. Front. Mater. Sci., 2020, 7: 290.

[138] Schmid-Fetzer R, Zhang F. The light alloy Calphad databases PanAl and PanMg. Calphad, 2018, 61: 246-263.

[139] Senkov ON, Miller JD, Miracle DB, Woodward C. Accelerated exploration of multi-principal element alloys with solid solution phases. Nat. Commun., 2015, 6: 6529.

Chapter 3

Microstructure and mechanical properties of novel Al–Cu–Mg–Zn lightweight entropy alloys for elevated-temperature applications

(Published in *Materials Characterization*)

Abstract

In this study, the microstructural evolution and mechanical properties of five lightweight Al–Cu–Mg–Zn entropy alloys ($Al_{85}Cu_5Zn_5Mg_5$, $Al_{74}Cu_{10}Zn_8Mg_8$, $Al_{93}Cu_4Zn_1Mg_1Cr_1$, $Al_{84}Cu_{10}Zn_3Mg_2Cr_1$, and $Al_{77}Cu_{17}Zn_3Mg_2Cr_1$) were investigated. The five experimental alloys revealed lightweight characteristics with density values ranging from 2.95 to 3.63 g/cm^3 and multiphase features. The microstructural and phase evolutions at elevated-temperature were characterized using X-ray diffraction and optical, scanning, and transmission electron microscopy. With the increase in Cu and other element contents, the volume fraction of intermetallic compounds (ICs) increased, resulting in an improved yield strength (YS) and reduced plasticity. The GP zone and fine η' precipitates were effective strengthening sources in fcc-Al, but they were unstable at 300 °C and transformed into coarse and submicron-sized particles. The main source of strengthening in the alloy series was the well-interconnected IC network. Among the five alloys studied, Alloy 5 ($Al_{77}Cu_{17}Zn_3Mg_2Cr_1$) exhibited the highest YS of 588 MPa at room temperature and retained the highest YS of 199 MPa at 300 °C after thermal exposure for 100 h. Combining its high strength and good thermal stability at 300 °C, Alloy 5 exhibits promising potential for elevated-temperature applications.

Keywords: Al-based entropy alloys, Microstructure, Intermetallic compounds, Mechanical properties.

3.1 Introduction

Al and its alloys have played a significant role in the automotive, aerospace, and infrastructure industries; however, their applications are greatly limited by their deteriorated mechanical behavior at high temperatures [1, 2]. With the development of the green economy, the demand for lightweight Al alloys with better mechanical behavior at elevated temperatures is significantly increasing.

A class of newly emerging alloys known as high-entropy alloys (HEAs) has attracted wide attention since 2004 [3, 4]. The design concept behind HEAs is to obtain a high entropy value by adding multiple principal elements in equal or near-equal atomic ratios to facilitate the formation of disordered solid solutions and endow the alloys with unique properties [5, 6]. Over the years, numerous studies have been conducted on HEAs [7]. With many new findings, the initial concept has largely expanded, and alloys of different entropy values having exceptional mechanical and material properties have been explored, including high-entropy, medium-entropy, and low-entropy alloys [7-10]. In addition, the phase formation of entropy alloys can be simple as a single disordered solid solution or complex as multicomponent intermetallic phases [5,7]. Inspired by the concept of entropy alloys, the introduction of Al alloys with enhanced entropy provides a new avenue and wide composition space for designing Al-based alloys with promising properties, such as high strength,

excellent thermal resistance, and high fatigue resistance, which cannot be achieved in conventional Al alloys [5,7].

Al-based entropy alloys are intentionally designed to obtain a higher entropy value by adding a larger quantity of secondary elements to the Al matrix; the resulting materials are also often called multicomponent Al alloys in the literature [11-14]. In traditional commercial Al alloys, Cu, Mg, and Zn are the main alloying elements used to improve the mechanical properties. For instance, Al–Zn–Mg–Cu 7xxx alloys have a reputation for excellent mechanical properties, particularly at room temperature [15]. Among conventional Al alloys, Al–Cu 2xxx alloys exhibit promising potential for high-temperature applications [16]. In current Al-based lightweight entropy alloy studies, Cu, Mg, and Zn are also widely adopted [12, 13, 17-20]. Yang et al. [12] reported an entropy alloy of $Al_{80}Li_5Mg_5Zn_5Cu_5$ that had a low density of 3.08 g/cm^3 and high compressive fracture strength of 879 MPa with a plasticity of up to 17%. Shao et al. [13] designed and studied a series of Al–Mg-based lightweight entropy alloys with low densities in the range of 2.64–2.75 g/cm^3; one of the alloys studied, $Al_{85}Mg_{10.5}Zn_{2.025}Cu_{2.025}Si_{0.45}$, exhibited an excellent compressive strength of 814 MPa with a plasticity percentage of 24.8%. Li et al. [20] studied a high-Zn Al-based entropy alloy, $Al_{80}Zn_{14}Li_2Mg_2Cu_2$, which exhibited high compressive strength (>1 GPa) and high plasticity (>20%) in the as-cast state. The above work shows that the room-temperature mechanical property of Al–Cu–Mg–Zn entropy alloys is promising. However, very limited studies and related information on the high-temperature mechanical performance, thermal stability, and corresponding microstructures of Al-based entropy alloys are available in the current literature.

To explore the potential of Al–Cu–Mg–Zn lightweight entropy alloys for elevated-temperature applications, in this study, five alloys are designed and investigated: $Al_{85}Cu_5Zn_5Mg_5$, $Al_{74}Cu_{10}Zn_8Mg_8$, $Al_{93}Cu_4Zn_1Mg_1Cr_1$, $Al_{84}Cu_{10}Zn_3Mg_2Cr_1$, and $Al_{77}Cu_{17}Zn_3Mg_2Cr_1$. This alloy series significantly increases the chemical composition space of conventional Al–Cu alloys by adding large amounts of Cu, Mg, Zn, and Cr. The ratio of the elements was adjusted to obtain balanced empirical thermodynamic parameters, including the mixing entropy, enthalpy, and density, as described in our previous study [21]. Cu was added at a relatively high content, which was intended to improve the mechanical behavior at elevated temperatures. Cr, which has a high melting point, was further added to the Al–Cu–Mg–Zn system to facilitate the formation of the heat-resistant $Al_{45}Cr_7$ phase at elevated temperatures [21]. The phase formation, microstructure evolution, mechanical performance at room and elevated temperatures, and thermal stability during thermal exposure of the five experimental alloys were systematically studied.

3.2 Experimental procedures

Five experimental alloys were prepared using an induction melting furnace. The pure raw materials Al bulks (> 99.2%), Cu bulks (> 99.5%), Mg bulks (> 99.5%), Zn slugs (> 99.9%), and Cr granules (> 99.9%) were melted in a graphite crucible under an argon atmosphere. The melting temperature was set to 880 °C, and elements could be melted through diffusion in Al melts. Each alloy was remelted three times, and before each remelting, the cast ingot was ground to remove the oxide film and flipped in the crucible to promote homogeneous distribution of the alloying elements. The molten metal was finally cast into a copper mold with dimensions of $26 \times 26 \times 50$ mm^3,

which was preheated to 250 °C. The chemical compositions of the experimental alloys were analyzed using inductively coupled plasma mass spectrometry, and the results are listed in Table 3.1. To study the thermal stability of the alloys, some of the ingot samples were thermally exposed at 300 °C for up to 200 h.

Table 3.1 Chemical compositions of five experimental alloys.

Code	Alloys	Chemical composition / at.%				
		Al	Cu	Zn	Mg	Cr
Alloy 1	$Al_{85}Cu_5Zn_5Mg_5$	85.72	5.08	4.02	5.18	-
Alloy 2	$Al_{74}Cu_{10}Zn_8Mg_8$	74.02	10.48	7.17	8.33	-
Alloy 3	$Al_{93}Cu_4Zn_1Mg_1Cr_1$	92.72	4.06	1.26	0.99	0.97
Alloy 4	$Al_{84}Cu_{10}Zn_3Mg_2Cr_1$	84.67	9.73	2.70	1.83	1.07
Alloy 5	$Al_{77}Cu_{17}Zn_3Mg_2Cr_1$	77.28	17.34	2.48	1.80	1.10

X-ray diffraction (XRD; D8 Discover) with Cu Kα radiation was used to identify the crystal structures of the alloy phases. The diffraction angle (2θ) ranged from 10° to 80°, with a step size of 0.05° and a step time of 0.5 s/step. The microstructures of the alloys were investigated using optical microscopy (OM; Nikon Eclipse ME600) and scanning electron microscopy (SEM; JEOL JSM-6480LV) equipped with energy-dispersive X-ray spectroscopy (EDS). Transmission electron microscopy (TEM; JEM−2100) with an accelerating voltage of 200 kV was used to characterize the precipitates and identify the fine-scaled Mg–Zn phase. Differential scanning calorimetry (DSC; PerkinElmer DSC 8000) was used for the as-cast samples at a heating rate of 10 °C/min under an argon atmosphere. To study the spatial distribution of the phases, three-dimensional (3D) reconstruction was performed based on two-dimensional (2D) SEM images. The reconstruction was achieved using manual serial sectioning and 3D visualization software (Materialise Mimics). The specific operating

procedure for serial sectioning was described in [22, 23]. For each reconstructed alloy, a total of 21 SEM images were captured. The microstructure was aligned and transformed into black and white images using image analysis software (ImageJ), so that different phases could be easily recognized by adjusting the grayscale threshold in the 2D stack and used for 3D rendering [23, 24].

For the mechanical properties, compression tests were conducted at 20 °C and 300 °C using a Gleeble 3800 thermomechanical simulator unit under the guidance of ASTM E9-09 and ASTM E209-18 standards. The samples were machined into cylindrical forms with diameters and lengths of 8 and 12 mm, respectively. The compressive strain rate was 10^{-3} s^{-1}. At least two samples were tested for each condition. The Vickers microhardness of the samples was measured on a polished sample surface using a microhardness testing machine (NG−1000 CCD) with a load of 200 g and a dwell time of 15 s.

3.3 Results and discussion

3.3.1 Microstructure and phase formation of as-cast alloys

Fig. 3.1 presents the XRD patterns of as-cast Alloys 1–5. Three to four phases were indexed in each alloy; the fcc-Al and Al_2Cu phases were observed in all alloys. The intensities of the diffraction peaks reflect the contents of the corresponding phases. The contents of fcc and Al_2Cu in each alloy were different. Fig. 3.1a–d display the most intense fcc-Al peaks, indicating that fcc-Al is the major phase in Alloys 1–4, while Fig. 3.1e shows that Al_2Cu peaks are the strongest, and hence Al_2Cu becomes the predominant phase, in Alloy 5. Owing to the massive addition of Zn and Mg in Alloys

1–2, a large amount of $MgZn_2$ was detected. The Al_2CuMg phase was particularly detected in Alloy 1 (Fig. 3.1a). The Cu/Mg ratio has been reported to affect the type of intermetallic compounds (ICs) in Al alloys, and a decreasing Cu/Mg ratio promotes the formation of Al_2CuMg [25, 26]. According to Table 3.1, Alloy 1 had the smallest Cu/Mg ratio, indicating a greater tendency to form Al_2CuMg than the other alloys. In Fig. 3.1c–e, peaks of $Al_{45}Cr_7$ are observed because of the addition of Cr to Alloys 3–5.

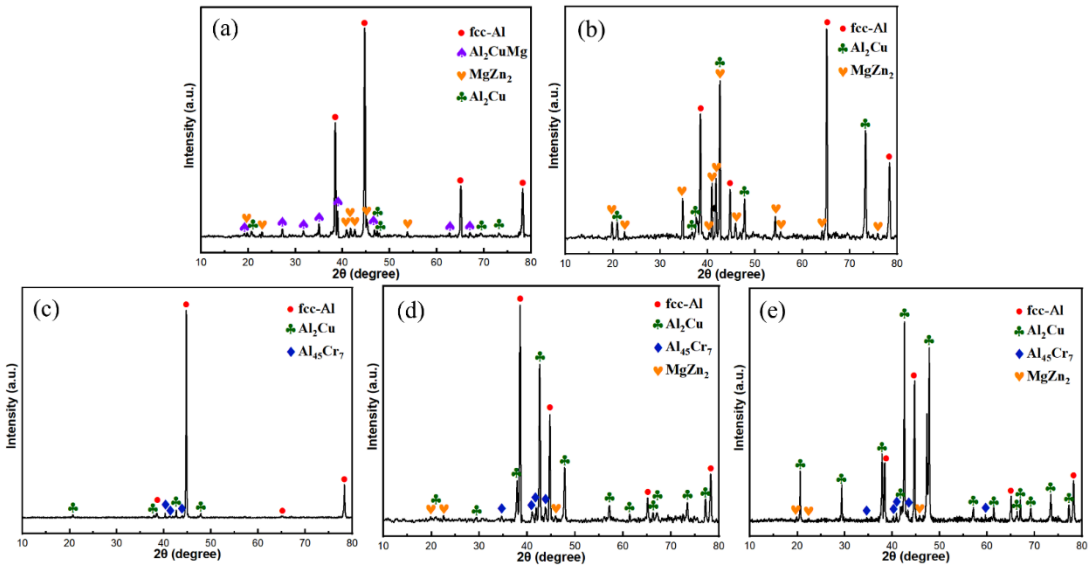

Fig. 3.1 XRD patterns of as-cast alloys: (a) Alloy 1, (b) Alloy 2, (c) Alloy 3, (d) Alloy 4, and (e) Alloy 5.

Typical SEM images of the as-cast alloys are shown in Fig. 3.2. Three to four regions (marked as A, B, C, D, and E) with corresponding phases were identified in each alloy according to the shape, brightness, and SEM–EDS results combined with the XRD patterns. The phase type, volume fraction, and chemical composition of each phase in the corresponding microstructure regions are listed in Table 3.2. The volume fraction of each phase was obtained by quantifying at least five OM images (not shown here), covering an area of more than 78 000 μm^2. Dark region A is fcc-Al, which was

the dominant phase in Alloys 1–4. Region B is Al_2CuMg, containing a small amount of Zn, which was only detected in Alloy 1. Region C is $MgZn_2$, which constitutes a fine lamellar eutectic structure with fcc-Al that comprised 28.69 vol.% in Alloy 2, while it was present only in small amounts in Alloys 3–5. Region D is Al_2Cu, and its volume fraction significantly increased with increasing Cu content in Alloys 4–5. Region E is $Al_{45}Cr_7$, which appeared in Alloys 3–5. The phase constituents and microstructures revealed by OM and SEM are in very good agreement with the XRD results, except that $MgZn_2$ was observed in the microstructure of Alloy 3, but it was not detected in the XRD patterns because of its trace content in this alloy (0.12 vol.%).

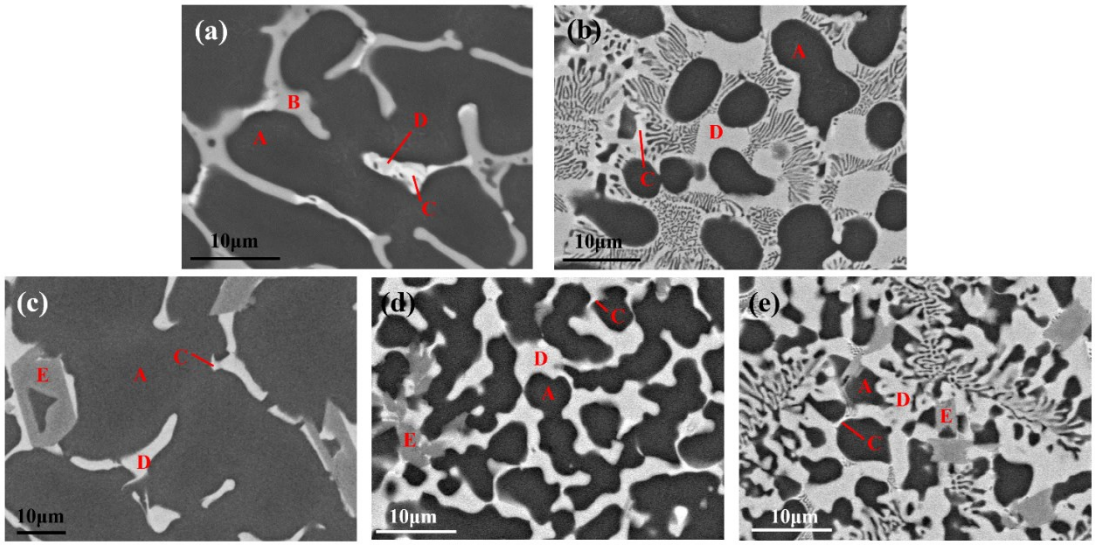

Fig. 3.2 SEM backscattered electron images of the as-cast alloys: (a) Alloy 1, (b) Alloy 2, (c) Alloy 3, (d) Alloy 4, and (e) Alloy 5.

The microstructures of the as-cast alloys exhibit a multiphase character. This is a common feature in lightweight entropy alloys owing to the large chemical difference and high negative enthalpy between elements [12, 27]. As listed in Table 3.2, the fcc-Al in Alloy 2 contains 2.5 at.% Cu, 3.5 at.% Zn, and 1 at.% Mg, which are much higher than the contents of conventional Al alloys. This could be a result of the sluggish

diffusion effect in entropy alloys [21, 28]. Among the multiple phases, fcc-Al has a face-centered cubic structure with many slip systems; the remaining phases are ICs of Al_2CuMg, Al_2Cu, $MgZn_2$, and $Al_{45}Cr_7$, which belong to orthorhombic, tetragonal, hexagonal, and monoclinic crystal systems, respectively. Accordingly, these ICs with much fewer slip systems are expected to bring high strength and low plasticity to the experimental alloys. The physical properties of the ICs in the literature are summarized in Table 3.3 [29-31].

Table 3.2 Chemical composition and volume fraction of each phase in the as-cast alloys.

Alloy	Density, g/cm^3	Region	Phase type	Volume fraction, vol.%	Chemical composition, at.%				
					Al	Cu	Zn	Mg	Cr
Alloy 1	3.02	A	fcc-Al	80.55	94.5	1.5	2.5	1.5	-
		B	Al_2CuMg	14.19	62	16	2	20	-
		C	$MgZn_2$	4.65	60	11	15	14	-
		D	Al_2Cu	0.61	69	25	3	3	-
Alloy 2	3.35	A	fcc-Al	52.96	93	2.5	3.5	1	-
		C	$MgZn_2$	28.69	63	11	12	14	-
		D	Al_2Cu	18.35	68	30	1	1	-
Alloy 3	2.95	A	fcc-Al	85.05	96	1.5	1.5	1	-
		C	$MgZn_2$	0.12	79	11	5	5	-
		D	Al_2Cu	9.71	71	28	1	-	-
		E	$Al_{45}Cr_7$	5.12	85	2	1	-	12
Alloy 4	3.27	A	fcc-Al	63.82	94	2	3	1	-
		C	$MgZn_2$	0.33	74	11	7	8	-
		D	Al_2Cu	29.34	70	29	1	-	-
		E	$Al_{45}Cr_7$	6.51	83	4	2	-	11
Alloy 5	3.63	A	fcc-Al	33.45	93.5	2.5	3	1	-
		C	$MgZn_2$	0.55	71	11	7	10	-
		D	Al_2Cu	58.33	70	29	1	-	-
		E	$Al_{45}Cr_7$	7.67	79	9	2	-	10

Table 3.3 Physical properties of intermetallic phases in as-cast Alloys 1–5.

Phase	Structure	Microhardness at RT, GPa	Microhardness at 300 °C, GPa	Reference
Al_2CuMg	orthorhombic	4.44	2.22*	[29]
$MgZn_2$	hexagonal	3.2	0.6+	[30, 31]
Al_2Cu	tetragonal	5.3	2*	[29]
$Al_{45}Cr_7$	monoclinic	5.2	3.72*	[29]

Note: * Tested from 300 °C/1 h thermally exposed samples.
+ Converted from yield strength σ_y in [31] by empirical formula $HV \approx 3\sigma_y$.

3.3.2 Mechanical performance at room and elevated temperatures

The compressive mechanical properties of the as-cast alloys at room temperature are shown in Fig. 3.3. According to the true stress–strain curves in Fig. 3.3a, the five as-cast alloys exhibit different mechanical performances. Alloy 1 and Alloy 3 have relatively high plasticities of 8.62% and 13.6%, respectively, whereas Alloys 2, 4, and 5 fractured during the tests, with true strains of 0.90%, 1.69%, and 0.72%, respectively. The low plasticity of Alloys 2, 4, and 5 was caused by their high IC contents; however, the high IC content significantly improved the yield strength (YS). A close correlation between the YS and IC content is observed, as shown in Fig. 3.3b. Alloy 3 had the lowest IC content of 15 vol.% and the lowest YS of 330 MPa, while Alloy 5 with the highest IC content of 67 vol.% exhibited the highest YS of 588 MPa. Apart from the IC content, the type of IC is also important. Compared with Alloy 2, Alloy 4 had a lower IC content but a higher YS because Al_2Cu and $Al_{45}Cr_7$ in Alloy 4 can contribute more strength than the major $MgZn_2$ in Alloy 2, as listed in Table 3.3.

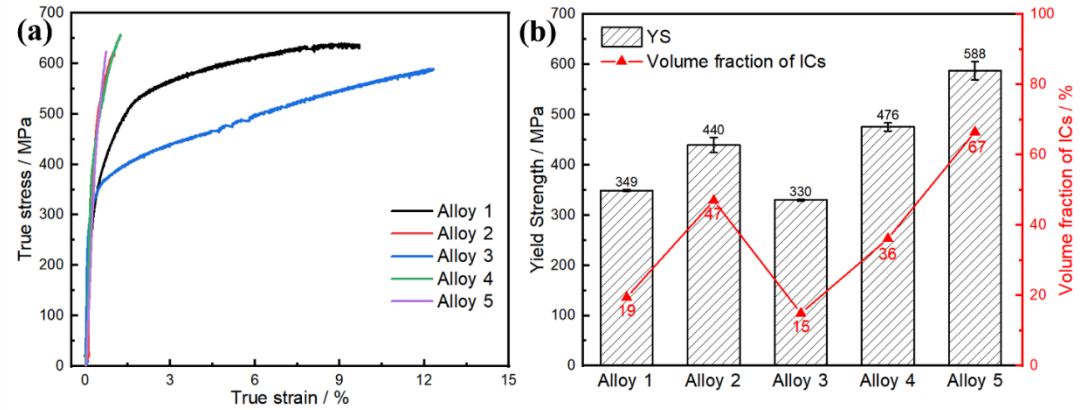

Fig. 3.3 Room-temperature mechanical properties: (a) true stress–strain curves and (b) YS and IC contents of the as-cast alloys.

Fig. 3.4 shows the compressive mechanical properties of as-cast Alloys 1–5 at 300 °C. Compared with the compression tests at room temperature (Fig. 3.3), the plasticity of Alloys 1–5 was significantly improved at 300 °C, as the compression tests at 300 °C automatically stopped upon reaching the preset engineering strain of 20%. The YS and maximum compressive strength of all five alloys exceeded 100 MPa: Alloy 1 had the lowest YS of 101 MPa and a maximum compressive strength of 118 MPa, whereas Alloy 5 showed the highest YS of 212 MPa and a maximum compressive strength of 257 MPa. The change in compressive strength among the five alloys at 300 °C exhibited a similar trend to that at room temperature. However, unlike the room temperature tests, Alloy 3 exhibited a higher YS and maximum compressive strength than those of Alloy 1 at 300 °C. This is attributed to the different heat resistances of the different types of ICs in the two alloys. As listed in Table 3.3, the main ICs in the two alloys have close microhardness values of 3–5 GPa at room temperature. Therefore, Alloy 3 had lower room-temperature strength than Alloy 1 due to its lower ICs content (Table 3.2). However, at 300 °C, the strength of the main intermetallics in Alloy 3 (Al_2Cu: 2 GPa, $Al_{45}Cr_7$: 3.72 GPa) is higher than that in Alloy 1 (Al_2CuMg:

2.22 GPa, $MgZn_2$: 0.6 GPa). This indicates that the intermetallics in Alloy 3 are more heat-resistant than those in Alloy 1. Therefore, the overall IC contribution in Alloy 3 at 300 °C was more significant than that in Alloy 1, resulting in the higher strengths of Alloy 3.

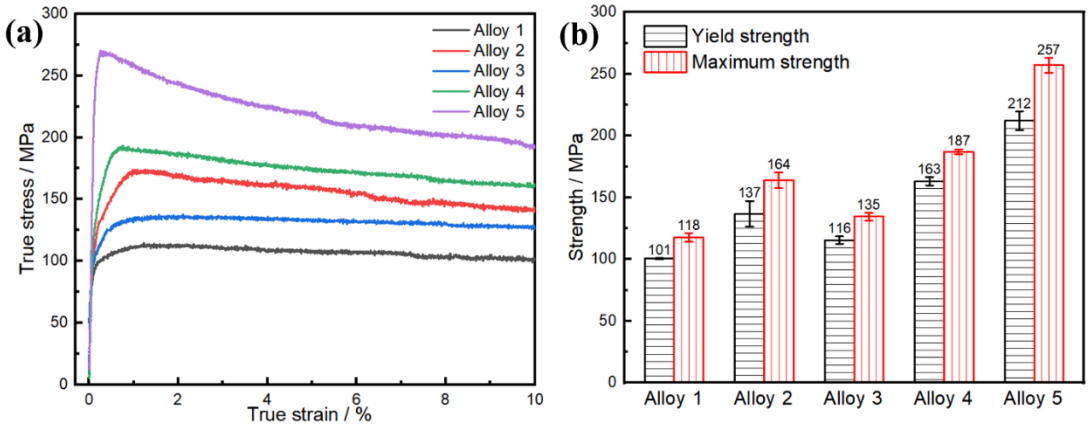

Fig. 3.4 Mechanical properties of the as-cast alloys at 300 °C: (a) true stress–strain curves and (b) yield and maximum strengths.

For alloys used in high-temperature applications, the thermal stability of the microstructure at elevated temperatures is vitally important. In this study, the experimental alloys were thermally exposed at 300 °C for up to 200 h. Fig. 3.5a shows the HV hardness measured at room temperature for Alloys 1–5 as a function of the thermal exposure time. A significant decrease in HV hardness was observed in the first 5 h of thermal exposure, and the HV hardness remained almost stable with further prolonged exposure, indicating that the microstructures of all alloys were thermally stable after the initial 5 h of thermal exposure. Compression tests at 300 °C were conducted on the 300 °C/100 h exposed samples, and the results are shown in Fig. 3.5b. The results reveal that Alloy 1 still had the lowest strength values, and Alloy 5 exhibited the highest strength values, with a YS of 199 MPa and a maximum compressive

strength of 234 MPa. Compared with the results under the as-cast condition in Fig. 3.4b, the strengths of all alloys after 100 h of thermal exposure decreased but varied by different degrees. The percentages of HV reduction and YS decrease after the 300 °C/100 h exposure as a function of fcc-Al content are plotted in Fig. 3.5c. The near-linear relationship between the mechanical reduction and fcc-Al content indicates that the strength decreases during the first 5 h of thermal exposure is closely related to the fcc-Al phase.

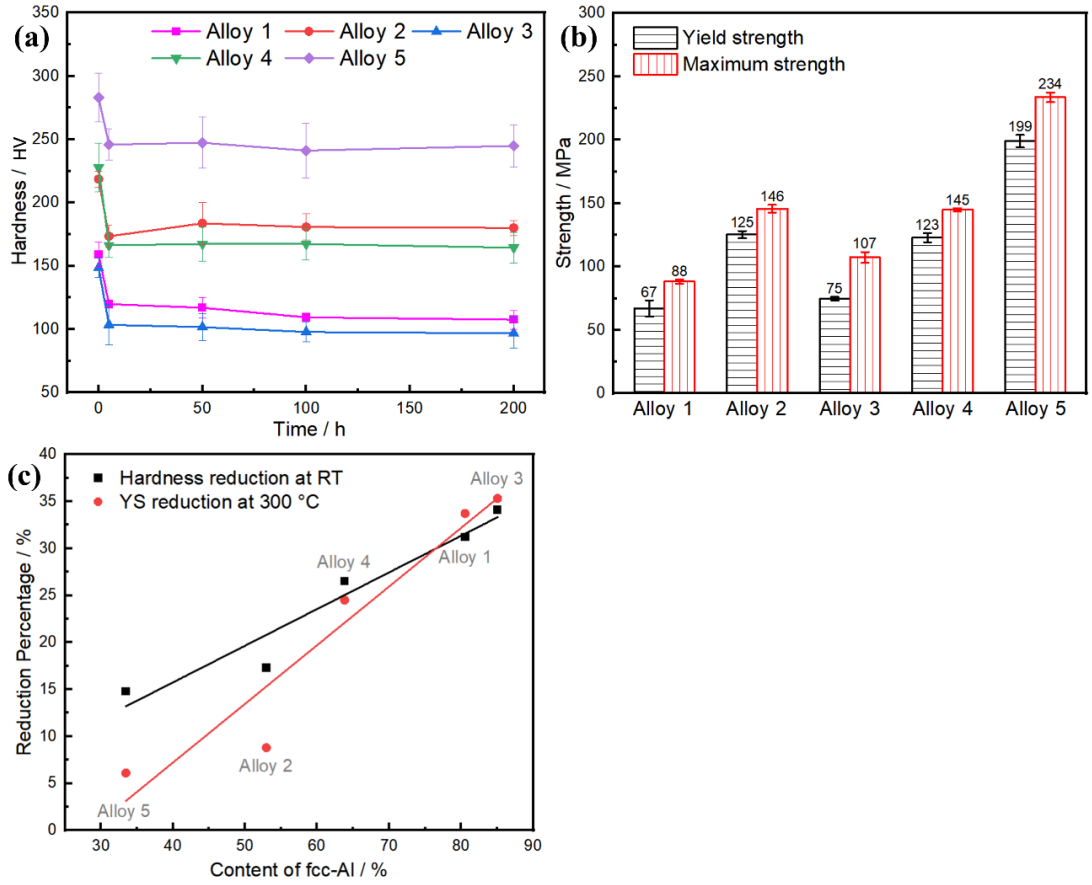

Fig. 3.5 (a) Microhardness of alloys at room temperature with various exposure times, (b) compressive strengths at 300 °C after 300 °C/100 h exposure, and (c) percentages of HV and YS reduction after 300 °C/100 h exposure vs. the content of fcc-Al.

3.3.3 Evolution of the microstructures during thermal exposure

Because fcc-Al clearly affects the thermal stability and strength reduction during initial thermal exposure, a TEM investigation of the evolution of fcc-Al was performed for Alloys 1 and 3, which contained the highest fraction of fcc-Al among the five experimental alloys. As shown in Fig. 3.6a–b, a large number of nanoscale precipitates in fcc-Al were observed along the $<001>_{Al}$ axis, which were identified as η' (metastable phase of $MgZn_2$) according to the selected area diffraction pattern (SADP) [32, 33]. DSC tests were conducted on as-cast Alloys 1–5, and the results are shown in Fig. 3.6c. The endothermal peaks D1 and D2 around 130 °C and 200 °C correspond to the dissolution of the GP zone and η', respectively [32, 34]. It is apparent that the GP zone and η′ precipitates were formed even under the as-cast condition, which is most likely attributed to the decomposition of highly supersaturated fcc-Al during the cooling process after solidification. As mentioned above, owing to the effect of sluggish diffusion of the entropy alloys, the supersaturated fcc-Al solution contained much more solute atoms than conventional Al alloys, which favors the precipitation of η'. The GP zone and fine η' precipitates in as-cast alloys are reported to be the most effective hardening precipitates [32].

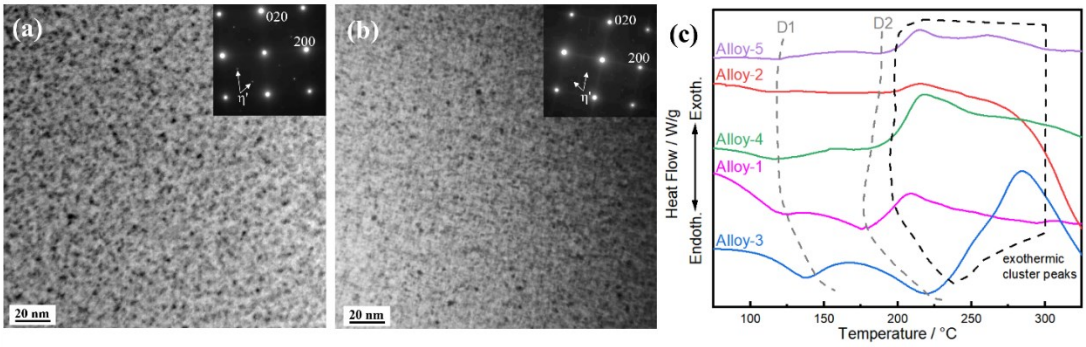

Fig. 3.6 Bright-field TEM images showing η′ precipitates in fcc-Al along <001>$_{Al}$: (a) as-cast Alloy 1, (b) as-cast Alloy 3, and (c) DSC curves of as-cast Alloys 1–5.

The TEM images of Alloys 1 and 3 after 300 °C/5 h and 300 °C/100 h thermal exposures are shown in Fig. 3.7. After 5 h of exposure (Fig. 3.7a and c), the nanoscale GP zones and η' precipitates disappeared, while coarse and submicron particles with different morphologies (typical round, rod, needle/disc, and square shapes) appeared, which were determined to be η-$MgZn_2$, S-Al_2CuMg, θ-Al_2Cu, and σ-$Al_5Cu_6Mg_2$ phases, respectively, based on their morphology and chemical composition analyzed by TEM–EDS [35]. During the initial thermal exposure, the dissolution of the GP zone and η' occurred at 130–200 °C (D1 and D2 peaks in Fig. 3.6c), which was followed by a few exothermic peaks indicating the formation of new types of precipitates. Because of the highly supersaturated fcc-Al with Zn, Mg, and Cu solutes in these entropy alloys, the exact mechanism of the phase transformation at 300 °C is not yet well understood. It seems that during thermal exposure at 300 °C, the GP zones and part of the η' were dissolved into the matrix, and the enriched solutes formed other types of precipitates (S-Al_2CuMg, θ-Al_2Cu, and σ-$Al_5Cu_6Mg_2$), while a part of the η' precipitates may have been directly transformed into equilibrium η particles. After 5 h of thermal exposure, the nanoscale GP zones and η' precipitates were replaced by coarse equilibrium particles, resulting in a significant decrease in the strengthening effect of fcc-Al. The higher the fraction of fcc-Al in the alloy, the larger the reduction in strength was (Fig. 3.5c). For instance, the YS reduction of Alloy 5 with 34 vol.% fcc-Al was limited to 6%, while the YS reduction of Alloys 1 and 3 with more than 80 vol.% fcc-Al reached 30%–35%. After prolonged exposure for 100 h, the coarse particles continued to be

slowly coarsened (Figs. 3.7b and d), but the decline in strengthening was no longer obvious, as shown in Fig. 3.5a.

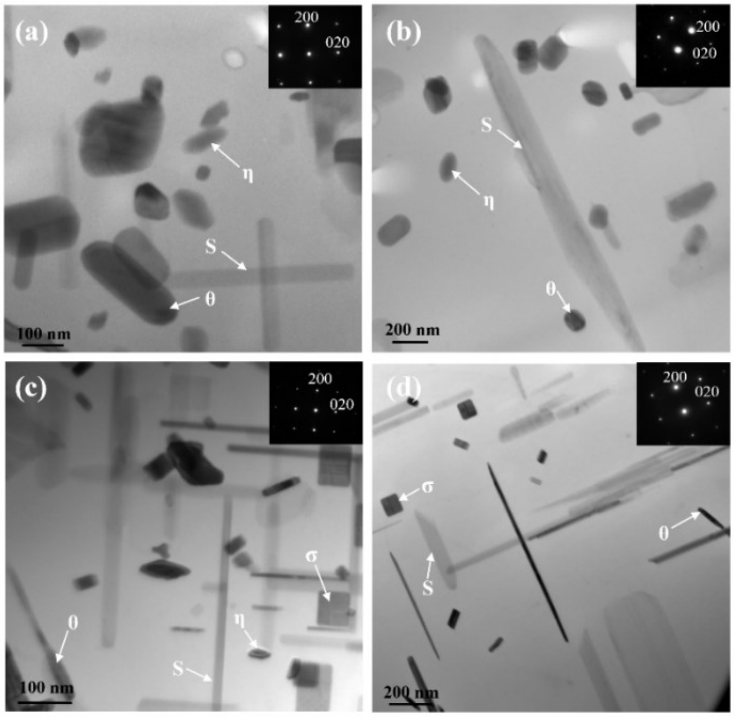

Fig. 3.7 Bright-field TEM images of fcc-Al in (a, b) Alloy 1, (c, d) Alloy 3, (a, c) after thermal exposure for 5 h and (b, d) after thermal exposure for 100 h at 300 °C.

The phase evolution after the 300 °C/100 h exposure in all Alloys 1–5 was examined by XRD and SEM. Typical results for Alloys 1, 2, and 5 are shown in Fig. 3.8. In the fcc-Al phase, some bright particles precipitated out, as indicated by the white arrows. According to Fig. 3.7, these particles were the various coarse precipitates (η, S, θ, σ) generated during thermal exposure. It was found that the type and ratio of the main phases in Alloys 1 and 3–5 generally remained the same as those before thermal exposure, whereas a new phase, Al_2CuMg, uniquely appeared in Alloy 2. The newly formed Al_2CuMg phase coexisted with the $MgZn_2$ phase, seemingly replacing some of the $MgZn_2$ as part of the eutectic microstructure, as shown in Fig. 3.8e. According to

the quantitative results from the OM images, in as-cast Alloy 2, the volume fractions of the three phases, fcc-Al, Al_2Cu, and $MgZn_2$, were 52.96%, 18.35%, and 28.69%, respectively (Table 3.2). After 300 °C/100 h exposure, Alloy 2 contained fcc-Al, Al_2Cu, $MgZn_2$, and Al_2CuMg with volume fractions of 51.71%, 19.17%, 23.75%, and 5.38%, respectively. Therefore, it can be inferred that the new Al_2CuMg phase in Alloy 2 was transformed from $MgZn_2$. This phase transformation was observed only in Alloy 2.

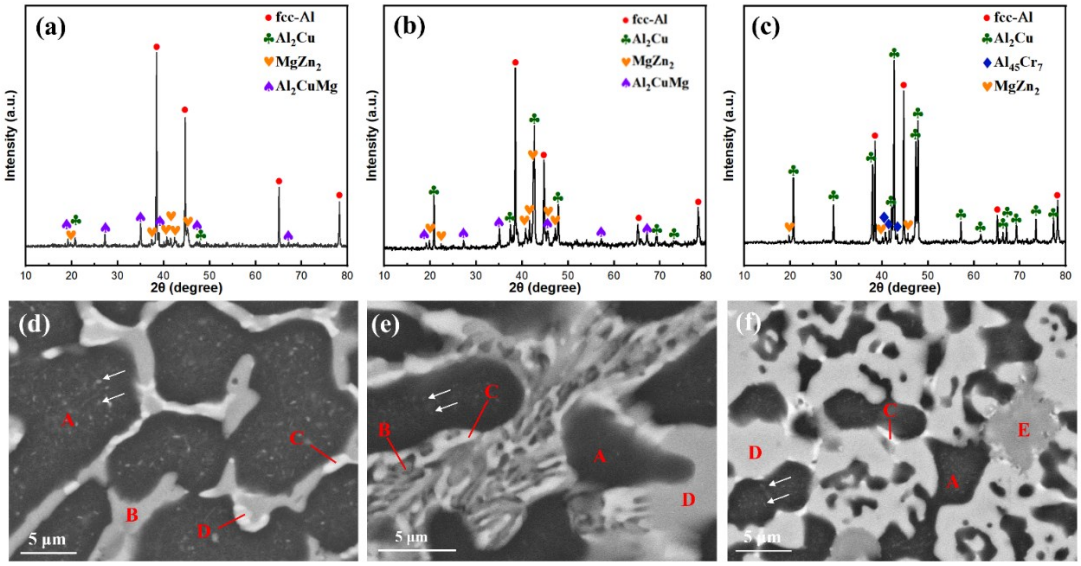

Fig. 3.8 XRD patterns and SEM backscattered electron images after 300 °C/100 h exposure: (a, d) Alloy 1, (b, e) Alloy 2, and (c, f) Alloy 5.

Because Alloys 1 and 3–5 contained the same ICs before and after thermal exposure, the contribution of ICs to the strength remained the same; consequently, their strength reduction after thermal exposure (Fig. 3.5c) was caused by the precipitate transformation in fcc-Al (Fig. 3.7). In Alloy 2, however, apart from the change in fcc-Al, a phase transformation from $MgZn_2$ to Al_2CuMg occurred. From Table 3.3, Al_2CuMg exhibits a much higher microhardness than $MgZn_2$ at both room temperature

and 300 °C. Therefore, after thermal exposure, although the precipitate transformation in fcc-Al decreased the strength, the phase transformation from $MgZn_2$ to Al_2CuMg compensated for the decrease in strength to some extent, leading to a below-average strength reduction in Alloy 2 (Fig. 3.5c).

3.3.4 Role of the IC network on strengthening

The elevated-temperature YS of Alloys 1–5 as a function of the IC content is plotted in Fig. 3.9. It can be seen that the YS of all five alloys is closely related to the content of ICs. The YS at elevated-temperature generally increased with increasing IC content. After the 300 °C/100 h exposure, when the contribution of fcc-Al became weaker due to softening and precipitate coarsening, the ICs and their network were the predominant components contributing to the alloy strength during plastic deformation. In this study, Alloy 5 showed the best mechanical properties, which benefited from its highest IC content and lamellar eutectic morphology. To better understand the role of ICs, in addition to the 2D morphologies of ICs shown in Fig. 3.2, the 3D morphology and spatial distribution of ICs in as-cast Alloys 4 and 5 were studied.

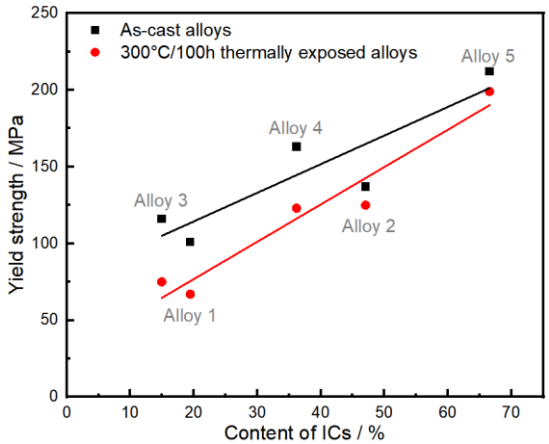

Fig. 3.9 Yield strengths of Alloys 1–5 at 300 °C as a function of the content of ICs.

Figs. 3.10 and 3.11 show the 3D reconstructions of Alloys 4 and 5, respectively, with a reconstructed volume of 30 × 30 × 15 μm^3; images from slightly different perspectives are shown to better present the morphology and distribution features. Figs. 3.10a and 3.11a display the spatial distribution of all phases in Alloys 4 and 5, respectively. The purple bulk represents the fcc-Al phase, the yellow skeleton represents Al_2Cu, and the blue block represents $Al_{45}Cr_7$. The trace amounts of $MgZn_2$ in both alloys (Table 3.2) were reconstructed together with Al_2Cu. The volume fraction of each phase obtained from the spatial structure was similar to that listed in Table 3.2, confirming the reliability of the 3D results. The Al_2Cu skeleton is extracted and shown in Figs. 3.10b and 3.11b. The Al_2Cu skeleton in both alloys had an interconnectivity of nearly 100%, as measured using the method described in [36]. It was reported that higher interconnectivity enables the hard IC network to carry more load from the matrix, resulting in higher strength [37]. At the same time, it can impose a lower limit on the ductility of alloys [38]. Although the Al_2Cu intermetallics in both Alloys 4 and 5 had an uninterrupted structure, the difference in the volume fraction and morphology of Al_2Cu between the two alloys was marked. The Al_2Cu in Alloy 5 (Fig. 3.11b) has a higher mass and is more robust, which can provide stronger support than the relatively thin structure in Alloy 4 (Fig. 3.10b). Moreover, the Al_2Cu in Alloy 5 had a higher extent of lamellar eutectic structure than that in Alloy 4. It has been reported that the morphology of the eutectic phase has a substantial impact on the YS, and the lamellar eutectic Al_2Cu in Alloy 5 was stiffer than the divorced eutectic Al_2Cu in Alloy 4 [39]. As shown in Figs. 3.10c and 3.11c, the $Al_{45}Cr_7$ blocks were generally relatively sharp, and thus they may be prone to cause stress concentration and initiate cracks at room

temperature, as reported in our previous study [21]. However, $Al_{45}Cr_7$ is very heat-resistant at high temperatures. At the same time, the $Al_{45}Cr_7$ particles were well connected to Al_2Cu, as shown in Figs. 3.10d and 3.11d. The hard and heat-resistant Al_2Cu and $Al_{45}Cr_7$ together formed a well-interconnected IC network in the alloys, which plays a vital role in strengthening at elevated temperatures. From the 3D reconstruction, it is apparent that Alloy 5 with a high IC content and lamellar eutectic structure possessed a solid and strong IC network that greatly contributed to its high strength.

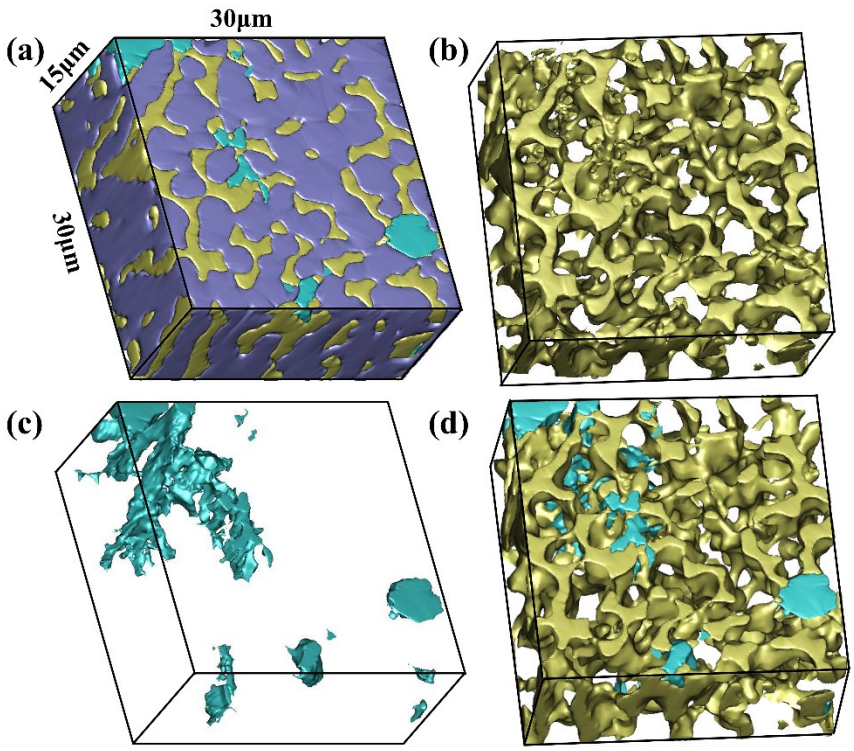

Fig. 3.10 3D phase distribution in as-cast Alloy 4: (a) all phases, (b) Al_2Cu phase, (c) $Al_{45}Cr_7$ phase, and (d) integrated IC network.

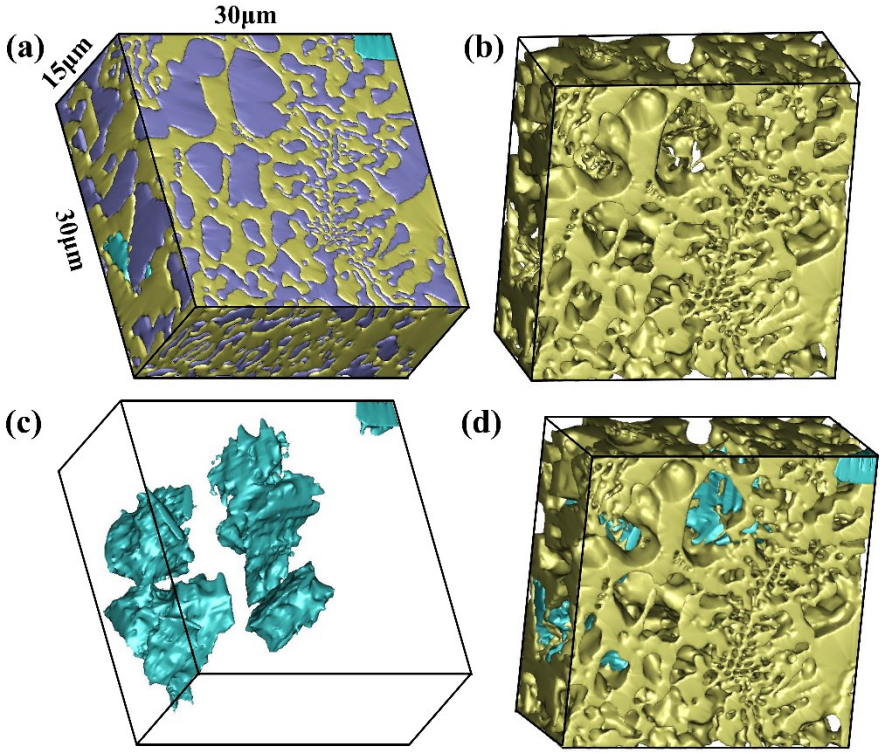

Fig. 3.11 3D phase distribution in as-cast Alloy 5: (a) all phases, (b) Al_2Cu phase, (c) $Al_{45}Cr_7$ phase, and (d) integrated IC network.

3.3.5 Comparison of the strength and density data for various aluminum alloys

The need to develop new materials with outstanding strength, microstructure stability, and lightweight characteristics is of prime interest in the automotive and aerospace industries. In recent years, significant efforts have been devoted to improving the elevated-temperature mechanical properties of both entropy and conventional alloys of aluminum [21, 35, 40, 41]. Fig. 3.12 summarizes the YS at room/elevated temperatures and the alloy density for various aluminum alloys, including Al-based entropy alloys and conventional Al alloys with a density of below 4.0 g/cm^3. The latter alloys listed here are those involving one main element with additional minor elements guided by the conventional alloy design strategy, and have

been recent developed in lab to improve the elevated-temperature strength through microalloying and optimized heat treatments as the heat-resistant alloys. In terms of the room-temperature strength (Fig. 3.12a), the Al-based entropy alloys have more dispersed data points than conventional Al alloys. The conventional Al alloys generally have a low density of ~2.75 g/cm^3, whereas the density of most Al-based entropy alloys is higher than this value. The YS of conventional Al alloys varies over a wide range, but some exhibit high YS values of close to 400 MPa owing to strong precipitation strengthening. The YS of some Al-based entropy alloys is much higher than that of conventional Al alloys; however, the mechanical properties of the former are not always superior because the strengthening is mainly a result of ICs rather than precipitation. The data points from the same study exhibit a near-linear relationship between the YS and density owing to the similar IC types among the alloys. The five experimental as-cast alloys in this study show decent positions in Fig. 3.12a, especially Alloy 5 with a YS of up to 588 MPa and density of 3.63 g/cm^3.

Fig. 3.12b displays the YS at 300 °C for various aluminum alloys without thermal exposure. Owing to the limited number of studies at elevated temperatures, fewer data points on Al-based alloys are listed. Because of the short time at the elevated test temperatures, precipitation still plays a considerable role in strengthening conventional alloys; thus, the YS values of some conventional Al alloys are still relatively high (150–200 MPa). Although some Al-based entropy alloys, including Alloy 5 in this study, have an excellent YS of over 200 MPa, the large advantage of Al-based entropy alloys is not obvious under this condition.

Fig. 3.12c shows the YS at 300 °C after thermal exposure at 300 °C for 100 h. The superiority of Al-based entropy alloys for structural applications at high temperatures is not only due to their high mechanical strength but also their strength retention and thermal stability at elevated temperatures. Owing to the rapid coarsening of precipitates, most conventional Al alloys exhibit a large reduction in YS after long thermal exposure. Al-based entropy alloys, by introducing a high proportion of thermally stable ICs, retain good mechanical strength after thermal exposure. Alloy 5 contained ICs with a volume fraction of 67% and retained outstanding strength, with a YS of 199 MPa and a maximum compressive strength of 234 MPa. Compared with the conventional Al alloys, with a density increase of less than 30%, the experimental Alloy 5 after thermal exposure had a strength increment of more than 40%, indicating the higher specific strength of the material. Similar examples can be found in our previous study, and are shown as black squares in Fig. 3.12 [21]. Owing to its excellent mechanical performance at 300 °C after long thermal exposure, the Al-based entropy Alloy 5 can provide a larger advantage and greater potential for elevated-temperature applications relative to conventional Al alloys.

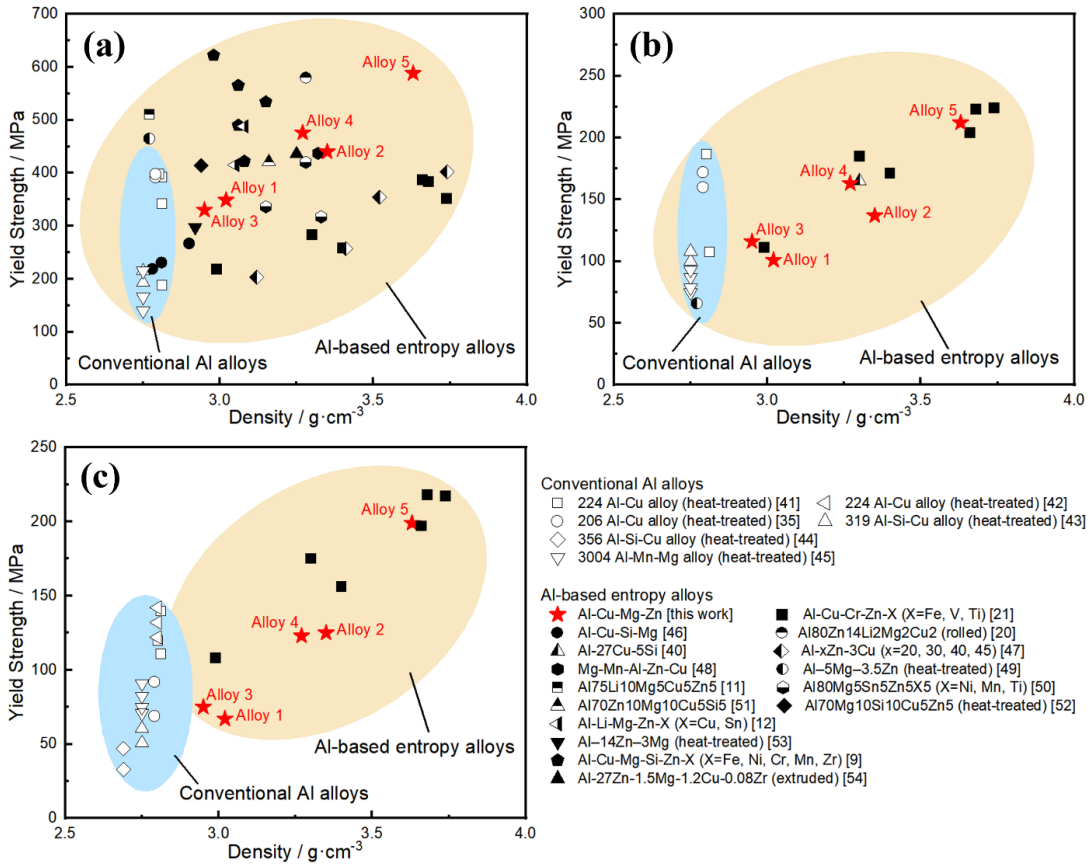

Note: For the density not mentioned in some references, it is calculated through mixing density equation [21].

Fig. 3.12 Comparison of the YS and density of Al-based entropy alloys and conventional Al alloys at (a) room temperature, (b) 300 °C, and (c) 300 °C after thermal exposure for 100 h.

In this study, five Al–Cu–Mg–Zn experimental alloys were designed to significantly increase the chemical composition space of aluminum alloys and explore their exceptional mechanical properties at high temperatures. The alloys were fabricated through conventional melting and casting, which are accessible to the conventional fabrication routes and cost effective. The ratio of the elements added was adjusted to obtain a higher entropy, which facilitated simple phase formation while maintaining a low alloy density. According to the criteria of Yeh et al. and Sanchez et al. [8, 9], entropy alloys can be divided into high-entropy, medium-entropy, and low-

entropy alloys for entropy values of greater than 1.5R, between 1R and 1.5R, and less than 1R (where R is the gas constant), respectively. According to the mixing entropy equation [5], the five experimental alloys in this study have entropy values varying from 2.88 to 7.11 J/mol/K (0.3R to 0.9R), falling in the low-entropy alloy category. However, their entropy values are still much higher than those of conventional Al alloys (~1 J/mol/K and ~0.1R). Most Al-based entropy alloys reported in the literature (sometimes called multicomponent alloys) [9, 11-14, 21] have entropy values between 0.3R and 1.2R, falling in the medium-entropy and low-entropy categories. Because of the large chemical difference and high negative enthalpy between aluminum and the alloying elements, the presence of a large quantity of intermetallic compounds (ICs) is inevitable in Al-based entropy alloys [12, 27]. This limits the plasticity at room temperature but can significantly improve the high-temperature mechanical properties if the proper type and proportion of ICs are selected. Among the five experimental alloys studied, Alloy 5 achieved the highest mechanical performance and thermal stability at 300 °C, providing a promising potential for elevated-temperature applications.

3.4 Conclusions

1) Five Al–Cu–Mg–Zn entropy alloys were designed and investigated in this study. All five experimental alloys exhibited lightweight characteristics with density values ranging from 2.95 to 3.63 g/cm^3 and revealed multiphase features. A large quantity of intermetallic compounds (ICs) appeared in the as-cast microstructures. With increasing Cu and other element contents, the volume fraction of ICs increased.

2) The as-cast Alloys 1–5 exhibited excellent compressive strength at room temperature, with YS ranging from 330 to 588 MPa. Alloy 5 ($Al_{77}Cu_{17}Zn_3Mg_2Cr_1$) had the highest YS of 588 MPa; however, its plasticity was low (0.72%) because of the high volume fraction of ICs.

3) At 300 °C, all alloys retained considerably high strength, with YS values of greater than 100 MPa. Thus, the plasticity of the alloys was significantly improved. Alloy 5 exhibited the highest YS of 212 MPa and maximum compressive strength of 257 MPa.

4) The GP zones and fine η' precipitates were effective strengthening sources for fcc-Al in the as-cast alloys. During thermal exposure, they were transformed into coarse and submicron particles, which deteriorated the mechanical behavior to varying degrees. After thermal exposure at 300 °C for 100 h, the strength of Alloy 5 at 300 °C slightly decreased (by less than 10%), and it still retained the highest strength among the five alloys studied, with a YS of 199 MPa and a maximum compressive strength of 234 MPa.

5) The main source of the strengthening of this entropy alloy series came from the IC network. From the 3D reconstruction, Alloy 5, with a high IC content and lamellar eutectic structure, possessed a solid and strong IC network that greatly contributed to its high strength. Combining its high strength and good thermal stability at 300 °C, the novel lightweight entropy Alloy 5 exhibits promising potential for elevated-temperature applications.

References

[1] I. J. Polmear, M. J. Couper, Design and development of an experimental wrought aluminum alloy for use at elevated temperatures, Metall. Trans. A 19 (1988) 1027-1035. https://doi.org/10.1007/BF02628387

[2] M. Asadikiya, S. Yang, Y. Zhang, C. Lemay, D. Apelian, Y. Zhong, A review of the design of high-entropy aluminum alloys: a pathway for novel Al alloys, J. Mater. Sci. 56(21) (2021) 12093-12110. https://doi.org/10.1007/s10853-021-06042-6

[3] J.W. Yeh, S.K. Chen, S.J. Lin, J.Y. Gan, T.S. Chin, T.T. Shun, C.H. Tsau, S.Y. Chang, Nanostructured high-entropy alloys with multiple principal elements: novel alloy design concepts and outcomes, Adv. Eng. Mater. 6(5) (2004) 299-303. https://doi.org/10.1002/adem.200300567

[4] B. Cantor, I.T.H. Chang, P. Knight, A.J.B. Vincent, Microstructural development in equiatomic multicomponent alloys, Mater. Sci. Eng. A 375 (2004) 213-218. https://doi.org/10.1016/j.msea.2003.10.257

[5] Y. Zhang, T.T. Zuo, Z. Tang, M.C. Gao, K.A. Dahmen, P.K. Liaw, Z.P. Lu, Microstructures and properties of high-entropy alloys, Progress in materials science 61 (2014) 1-93. https://doi.org/10.1016/j.pmatsci.2013.10.001

[6] S. Praveen, H.S. Kim, High-entropy alloys: potential candidates for high-temperature applications–an overview, Advanced Engineering Materials 20(1) (2018) 1700645. https://doi.org/10.1002/adem.201700645

[7] D.B. Miracle, O.N. Senkov, A critical review of high entropy alloys and related concepts, Acta Mater. 122 (2017) 448-511. https://doi.org/10.1016/j.actamat.2016.08.081

[8] J.W. Yeh, Alloy design strategies and future trends in high-entropy alloys, JOM 65(12) (2013) 1759-1771. https://doi.org/10.1007/s11837-013-0761-6

[9] J.M. Sanchez, I. Vicario, J. Albizuri, T. Guraya, E.M. Acuña, Design, microstructure and mechanical properties of cast medium entropy aluminium alloys, Sci. Rep. 9(1) (2019) 1-12. https://doi.org/10.1038/s41598-019-43329-w

[10] Y.E.H. Jien-Wei, Recent progress in high entropy alloys, Ann. Chim. Sci. Mat. 31 (6) (2006) 633–648. https://doi.org/10.3166/acsm.31.633-648

[11] K.S. Tun, P. Murugan, T.S. Srivatsan, M. Gupta, Synthesis and characterization of aluminium based multicomponent alloys, Mater. Today 46 (2021) 1210–1214. https://doi.org/10.1016/j.matpr.2021.02.066

[12] X. Yang, S.Y. Chen, J.D. Cotton, Y. Zhang, Phase stability of low-density, multiprincipal component alloys containing aluminum, magnesium, and lithium, JOM 66 (10) (2014) 2009–2020. https://doi.org/10.1007/s11837-014-1059-z

[13] L. Shao, T. Zhang, L. Li, Y. Zhao, J. Huang, P.K. Liaw, Y. Zhang, A low-cost lightweight entropic alloy with high strength, J. Mater. Eng. Perform. 27 (12) (2018) 6648–6656. https://doi.org/10.1007/s11665-018-3720-0

[14] R. Li, X. Li, J. Ma, Y. Zhang, Sub-grain formation in Al–Li–Mg–Zn–Cu lightweight entropic alloy by ultrasonic hammering, Intermetallics 121 (2020) 106780. https://doi.org/10.1016/j.intermet.2020.106780

[15] C. Liu, A. Garner, H. Zhao, P.B. Prangnell, B. Gault, D. Raabe, P. Shanthraj, CALPHAD-informed phase-field modeling of grain boundary microchemistry and precipitation in Al-Zn-Mg-Cu alloys, Acta Mater. 214 (2021) 116966. https://doi.org/10.1016/j.actamat.2021.116966

[16] G.E. Totten, D.S. MacKenzie, Handbook of Aluminum: Vol. 1: Physical Metallurgy

and Processes, CRC Press, 2003. https://doi.org/10.1201/9780203912591

[17] T.Y. Ahn, J.G. Jung, E.J. Baek, S.S. Hwang, K. Euh, Temporal evolution of precipitates in multicomponent Al–6Mg–9Si–10Cu–10Zn–3Ni alloy studied by complementary experimental methods, J. Alloys Compd. 701 (2017) 660-668. https://doi.org/10.1016/j.jallcom.2017.01.183

[18] T.Y. Ahn, J.G. Jung, E.J. Baek, S.S. Hwang, K. Euh, Temperature dependence of precipitation behavior of Al–6Mg–9Si–10Cu–10Zn–3Ni natural composite and its impact on mechanical properties, Mater. Sci. Eng. A 695 (2017) 45-54. https://doi.org/10.1016/j.msea.2017.04.015

[19] E.J. Baek, T.Y. Ahn, J.G. Jung, J.M. Lee, Y.R. Cho, K. Euh, Effects of ultrasonic melt treatment and solution treatment on the microstructure and mechanical properties of low-density multicomponent Al70Mg10Si10Cu5Zn5 alloy, J. Alloy. Compd. 696 (2017) 450–459. https://doi.org/10.1016/j.jallcom.2016.11.305

[20] R. Li, Z. Ren, Y. Wu, Z. He, P.K. Liaw, J. Ren, Y. Zhang, Mechanical behaviors and precipitation transformation of the lightweight high-Zn-content Al–Zn–Li–Mg–Cu alloy, Mater. Sci. Eng. A 802 (2021) 140637. https://doi.org/10.1016/j.msea.2020.140637

[21] L. Cui, Z. Zhang, X.G. Chen, Development of lightweight Al-based entropy alloys for elevated temperature applications, J. Alloys Compd. 938 (2023) 168619. https://doi.org/10.1016/j.jallcom.2022.168619

[22] C.M. Dinnis, A.K. Dahle, J.A. Taylor, Three-dimensional analysis of eutectic grains in hypoeutectic Al–Si alloys. Mater. Sci. Eng. A 392(1-2) (2005) 440-448. https://doi.org/10.1016/j.msea.2004.10.037

[23] N. Chawla, R.S. Sidhu, V.V. Ganesh, Three-dimensional visualization and microstructure-based modeling of deformation in particle-reinforced composites, Acta Mater. 54(6) (2006) 1541-1548. https://doi.org/10.1016/j.actamat.2005.11.027

[24] J.J. Williams, K.E. Yazzie, E. Padilla, N. Chawla, X. Xiao, F. De Carlo, Understanding fatigue crack growth in aluminum alloys by in situ X-ray synchrotron tomography, Int. J. Fatigue 57 (2013) 79-85. https://doi.org/10.1016/j.ijfatigue.2012.06.009

[25] S. Cui, I.H. Jung, Thermodynamic modeling of the quaternary Al-Cu-Mg-Si system, Calphad 57 (2017) 1-27. https://doi.org/10.1016/j.calphad.2017.02.002

[26] S.L. Chen, Y. Zuo, H.Y. Liang, Y.A. Chang, A thermodynamic description for the ternary Al-Mg-Cu system, Metall. Mater. Trans. A 28(2) (1997) 435-446. https://doi.org/10.1007/s11661-997-0144-0

[27] C. Ji, A. Ma, J. Jiang, Mechanical properties and corrosion behavior of novel Al-Mg-Zn-Cu-Si lightweight high entropy alloys, J. Alloy. Compd. 900 (2022) 163508. https://doi.org/10.1016/j.jallcom.2021.163508.

[28] J.M. Sanchez, I. Vicario, J. Albizuri, T. Guraya, J.C. Garcia, Phase prediction, microstructure and high hardness of novel light-weight high entropy alloys, J. Mater. Res. Technol. 8 (1) (2019) 795–803. https://doi.org/10.1016/j.jmrt.2018.06.010

[29] M.V. Glazoff, A. Khvan, V.S. Zolotorevsky, N.A. Belov, A. Dinsdale, Casting aluminum alloys: their physical and mechanical metallurgy, second ed., Butterworth-Heinemann. https://doi.org/10.1016/C2015-0-02446-7

[30] M. Krystýnová, P. Doležal, S. Fintová, J. Zapletal, T. Marada, J. Wasserbauer, Characterization of Brittle Phase in Magnesium Based Materials Prepared by Powder Metallurgy, Key Eng. Mater. 784 (2018) 61-66. https://doi.org/10.4028/www.scientific.net/KEM.784.61

[31] T.H. Müllerr, P. Paufler, Yield strength of the monocrystalline intermetallic compound MgZn2, physica status solidi (a) 40(2) (1977) 471-477. https://doi.org/10.1002/pssa.2210400213

[32] F. Jiang, H.S. Zurob, G.R. Purdy, H. Zhang, Characterizing precipitate evolution of an Al–Zn–Mg–Cu-based commercial alloy during artificial aging and non-isothermal heat treatments by in situ electrical resistivity monitoring, Mater. Charact. 117 (2016) 47-56. https://doi.org/10.1016/j.matchar.2016.04.014

[33] J. Zhu, B. Jiang, D. Yi, H. Wang, G. Wu, Precipitate behavior, mechanical properties and corrosion behavior of an Al-Zn-Mg-Cu Alloy during non-isothermal creep aging with axial tension stress, Metals 10(3) (2020) 378. https://doi.org/10.3390/met10030378

[34] Y. Zhao, J. Liu, T.D. Topping, E.J. Lavernia, Precipitation and aging phenomena in an ultrafine grained Al-Zn alloy by severe plastic deformation, J. Alloys Compd. 851 (2021) 156931. https://doi.org/10.1016/j.jallcom.2020.156931

[35] J. Rakhmonov, K. Liu, X.G. Chen, Effects of compositional variation on the thermal stability of θ ′-Al2Cu precipitates and elevated-temperature strengths in Al-Cu

206 alloys, J. Mater. Eng. Perform. 29 (11) (2020) 7221–7230. https://doi.org/10.1007/s11665-020-05227-5

[36] D. Tolnai, G. Requena, P. Cloetens, J. Lendvai, H.P. Degischer, Effect of solution heat treatment on the internal architecture and compressive strength of an AlMg4.7Si8 alloy, Mater. Sci. Eng. A 585 (2013) 480-487. https://doi.org/10.1016/j.msea.2013.06.033

[37] D. Amberger, P. Eisenlohr, M. Göken, On the importance of a connected hard-phase skeleton for the creep resistance of Mg alloys, Acta Mater. 60(5) (2012) 2277-2289. https://doi.org/10.1016/j.actamat.2012.01.017

[38] B. Zhang, S. Gavras, A.V. Nagasekhar, C.H. Cáceres, M.A. Easton, The strength of the spatially interconnected eutectic network in HPDC Mg-La, Mg-Nd, and Mg-La-Nd alloys, Metall. Mater. Trans. A 45(10) (2014) 4386-4397. https://doi.org/10.1007/s11661-014-2416-9

[39] N.T.B.N. Koundinya, R.S. Kottada, Distinct role of eutectic morphology on the plastic flow in cast Mg–3Ca alloy, Mater. Sci. Eng. A 791 (2020) 139633. https://doi.org/10.1016/j.msea.2020.139633

[40] S.A. Awe, Elevated temperature tensile properties of a ternary eutectic Al–27%Cu–5% Si cast alloy, Int. J. Lightweight Mater. 4(1) (2021) 18-26. https://doi.org/10.1016/j.ijlmm.2020.07.004

[41] J. Rakhmonov, K. Liu, L. Pan, F. Breton, X.G. Chen, Enhanced mechanical properties of high-temperature-resistant Al–Cu cast alloy by microalloying with Mg, J. Alloy. Compd. 827 (2020) 154305. https://doi.org/10.1016/j.jallcom.2020. 154305

[42] P. Hu, K. Liu, L. Pan, X.G. Chen, Effect of Mg microalloying on elevated-temperature creep resistance of Al–Cu 224 cast alloys, Mater. Sci. Eng. A 851 (2022) 143649. https://doi.org/10.1016/j.msea.2022.143649

[43] L. Jin, K. Liu, X.G. Chen, Evolution of dispersoids and their effects on elevated-temperature strength and creep resistance in Al-Si-Cu 319 cast alloys with Mn and Mo additions, Mater. Sci. Eng. A 770 (2020) 138554. https://doi.org/10.1016/j.msea.2019.138554

[44] A.R. Farkoosh, X.G. Chen, M. Pekguleryuz, Dispersoid strengthening of a high temperature Al–Si–Cu–Mg alloy via Mo addition, Mater. Sci. Eng. A 620 (2015) 181–189 https://doi.org/10.1016/j.msea.2014.10.004

[45] K. Ma, E.M. Elgallad, Z.X. Chen, B.L. Xiao, X.G. Chen, Improving the elevated-temperature mechanical properties of AA3004 hot-rolled sheets by microalloying with Mo and optimizing the process route, J. Mater. Res. Technol. 19 (2022) 4489–4503. https://doi.org/10.1016/j.jmrt.2022.06.171

[46] Q. Cai, C.L. Mendis, I.T. Chang, Z. Fan, Microstructure and mechanical properties of new die-cast quaternary Al-Cu-Si-Mg alloys, Mater. Sci. Eng. A 800 (2021) 140357. https://doi.org/10.1016/j.msea.2020.140357

[47] S.S. Shin, K.M. Lim, I.M. Park, Effects of high Zn content on the microstructure and mechanical properties of Al–Zn–Cu gravity-cast alloys, Mater. Sci. Eng. A 679 (2017) 340-349. https://doi.org/10.1016/j.msea.2016.09.022

[48] R. Li, J. Gao, K. Fan, Study to microstructure and mechanical properties of Mg containing high entropy alloys, Mater. Sci. Forum, Trans. Tech. Publ. Ltd 650 (2010) 265–271. https://doi.org/10.4028/www.scientific.net/MSF.650.265

[49] N. Takata, M. Ishihara, A. Suzuki, M. Kobashi, Microstructure and strength of a novel heat-resistant aluminum alloy strengthened by T-Al6Mg11Zn11 phase at elevated temperatures, Mater. Sci. Eng. A 739 (2019) 62-70. https://doi.org/10.1016/j.msea.2018.10.034

[50] J.M. Sanchez, A. Pascual, I. Vicario, J. Albizuri, T. Guraya, H. Galarraga, Microstructure and Phase Formation of Novel Al80Mg5Sn5Zn5X5 Light-Weight Complex Concentrated Aluminum Alloys, Metals 11(12) (2021) 1944. https://doi.org/10.3390/met11121944

[51] Y. Huang, J. Wen, Y. Liu, Y. Zhao, Effects of electromagnetic frequency on the microstructure and mechanical properties of Al70Zn10Mg10Cu5Si5 medium entropy alloy, J. Mater. Res. Technol. 17 (2022) 3105-3117. https://doi.org/10.1016/j.jmrt.2022.02.034

[52] K. Euh, K., J.G. Jung, E.J. Baek, J.M. Lee, H.W. Kim, Effect of heat-treatment on microstructure and mechanical properties of sonicated multicomponent AlMgSiCuZn alloy, Light Metals (2017) 379-383. Springer, Cham. https://doi.org/10.1007/978-3-319-51541-0_47

[53] A.P. Babu, A. Huang, N. Birbilis, On the heat treatment and mechanical properties of a high solute Al–Zn–Mg alloy processed through laser powder bed fusion process, Mater. Sci. Eng. A 807 (2021) 140857. https://doi.org/10.1016/j.msea.2021.140857

[54] X. Meng, D. Zhang, W. Zhang, C. Qiu, D. Chen, Achieving high damping capacity and strength simultaneously in a high-zinc aluminum alloy via melt spinning and hot extrusion, Mater. Sci. Eng. A 833 (2022) 142376. https://doi.org/10.1016/j.msea.2021.142376

Chapter 4

Development of lightweight Al-based entropy alloys for elevated temperature applications

(Published in *Journal of Alloys and Compounds*)

Abstract

A series of lightweight Al-based entropy alloys containing Cu, Zn, Cr, V, Ti and Fe has been designed for elevated temperature applications. The microstructure, mechanical properties at room and elevated temperatures, and the thermal stability of six entropy alloys ($Al_{93}Cu_4Zn_1Cr_1Fe_1$, $Al_{85}Cu_{11}Zn_2Cr_1Fe_1$, $Al_{85}Cu_{11}Zn_1Cr_2V_1$, $Al_{78}Cu_{18}Zn_2Cr_1Fe_1$, $Al_{78}Cu_{18}Zn_1Cr_2Ti_1$, and $Al_{78}Cu_{18}Zn_1Cr_2V_1$) were investigated. Owing to the large chemical difference and high negative enthalpy between Al and the alloying elements, the generation of a large quantity of intermetallic compounds (ICs) was inevitable. With increasing Cu content, the volume fraction of ICs increased significantly. The three high-Cu alloys ($Al_{78}Cu_{18}Zn_2Cr_1Fe_1$, $Al_{78}Cu_{18}Zn_1Cr_2Ti_1$, and $Al_{78}Cu_{18}Zn_1Cr_2V_1$) exhibited high yield strengths of more than 200 MPa and excellent thermal stability at 300 °C. These values are considerably superior to those of most conventional aluminum alloys. The strengthening mechanisms at room and elevated temperatures have been discussed. The favorable thermal stability and good mechanical properties of the high-Cu alloys up to 450 °C indicate their significant potential for high temperature applications.

Keywords: Aluminum entropy alloys, Lightweight, Microstructure, Elevated-temperature strengths, Thermal stability.

4.1 Introduction

As lightweight materials, aluminum alloys play a significant role in the aerospace, automotive, and construction industries. Although several aluminum structural alloys meet the high-strength criteria at room temperature (RT), the general low strength of the aluminum alloys at high temperatures (HTs) significantly limits their widespread applications. For example, the elevated temperature strengths of a typical high-strength 7075 aluminum alloy at 200℃ and 300℃ are approximately 30% and 10% of its RT strengths, respectively [1]. Owing to the development of a green economy and industry, to further advance lightweight aluminum alloys for elevated temperature applications, two requirements are essential: (1) enhanced strength at HTs and (2) maintenance of excellent thermal stability during the prolonged HT service [2].

High-entropy alloys (HEAs) are a class of newly emerging materials containing multiple principal elements in equal or near-equal atomic ratios [3-4]. The concept behind this new design is that by mixing several principal elements, resulting alloys a considerably higher mixing entropy than this of the conventional alloys, allowing them to resist the effects of the mixing enthalpy, i.e., the formation of intermetallic compounds (ICs), therefore stabilizing the simple, disordered solid solutions [5-6]. This deviates from the conventional alloy design strategy (involving one main element with additional minor elements), creating a new avenue for designing alloys with promising comprehensive properties, such as high strength, excellent thermal stability, high fatigue, and fracture resistance, which may not be achievable in conventional alloys [6-8]. It is found that the phase formation of HEAs can be simple as a single

solid solution as well as complex as multiple ICs [8-9]. Over the years, the concept of HEAs has expanded and it motivates the development of entropy alloys, including high-entropy, medium-entropy, and low-entropy alloys [9-12]. Developing aluminum entropy alloys can be a novel approach for improving the mechanical properties of aluminum alloys at HTs [2].

Aluminum entropy alloys are Al-based alloys which are intentionally designed by combining with the concept of entropy. They usually have an improved entropy value compared with the traditional aluminum alloys by adding a larger quantity of secondary elements. Therefore, the aluminum entropy alloys are also known as multicomponent aluminum alloys [13-16]. Several Al-based entropy alloys with excellent properties have been reported [5, 11, 13-22]. Sanchez et al. [11] investigated two series Al-based medium-entropy alloys $Al_{65}Cu_5Mg_5Si_{15}Zn_5X_5$ and $Al_{70}Cu_5Mg_5Si_{10}Zn_5X_5$ (wherein, X is Fe, Ni, Cr, Mn or Zr), which exhibited moderate plastic deformation with high compressive strength up to 644 MPa and microhardness up to 264 HV. Yang et al. [15] designed two alloys $Al_{80}Li_5Mg_5Zn_5Cu_5$ and $Al_{80}Li_5Mg_5Zn_5Sn_5$ with a low density of 2.85 g/cm^3 and a high compressive strength of more than 800 MPa with a plasticity up to 17%. Baek et al. [17] investigated the microstructure and compressive mechanical properties of a low-density alloy $Al_{70}Mg_{10}Si_{10}Cu_5Zn_5$ at room and elevated temperatures. The compressive strengths of this alloy were significantly improved (>700 MPa at RT and >110 MPa at 350 °C) compared to those of the conventional cast alloys (A356 and A390) [23]. Owing to the sluggish effect caused by the high concentration of multiple elements, most HEAs generally exhibit poor liquidity and castability, which result in compositional inhomogeneity; consequently, a eutectic

structure is introduced to overcome these issues [14, 24-27]. Shao et al. [14] studied the microstructure and mechanical properties of a series of Al–Mg-based entropy alloys with a low-density range of 2.64–2.75 g/cm^3. They found that the $Al_{85}Mg_{10.5}Zn_{2.025}Cu_{2.025}Si_{0.45}$ alloy with a eutectic structure exhibited excellent compressive strength of more than 800 MPa with a plastic strain of more than 20%. The existing Al-based entropy alloys always contain a large number of elements with low melting points, such as Li, Mg, and Zn; this may deteriorate the mechanical performance of alloys at elevated temperatures. Most previous studies have focused on phase formation and RT mechanical properties. The current literature on the HT mechanical properties and thermal stability of Al-based entropy alloys is very limited.

This study aimed to develop a series of lightweight Al-based entropy alloys with high strength and good thermal stability at elevated temperatures (300 °C and above). To improve the entropy of the system, five elements were added to each alloy; elements with high melting points (Cu, Cr, V, Ti, and Fe) were chosen as candidates to ensure suitable HT mechanical behaviors. As entropic alloys generally have low fluidity during casting, an Al–Cu eutectic structure was adopted owing to its appropriate eutectic point to overcome this issue using a method similar to that reported by Shao et al. [14]. By calculating the empirical thermodynamic parameters commonly adopted for entropy alloy design (discussed in Section 4.4.1 in detail), the type and proportion of elements were adjusted and determined [8, 14, 28]. Wherein, Zn was added for thermodynamic reasons. At the same time, Thermo-Calc simulations were used to predict the phase constitution, and they assisted in the selection of alloys (introduced in Section 4.3.1). Finally, six lightweight Al-based entropy alloys were designed:

$Al_{93}Cu_4Zn_1Cr_1Fe_1$ (Alloy 1), $Al_{85}Cu_{11}Zn_2Cr_1Fe_1$ (Alloy 2), $Al_{85}Cu_{11}Zn_1Cr_2V_1$ (Alloy 3), $Al_{78}Cu_{18}Zn_2Cr_1Fe_1$ (Alloy 4), $Al_{78}Cu_{18}Zn_1Cr_2Ti_1$ (Alloy 5), and $Al_{78}Cu_{18}Zn_1Cr_2V_1$ (Alloy 6). The microstructure, phase formation, phase stability, and mechanical behavior of the experimental alloys at elevated temperatures were investigated, and the relationship between the microstructure and mechanical properties was further examined.

4.2 Experimental procedures

The six alloys were prepared by mixing the corresponding pure elements in a graphite crucible, and each was melted at 880°C in an induction melting furnace under an argon atmosphere. Elements were well mixed through melting and diffusion. Each ingot was remelted at least three times. During remelting, the cast ingot was ground by sandpaper to remove the oxide film and flipped each time in the crucible to improve the homogeneous distribution of the alloying elements. The molten metal was finally cast into a copper permanent mold which was preheated at 250 °C. The produced ingots were then air-cooled down and they had dimensions of about 26x26x50 mm^3. The chemical compositions of the experimental alloys were examined using inductively coupled plasma mass spectrometry, and the results are listed in Table 4.1. Based on the Cu content, the alloys were divided into three groups: low-Cu (Alloy 1), medium-Cu (Alloys 2–3), and high-Cu (Alloys 4–6) alloys.

Table 4.1 Chemical compositions of experimental alloys.

Alloys	Chemical composition, at.%						
	Al	Cu	Zn	Cr	Fe	Ti	V
Alloy 1 ($Al_{93}Cu_4Zn_1Cr_1Fe_1$)	93.18	4.34	0.45	0.99	1.04	-	-
Alloy 2 ($Al_{85}Cu_{11}Zn_2Cr_1Fe_1$)	84.26	12.04	1.88	0.83	0.99	-	-
Alloy 3 ($Al_{85}Cu_{11}Zn_1Cr_2V_1$)	86.26	10.56	0.59	1.72	-	-	0.87
Alloy 4 ($Al_{78}Cu_{18}Zn_2Cr_1Fe_1$)	77.44	19.04	1.72	0.79	1.01	-	-
Alloy 5 ($Al_{78}Cu_{18}Zn_1Cr_2Ti_1$)	78.11	18.68	0.42	1.85	-	0.94	-
Alloy 6 ($Al_{78}Cu_{18}Zn_1Cr_2V_1$)	78.85	18.01	0.47	1.85	-	-	0.82

The microstructures of the alloys were observed using optical microscopy (OM, Nikon Eclipse ME600) and a scanning electron microscopy instrument (SEM, JEOL JSM-6480LV) equipped with an energy-dispersive X-ray spectroscopy (EDS) system. The phases in the alloys were identified via SEM–EDS and X-ray diffraction (XRD, D8 Discover) using Cu Kα radiation with a diffraction angle (2θ) ranging from 10° to 80°, a step size of 0.05°, and a step time of 0.5 s/step. After phase identification, the volume fraction of each phase in each alloy was measured via image analysis using at least five OM images. Transmission electron microscopy (TEM, JEM−2100) with an accelerating voltage of 200 kV was used to examine the distribution of dislocations and precipitates in the experimental alloys. TEM samples were initially cut and punched into rounded pieces with a thickness of 600 μm; they were then mechanically polished to a final thickness of 50–60 μm and electropolished in a twin-jet unit using 20 V at 20℃ in a solution of 30 vol.% nitric acid and 70 vol.% methanol. The differential scanning calorimetry (DSC, PerkinElmer DSC 8000) analyses were conducted on the as-cast samples at a heating rate of 10℃/min under an argon atmosphere. For each alloy, at least two samples were tested to ensure the reproducibility of the obtained results.

Compression tests were conducted at RT and HTs using a Gleeble 3800 thermomechanical simulator unit according to the ASTM E9-09 and ASTM E209-18 standards. Cylindrical specimens with diameter and length of 8 and 12 mm, respectively, were used for the compression tests. The strain rate for the compression tests at RT was set to 10^{-4} s^{-1} owing to the brittleness of certain alloys. For the HT tests, a strain rate of 10^{-3} s^{-1} was used.

4.3 Results

4.3.1 Microstructures and phase constituents

The Thermo-Calc simulations (equilibrium and Scheil's model) were conducted at the alloy design stage to predict phase formation. The equilibrium phase diagrams of the six alloys as a function of temperature were first calculated using the TCAL7 database, and the results are shown in Fig. 4.1. At RT, each alloy was predicted to contain three to four phases. The three major phases were fcc-Al (face centered cubic crystal structure), Al_2Cu, and $Al_{45}Cr_7$; they appeared in each alloy in larger quantities. In Alloy 1 (Fig. 4.1a), the fcc-Al is the dominant phase in the matrix with a mole percentage of 73%. With the increasing content of Cu in the medium-Cu Alloys 2–3 (Fig. 4.1b–c), the fcc-Al remains as the major phase with a reduced percentage of approximately 50%, followed by Al_2Cu as second major phase with a percentage of approximately 30%. In the high-Cu Alloys 4–6 (Fig. 4.1d–f), the major phase is the Al_2Cu phase with approximately 50%, which is followed by the fcc-Al phase with approximately 30%. The $Al_{45}Cr_7$ phase accounted for a large portion of up to approximately 20% of Alloys 3, 5, and 6; this was caused by the high addition amount

of Cr. The Al_3Ti phase was present in Alloy 5 owing to the Ti addition, and Al_7Cu_2Fe existed in Alloys 1, 2, and 4 owing to the Fe addition. The hcp phase was predicted to exist in all six alloys with a low content of less than 3%. According to the database, the hcp phase represented a phase with a hexagonal close-packed (hcp) crystal structure and contained all added elements.

For the comparison, the simulation of the phase formation under the non-equilibrium condition using Scheil's model was also conducted, and the results are displayed in Fig. 4.2. The Scheil's simulation revealed that each alloy contained five to six phases, in which two more minor phases were predicted than that calculated by the equilibrium simulation. In Alloy 1 (Fig. 4.2a), the fcc-Al as the major phase and three minor phases (Al_2Cu, $Al_{45}Cr_7$ and Al_7Cu_2Fe) were predicted, which is consistent with the equilibrium phase diagram (Fig. 4.1a); but two minor phases ($Al_{13}Fe_4$ and Al_5Cr) did not appear in the equilibrium phase diagram. In the medium-Cu Alloys 2–3 (Fig. 4.2b–c), the fcc-Al remained as the major phase and other two minor phases (Al_2Cu and $Al_{45}Cr_7$) also appeared, showing good agreement with the equilibrium simulation (Fig. 4.1b–c). However, other minor phases ($Al_{13}Fe_4$ and Al_5Cr, or Al_3Ti) were not predicted by the equilibrium simulation. In the high-Cu Alloys 4–6 (Fig. 4.2d–f), Al_2Cu became the major phase with approximately 55%, followed by the second major phase fcc-Al with approximately 35%. The results are still similar with those calculated by the equilibrium simulation (Fig. 4.1d–f). The difference is the prediction of some minor phases with small fraction; for instance, $Al_{13}Fe_4$, Al_4Cr and Al_5Cr did not appeare in the equilibrium phase diagram, while $Al_{45}Cr_7$ was not predicted in the Scheil's simulation.

Both simulations showed the multiphase feature in all six experimental alloys, which is very common in the lightweight entropy alloys. This is mainly because of the high electronegativity and strong interatomic interactions among the main light elements, and hence ICs are produced more frequently in the lightweight entropy alloys [5, 14-17]. Even if all the elements are added in near-equal atomic ratios, i.e., the alloy system has a high entropy value, a large quantity of ICs can still be observed [15, 18, 29].

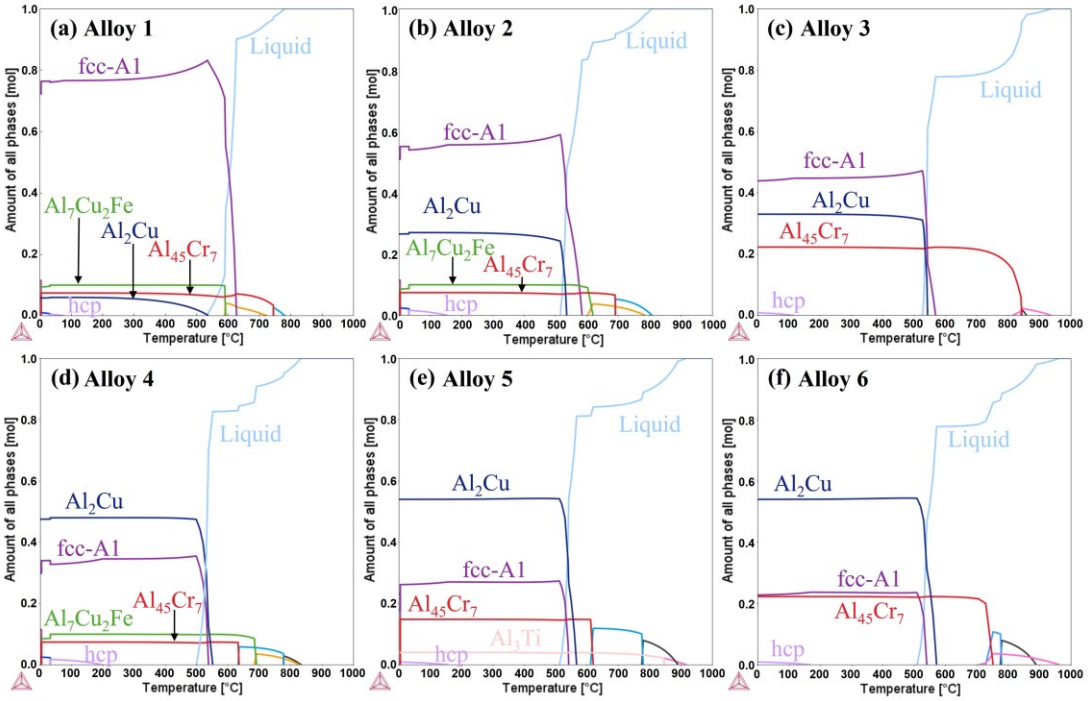

Fig. 4.1 Calculated equilibrium phase diagrams showing the mole fraction of all phases as a function of temperature: (a) Alloy 1, (b) Alloy 2, (c) Alloy 3, (d) Alloy 4, (e) Alloy 5 and (f) Alloy 6.

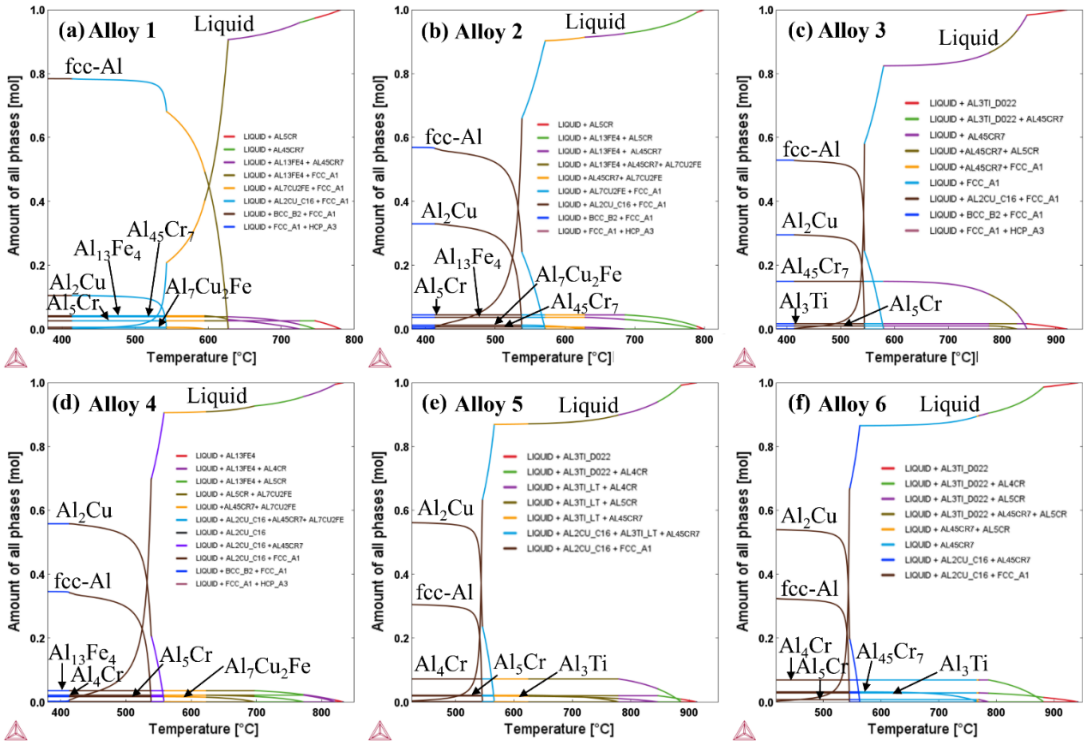

Fig. 4.2 Simulated phase formation using Scheil's model showing the mole fraction of all phases as a function of temperature: (a) Alloy 1, (b) Alloy 2, (c) Alloy 3, (d) Alloy 4, (e) Alloy 5 and (f) Alloy 6.

XRD was used to identify the phase constituents; the corresponding patterns of the as-cast Alloys 1–6 are shown in Fig. 4.3. In most cases, XRD detected three major phases of fcc-Al, Al_2Cu, and $Al_{45}Cr_7$. In Fig. 4.3a–c, the diffraction peaks of fcc-Al are intense, indicating a high fraction of the fcc-Al in these three alloys, which is consistent with the results from the Thermo-Calc simulations. Compared with the standard Al diffraction patterns, peaks of fcc-Al of all alloys slightly shifted to the right with varying degrees, indicating the existence of solute atoms in Al. Compared with Alloy 1 (Fig. 4.3a), the medium-Cu Alloys 2–3 have more intense Al_2Cu diffraction peaks, suggesting an increase in the proportion of Al_2Cu in the alloys. $Al_{45}Cr_7$ was also detected with weak diffraction peaks, indicating its low proportion in the alloy. In the high-Cu alloys (Fig. 4.3d–f), the diffraction peaks of Al_2Cu are more intense than those

of fcc-Al, indicating that Al_2Cu is the predominant phase in the high-Cu Alloys 4–6, which corresponds to the results in Figs. 4.1–4.2. Diffraction peaks of Al_3Ti are observed in Alloy 5 (Fig. 4.3e). Overall, the XRD results are in good agreement with the prediction of main phases from the Thermo-Calc simulations. However, not all the predicted phases in Figs. 4.1–4.2 were observed in XRD results. This can be due to three reasons: (1) the volume fraction of the phase was too small to be detected; (2) the results of Thermo-Calc simulations were not yet accurate enough due to the incomplete of database for Al-base entropy alloys, which are often beyond the Al-rich region; (3) sluggish diffusion effect on the entropy alloys could affect the phase formation, such as enriching the solute atoms in each phase [5].

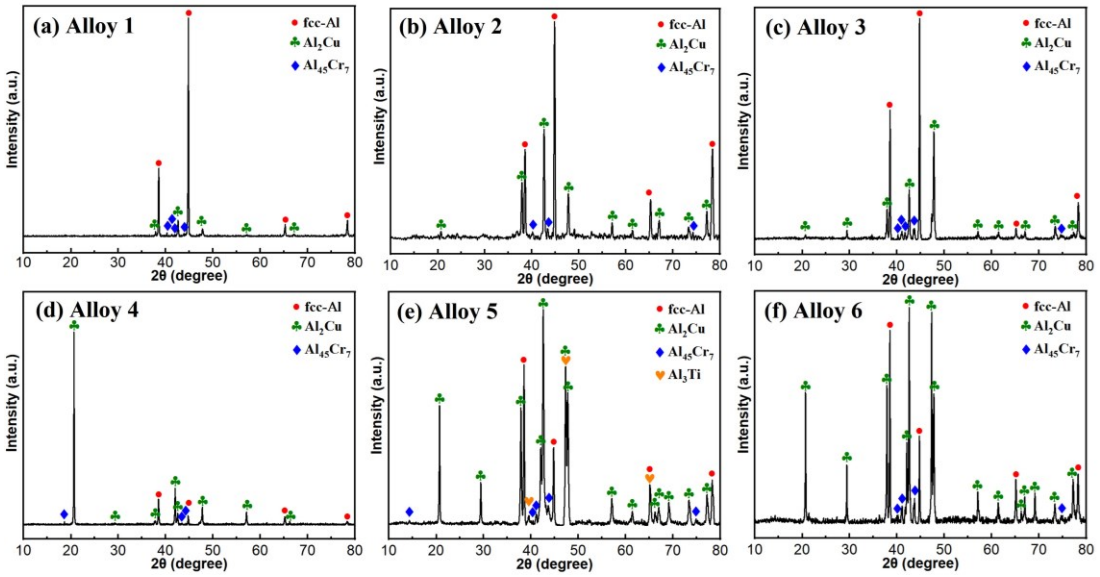

Fig. 4.3 XRD patterns of the as-cast alloys: (a) Alloy 1, (b) Alloy 2, (c) Alloy 3, (d) Alloy 4, (e) Alloy 5 and (f) Alloy 6.

Typical SEM micro images of the as-cast alloys are shown in Fig. 4.4. All six alloys exhibited multiphase features with three to four different phases, which was consistent with the XRD results shown in Fig. 4.3. In the SEM images, five different

regions (marked as A, B, C, D, and E) with corresponding phases were identified based on the shape, brightness, and SEM–EDS results. The phase type, volume fraction, and phase composition of the corresponding microstructure regions are summarized in Table 4.2.

The semiquantitative SEM–EDS analysis of each phase composition is the average value from at least five points, which is helpful to assist the phase identification. The dark Region A was determined to be the fcc-Al solid solution containing the solute atoms of Cu and Zn. The bright Region B contained Al and Cu with an atomic ratio of approximately 2:1 and was identified as the Al_2Cu phase. The Al_2Cu phase showed two shapes: (1) a bulk shape and (2) lamellar form as the eutectic phase with fcc-Al. From the low-Cu Alloy 1 to medium-Cu Alloys 2–3 and high-Cu Alloys 4–6, the volume fraction of the fcc-Al phase decreased, and the volume fraction of the Al_2Cu increased, which is supported by the XRD and Thermo-Calc simulations results. The content of the Cu solute atoms in the fcc-Al phase increased from the low- to high-Cu alloys, inducing a high degree of solid-solution strengthening. Compared to conventional Al–Cu alloys, the fcc-Al phase of the six experimental alloys contained more Cu solute atoms and was determined by the sluggish diffusion effect of the entropy alloys [5, 14, 19]. The gray Region C contained a substantial amount of Cr; considering the XRD results, it was labeled the $Al_{45}Cr_7$-type phase. Region D in Alloy 1 (Fig. 4.4a) contains high amounts of Cu and Fe, which is determined to be the Al_7Cu_2Fe phase. Region E in alloy 5 (Fig. 4.4e) contains a high amount of Ti and is identified as the Al_3Ti phase. Phases $Al_{45}Cr_7$, Al_7Cu_2Fe, and Al_3Ti have non-

stoichiometric compositions, which is common in entropic alloys and may be caused by the sluggish diffusion effect or constitutional defects [5, 15, 30-31].

The microstructure results (Fig. 4.4 and Table 4.2) reveal that all six alloys contain the three basic phases of fcc-Al, Al_2Cu, and $Al_{45}Cr_7$; this is in agreement with the XRD results. Alloys 2, 3, 4, and 6 contained only these three phases. Alloys 1 and 5 showed four phases with the Al_7Cu_2Fe phase in Alloy 1 and the Al_3Ti phase in Alloy 5. According to the Gibbs phase rule ($F = C - P + 1$, where F is the degree of freedom; C is the number of elements, and P is the number of phases), six phases may appear in a five-element alloy system when F is 0 [8]. The actual phase formation in the six alloys was simpler than expected based on the Gibbs phase rule and the Thermo-Calc simulations. It is also found that the results of the equilibrium simulation matched better with the experimental data determined by XRD and the microstructural observation compared to those of the Scheil's simulation. However, both simulations did not accurately predict the entire phase formation of six experimental alloys in term of the phase number and fraction. This is common in entropy alloy phase prediction owing to its complexities and incomplete databases [5, 17]. Despite of this, the Thermo-Calc simulations are used as the first estimation of the phase prediction [17, 19].

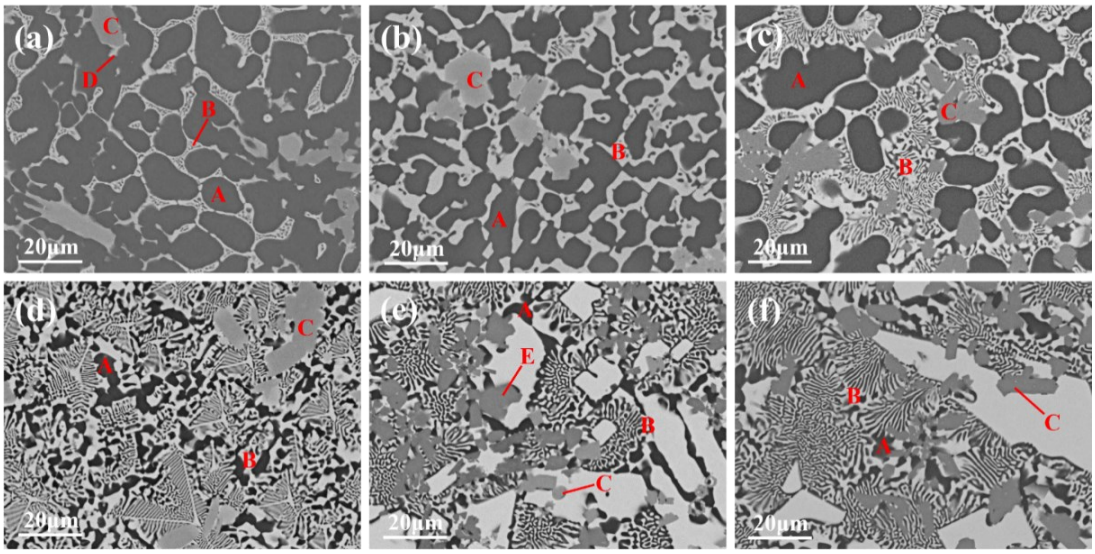

Fig. 4.4 SEM images of the as-cast microstructure: (a) Alloy 1, (b) Alloy 2, (c) Alloy 3, (d) Alloy 4, (e) Alloy 5 and (f) Alloy 6.

Table 4.2 The phase type, volume fraction and phase composition in the corresponding microstructure regions of Fig. 4.4.

Alloy	Region	Phase type	Volume fraction, vol.%	Chemical composition, at.%						
				Al	Cu	Zn	Cr	Fe	Ti	V
Alloy 1	A	fcc-Al	74.74	97.5	2	0.5	-	-	-	-
	B	Al_2Cu	14.60	76	24	-	-	-	-	-
	C	$Al_{45}Cr_7$	9.10	84	3	-	10	3	-	-
	D	Al_7Cu_2Fe	1.56	82.5	7	0.5	3	7	-	-
Alloy 2	A	fcc-Al	55.75	94	3	3	-	-	-	-
	B	Al_2Cu	34.52	72	28	-	-	-	-	-
	C	$Al_{45}Cr_7$	9.73	78	9	1	7	5	-	-
Alloy 3	A	fcc-Al	47.88	96.5	2.5	1	-	-	-	-
	B	Al_2Cu	35.52	76	24	-	-	-	-	-
	C	$Al_{45}Cr_7$	16.60	84	3.5	0.5	8	-	-	4
Alloy 4	A	fcc-Al	31.58	92	4	4	-	-	-	-
	B	Al_2Cu	57.51	70	30	-	-	-	-	-
	C	$Al_{45}Cr_7$	10.91	76	10	1	7	6	-	-
Alloy 5	A	fcc-Al	26.31	95	3.5	1.5	-	-	-	-
	B	Al_2Cu	58.06	69	31	-	-	-	-	-
	C	$Al_{45}Cr_7$	12.32	81	6	0.5	12	-	0.5	-
	E	Al_3Ti	3.31	76	1	-	7	-	16	-
Alloy 6	A	fcc-Al	28.77	95	3.5	1.5	-	-	-	-
	B	Al_2Cu	56.08	69	31	-	-	-	-	-
	C	$Al_{45}Cr_7$	15.15	82.5	5	0.5	9	-	-	3

4.3.2 Mechanical properties and thermal stability

Fig. 4.5 shows the compressive stress–strain curves of the as-cast alloys at RT. The compressive results, including the yield strength (YS, σ_y), the compressive strength (σ_{max}), and the maximum strain (ε_{max}), are summarized in Table 4.3; σ_y was obtained at a 0.2% offset strain. σ_{max} and ε_{max} are the maximum compressive strength and strain measured during deformation, respectively. A tradeoff between the strength and ductility was observed in all six alloys. Alloy 1 showed a relatively low σ_{max} of 432 MPa with a very high ε_{max} of 20%. With the increased Cu content in the medium-Cu alloys, the σ_{max} increased to 498 MPa in Alloy 2 and 564 MPa in Alloy 3, while the ε_{max} abruptly decreased to 3.21% in Alloy 2 and 1.94% in Alloy 3. The high-Cu Alloys 4–6 exhibited very high σ_{max} (exceeding 580 MPa) with low plasticities (ε_{max} of ~1%). Among the six alloys studied, Alloy 5 displayed the highest strengths, in which σ_{max} and σ_y reached 646 and 383 MPa, respectively.

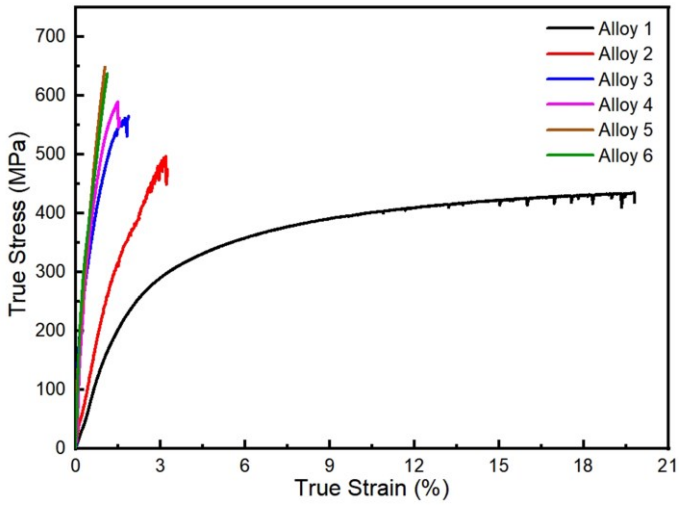

Fig. 4.5 Room-temperature compressive stress-strain curves of the as-cast alloys.

Table 4.3 Room-temperature compressive mechanical properties of the as-cast alloys.

Alloy	σ_y, MPa	σ_{max}, MPa	ε_{max}, %
Alloy 1	218	432	20.0
Alloy 2	258	498	3.21
Alloy 3	283	564	1.94
Alloy 4	351	589	1.73
Alloy 5	383	646	1.02
Alloy 6	387	628	1.09

For the elevated temperature mechanical properties, the compression tests of the as-cast alloys were initially conducted at 300 °C. The compressive stress–strain curves at 300 °C and their corresponding strengths are shown in Fig. 4.6. At elevated temperatures, the compression tests automatically stopped when reaching the preset strain of 20%. The plasticity of all alloys is no longer an issue (Fig. 4.6a), owing to the high thermal activation and easy dislocation movement at HTs. Alloy 1 displayed relatively low YS (σ_y = 111 MPa) and compressive strength (σ_{max} = 143 MPa), which were comparable to those of the conventional Al-Cu 224 cast alloy [32]. From the low-Cu alloy to the high-Cu alloys, the values of σ_y and σ_{max} significantly increase (Fig. 4.6b); Alloys 4–5 demonstrate a YS as high as 223–224 MPa at 300 °C.

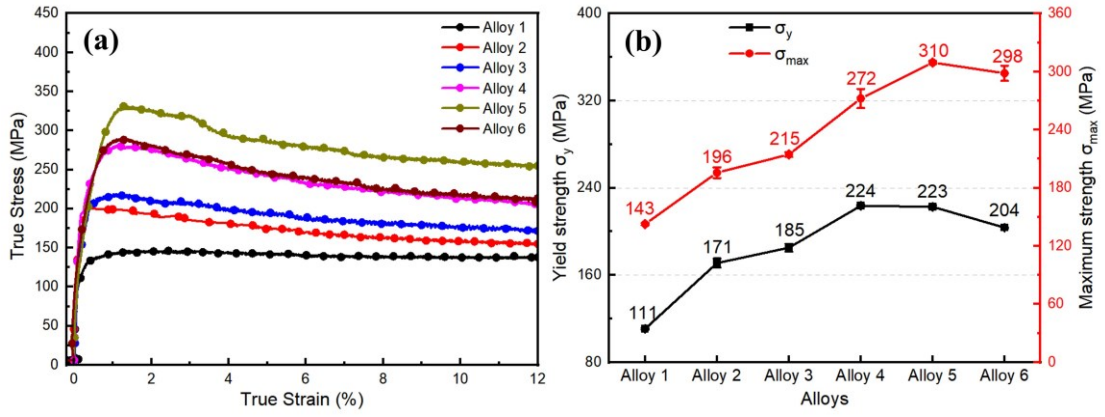

Fig. 4.6 Compressive mechanical properties of the as-cast alloys at 300 °C, (a) true stress-strain curves and (b) yield strength and maximum compressive strength.

To examine the thermal stability of the alloys, the as-cast samples were exposed to 300 °C for 100 h; compression tests of the thermally exposed samples were then conducted at 300 °C. The results of the compression tests at 300 °C and their corresponding strengths are shown in Fig. 4.7. After thermal exposure, the tendency of the strength change was similar to that of the as-cast state. Compared with the as-cast state, the σ_y of Alloy 1 slightly decreased from 111 to 108 MPa; Alloys 2 and 3 showed a decrease in σ_y from 171 to 156 MPa and 185 to 175 MPa, respectively. In the high-Cu alloys, the YS values of thermally exposed samples were very stable, and they decreased by only 5–7 MPa, which represented a 2% to 3.5% decrease after thermal exposure, indicating excellent thermal stability. Among the six alloys studied, Alloy 5 exhibited the optimal mechanical performance and thermal stability after prolonged exposure at 300 °C/100 h with its σ_{max} and σ_y reaching 272 and 218 MPa, respectively.

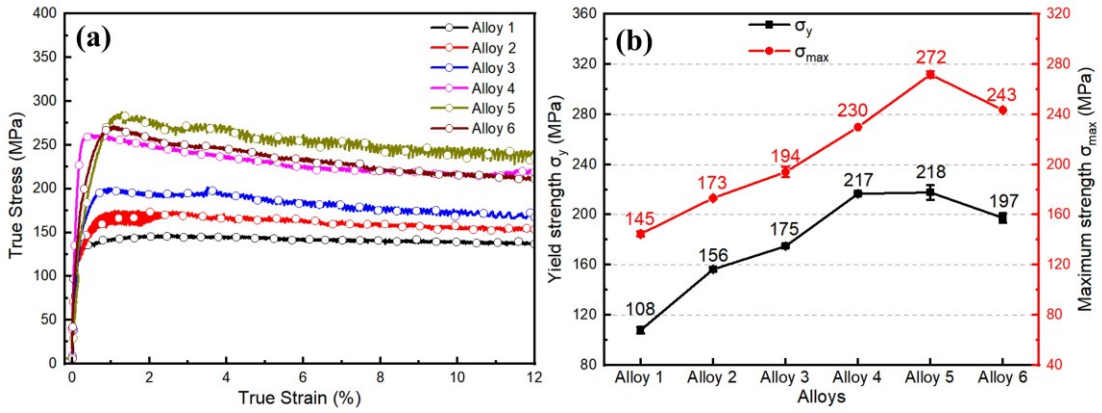

Fig. 4.7 Compressive mechanical properties at 300 °C for the samples after thermal exposure at 300 °C/100 h, (a) true stress-strain curves and (b) yield strength and maximum compressive strength.

The abovementioned results indicate that Alloy 5 demonstrates the optimal mechanical properties and thermal stability at 300 °C. To further explore the potential applications of high-Cu alloys at even higher temperatures, the as-cast samples of Alloy

5 were exposed to 350 °C, 400 °C, and 450 °C for 100 h, respectively. The compression tests were conducted at the corresponding temperatures for both as-cast and thermally exposed samples. Fig. 4.8 shows the evolution of σ_{max} and σ_y as a function of the test temperature for Alloy 5. With an increase in the test temperature, both σ_{max} and σ_y gradually decreased. However, the σ_y values of the as-cast and thermally exposed samples were very close, thereby confirming the excellent thermal stability of Alloy 5 at HTs. Even at the highest temperature (450 °C), the sample after thermal exposure at 450 °C/100 h retained a reasonable strength with σ_{max} = 80 MPa and σ_y = 78 MPa, demonstrating the significant potential and a reliable safety design margin during long-term operation at high service temperatures.

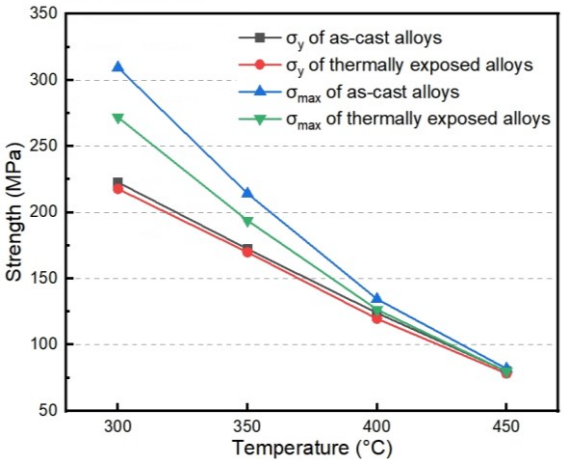

Fig. 4.8 Evolution of maximum compressive strength and yield strength of as-cast and thermally exposed Alloy 5 as a function of test temperature.

4.4 Discussion

4.4.1 Thermodynamic parameters and phase formation

During the alloy design, the computational modeling of phase diagrams and thermodynamic parameters are two important means of phase prediction for the

entropy alloys [8]. Both of the two means are used as the alloy design strategy in this study. From Figs. 4.1–4.4, the Thermo-Calc simulations are not completely consistent with the actual phase formation but are valid to a certain extent. By expanding the database to include more studies on entropy alloys, the simulations are expected to be more accurate in future.

Empirical thermodynamic parameters have been developed and applied by several researchers [8, 14, 28]. In this section, three vital parameters, the entropy of mixing ($\triangle S_{mix}$), enthalpy of mixing ($\triangle H_{mix}$), and ratio of entropy to enthalpy (Ω) are selectively introduced. These are defined as follows [8]:

$$\Delta S_{mix} = -R \sum_{i=1}^{n} c_i \ln c_i \tag{1}$$

$$\Delta H_{mix} = \sum_{i=1, j=1, i\neq j}^{n} 4\Delta H_{ij}^{mix} c_i c_j \tag{2}$$

$$\Omega = \frac{T_m \Delta S_{mix}}{|\Delta H_{mix}|} \tag{3}$$

where R is the gas constant; c_i and c_j are the atomic percentages of the i^{th} and j^{th} elements, respectively; $\triangle H_{ij}^{mix}$ is the enthalpy of mixing of binary liquid alloys of the i^{th} and j^{th} elements; $T_m=\sum_{i=1}^{n} c_i (T_m)_i$ is the average melting temperature, and $(T_m)_i$ is the melting temperature of the i^{th} element.

$\triangle S_{mix}$ represents the degree of disorder in a multi-component system. A higher $\triangle S_{mix}$ helps the formation of a disordered solid solution phase [3, 28]. $\triangle H_{mix}$ is used to describe the chemical compatibility among the principal elements. Based on the empirical summary, $\triangle H_{mix}$ should fall within a certain range; for example, for

transition element-based HEAs, this range is between -15 and 5 kJ/mol, and for Li-bearing entropy alloys, it is between -1 and 5 kJ/mol [8, 15]. **Ω** is a combination indicator of $\triangle S_{mix}$ and $\triangle H_{mix}$. A higher **Ω** correlates to a higher possibility to form solid solution phases and a lower tendency to form complex phases.

To ensure the lightweight property, the mixing density (ρ_{mix}) calculated using equation (4) was intended to be lower than 4 g/cm^3 in this study [33].

$$\rho_{mix} = \frac{\sum_{i=1}^{n} c_i A_i}{\sum_{i=1}^{n} c_i A_i / \rho_i} \quad (4)$$

where A_i and ρ_i are the atomic weight and density of the i^{th} element, respectively.

The thermodynamic parameters reflect the tendency of the system to form single solid solutions or ICs (i.e., the complexity of the phase formation). During the alloy design in this study, by adjusting the type and proportion of the elements, the $\triangle H_{mix}$ was controlled to be close to 0, and the $\triangle S_{mix}$ and **Ω** were expected to be higher, so as to achieve a simpler phase formation. As mentioned previously, the Al–Cu eutectic structure was adopted because of its appropriate Al–Cu eutectic point. Cu has a relatively high melting temperature, and $\triangle H_{AlCu}^{mix}$ is -1 kJ/mol, which aid the $\triangle H_{mix}$ of the system to be close to 0. Further, Zn was selected to facilitate the system to obtain a near-zero $\triangle H_{mix}$. Additionally, the type of high melting point element was determined largely depending on the mutual $\triangle H_{ij}^{mix}$. A balance between the density and thermodynamic parameters was achieved by adjusting the type and proportion of elements; a total of six lightweight Al-based entropy alloys were designed. The thermodynamic parameters and mixing densities were calculated based on the actual

chemical compositions of the six alloys (Table 4.4). The mixing densities of six experimental alloys varied from 2.99 to 3.74 g/cm^3, which confirmed the lightweight characteristic of the alloys. According to Yeh et al. and Sanchez et al. [10, 11], the entropy alloys can be divided into high-entropy, medium-entropy and low-entropy alloys when their entropy values are higher than 1.5R, between 1R to 1.5R or less than 1R, respectively. The six experimental alloys had the entropy values ranging from 2.66 J/mol/K (0.3R) to 5.56 J/mol/K (0.7R), belonging to the low-entropy alloy category. However, their entropy values are still much higher than those of the conventional aluminum alloys (approximately 0.1R).

The six experimental alloys in this study reveal a multiphase feature. Owing to the large chemical difference and high negative enthalpy between elements, the emergence of ICs was inevitable in the alloys [15]. At the same time, the complexities of the phase formations were slightly different among the six experimental alloys. Alloys 1 and 5 consisted of four phases, whereas the remaining four alloys contained only three phases. From Table 4.4, Alloys 1 and 5 had Ω values of 2.89 and 2.91, respectively, which were lower than those of the other alloys. The same relationship between Ω and phase complexity was found in other relevant references [14-15]. Therefore, Ω should be regarded as a more effective parameter than $\triangle S_{mix}$ and $\triangle H_{mix}$ for predicting the complexity of phase formation in the design of Al-based entropy alloys. To simplify phase formation, a high Ω is preferred. Herein, alloys with Ω values higher than 2.91 showed a simpler phase formation.

Table 4.4 Thermodynamic parameters and mixing density of the experimental alloys.

Alloys	$\triangle \mathbf{S_{mix}}$, J/mol/K	$\triangle \mathbf{H_{mix}}$, kJ/mol	$\boldsymbol{\Omega}$	$\boldsymbol{\rho_{mix}}$, g/cm^3
Alloy 1	2.66	-0.89	2.89	2.99
Alloy 2	4.65	-0.86	5.37	3.40
Alloy 3	4.21	-1.31	3.24	3.30
Alloy 4	5.56	-0.93	6.11	3.74
Alloy 5	5.38	-1.93	2.91	3.68
Alloy 6	5.28	-1.36	4.05	3.66

4.4.2 Relationship between mechanical behavior and microstructure

1. At room temperature

The strengthening mechanism in the experimental alloys was attributed to the solid solution strengthening of the fcc-Al phase and secondary phase strengthening caused by the ICs. Except for the low-Cu alloy, the experimental alloys exhibit high strengths and low plasticities at RT (Fig. 4.5). The microstructure analysis in Section 4.3.1 showed that the high content of Cu and Zn solute atoms in the fcc-Al phase induced higher solid solution strengthening than that in the conventional Al-Cu alloys. Owing to the high volume fraction of ICs, particularly in the medium- and high-Cu alloys, the intermetallics and their networks contributed to the alloy strengthening [34]. The intermetallics of Al_2Cu and Al_3Ti belong to the tetragonal crystal system, and $Al_{45}Cr_7$ has a monoclinic crystal structure. Compared with the fcc-Al phase, these three intermetallics have fewer slip systems and impeded the movement of dislocations in the fcc-Al phase; this resulted in lower plasticity and considerably higher strength [35-37]. With increasing solute atom content in the fcc-Al phase and growing volume fraction of intermetallics (Table 4.2) from the low- to high-Cu alloys, the strength of the alloys increased.

The plastic deformation caused the brittle phase to separate from the matrix or break. This resulted in cracks and a decrease in the plasticity of the alloy [38]. Fracture toughness (K_{IC}), which is a plasticity indicator, is inversely proportional to the volume fraction of ICs (f_v): $K_{IC} \propto f_v^{-1/6}$ [38-39]. As the IC content increased, ε_{max} at RT decreased significantly from the low- to the high-Cu alloys. Among the different intermetallics in the experimental alloys, the $Al_{45}Cr_7$ phase was found to be the crack initiation site. Fig. 4.9 shows the fracture features of the as-cast alloys after the RT compression test. The polished surface was parallel to the direction of the compression. $Al_{45}Cr_7$ has a higher hardness than Al_2Cu and shows a higher tendency to crack over Al_2Cu (Fig. 4.9a) [37]. Numerous tiny cracks are first observed on the $Al_{45}Cr_7$ particles, as indicated by the black arrows in Fig. 4.9a, while fcc-Al and Al_2Cu remain undamaged, indicating that the hard $Al_{45}Cr_7$ phase may be crack initiation during the compression test. The inserted image exhibits a detailed broken $Al_{45}Cr_7$. Under compression, the tiny cracks initiated from the hard $Al_{45}Cr_7$ phase, which then propagated along the soft fcc-Al matrix and grew into a large crack, leading to failure. The crack propagation in alloys with higher IC contents is obstructed to a higher extent (Fig. 4.9b in the example of Alloy 4), resulting in the high strengths of the high-Cu alloys.

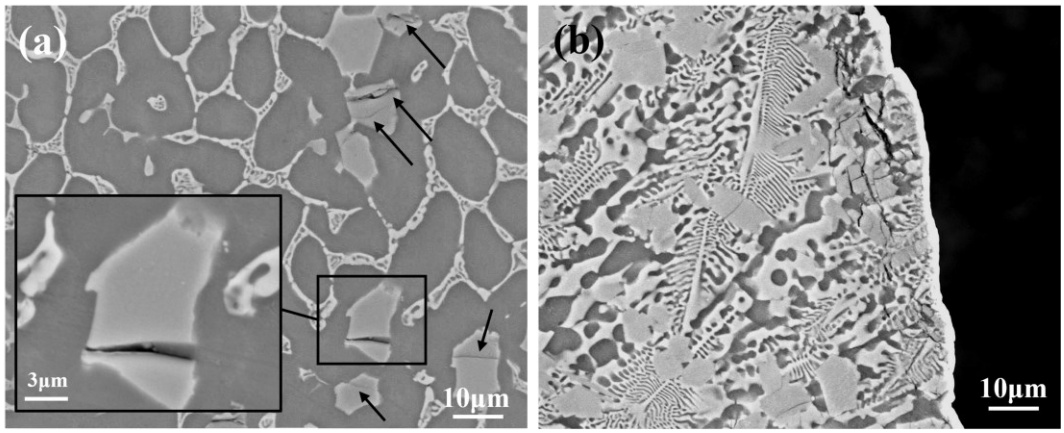

Fig. 4.9 SEM images of as-cast (a) Alloy 1 and (b) Alloy 4 after room-temperature compression tests.

2. At elevated temperatures

Owing to the higher thermal activation and more available slip systems in the fcc-Al phase at elevated temperatures, the dislocation movement and grain boundary rotation in the fcc-Al were easier. Consequently, the experimental alloys exhibited considerably higher plasticity but lower strength than those at RT. Most of the alloys retained good YS values at 300 °C because of the presence of a large volume fraction of ICs. The relationship between the YS at 300 °C and the IC volume fraction for as-cast and thermally exposed alloys is displayed in Fig. 4.10. The YS is linearly related to the volume fraction of the ICs in the alloys, thereby verifying the vital role of the ICs in the strengthening mechanism. As the fcc-Al phase became softer at elevated temperatures, the ICs and their network were the predominant components to support the structure during the plastic deformation by impeding the dislocation movement and grain boundary migration. Fig. 4.11 shows the arrangement of dislocations after compression tests. The selected area diffraction patterns inserted in Fig. 4.11a reveal the two main phases, fcc-Al and Al_2Cu, in the alloy. The massive accumulation of

dislocations near the ICs indicates that the ICs significantly hinder the dislocation movement at elevated temperatures.

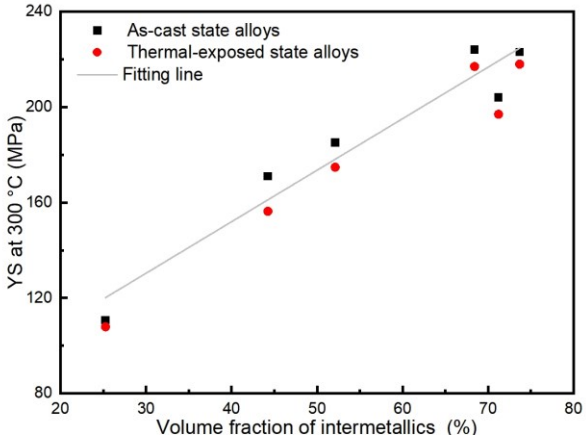

Fig. 4.10 Linear relationship between the YS at 300 °C and the volume fraction of ICs.

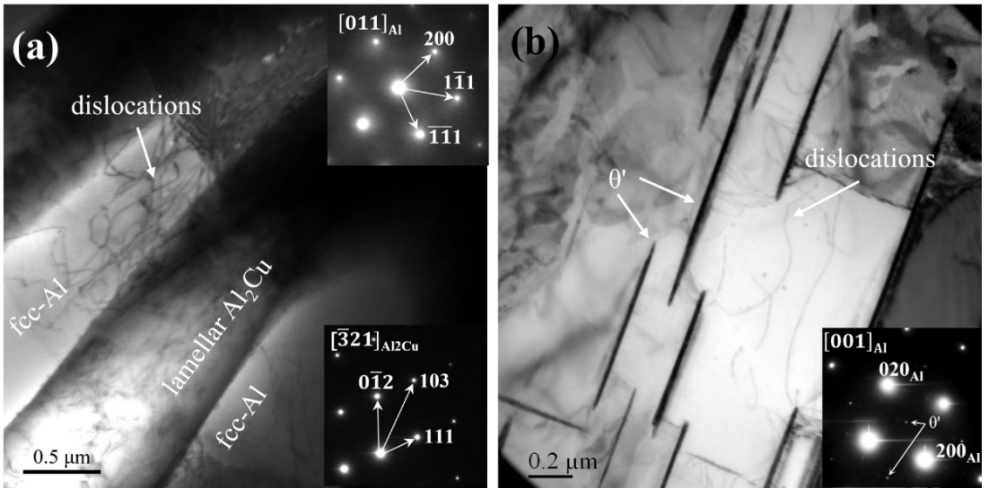

Fig. 4.11 Bright-field TEM images of after thermal exposure at 300 °C/100 h and compression test at 300 °C, (a) Alloy 5 and (b) Alloy 1.

In the thermally exposed alloys, all ICs remained unchanged, whereas the supersaturated fcc-Al phase decomposed. The SEM images (Fig. 4.12) show evidence of stable intermetallics (marked in red in Fig. 4.12a–c) and a decomposed fcc-Al phase (indicated by white arrows in Fig. 4.12d). The long needle-like phase that precipitated from the fcc-Al is identified as θ′ (Fig. 4.11b). The formation of the θ′ precipitates in

the fcc-Al implied that the solid solution strengthening caused by Cu solute atoms was replaced by the precipitation strengthening of θ′. As the type and proportion of the ICs remained the same after thermal exposure, the strength difference between the as-cast and thermally exposed alloys was attributed to the change in the strengthening mechanism of the fcc-Al phase.

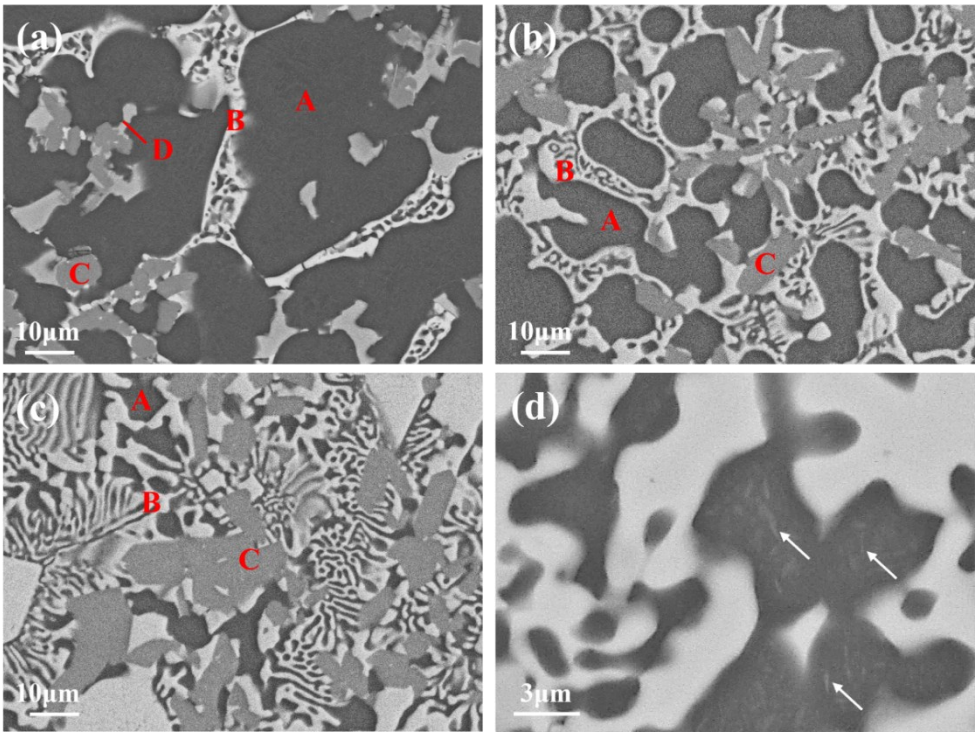

Fig. 4.12 SEM images of the thermally exposed alloys: (a) Alloy 1, (b) Alloy 3, (c) Alloy 6, (d) an enlarged view showing precipitates in the fcc-Al phase of Alloy 6.

The YS increment attributed to solid solution strengthening ($\Delta\sigma_{SS}$) caused by Cu and the precipitation strengthening (σ_p) caused by θ′ were calculated according to the following equations:

$$\Delta\sigma_{SS} = \sum \Delta\sigma_{Cu} c_{Cu} \quad (5)$$

$$\sigma_p = \frac{MGb}{2\pi\sqrt{1-\nu}}\left(\frac{1}{1.23\frac{1.030}{\sqrt{N_V d_t}}-\frac{\pi d_t}{8}-1.061t_t}\right)\ln\frac{0.981\sqrt{d_t t_t}}{b} \quad (6)$$

where $\Delta\sigma_{Cu}$ and c_{Cu} are the theoretical strengthening contribution and weight fraction of the Cu solute atoms, respectively; M is the Taylor factor (3 for Al); G is the shear modulus (21.1 GPa for Al); b is the magnitude of the Burgers vector (0.284 nm for Al); ν is the Poisson ratio (0.33 for Al); N_v, d_t, and t_t are the number density, effective width, and effective thickness of the θ′ precipitates, respectively [40].

As no published data were available on $\Delta\sigma_{Cu}$ at HTs, $\Delta\sigma_{Cu}$ was estimated to be 10 MPa/wt.% at 300 °C using the YS difference of 18 MPa between AA1100-O and AA2014-O alloys at 315 °C and their Cu solute atoms difference of 1.8 wt.% [41]. The contents of the Cu solute atoms in the fcc-Al phase of as-cast Alloys 1, 2, and 5 were 4.5, 7.0, and 8.0 wt.%, respectively. The quantification of θ′ in thermally exposed alloys is presented in Table 4.5. Based on equations (5) and (6), the $\Delta\sigma_{Cu}$ and σ_p in Alloys 1, 2, and 5 at 300 °C were 45, 70, and 80 MPa and 40, 44, and 58 MPa, respectively. The volume fractions of the fcc-Al phase in Alloys 1, 2, and 5 were 74.74%, 55.75%, and 26.31%, respectively. Considering the rule of mixtures, the final YS decrease caused by the fcc-Al phase in Alloys 1, 2, and 5 was 3, 14, and 6 MPa, respectively, which was consistent with the experimental results [42].

Table 4.5 Quantification results of θ’ precipitates after thermal exposure.

Alloys	Number density N_v, μm^{-3}	Effective width d_t, nm	Effective thickness t_t, nm
Alloy 1	2.97	731.4	23.9
Alloy 2	5.59	537.2	25.9
Alloy 5	15.3	368.4	26.5

From calculations, the YS increments attributed to $\Delta\sigma_{Cu}$ and σ_p in Alloy 5 were 21 and 15 MPa, respectively; these were 9% and 7% of the total YS, respectively. As the temperature increased, the ICs played a predominant role in impeding dislocation movement, and the effect due to the fcc-Al was insignificant. Alloy 5 showed a highly stable YS at elevated temperatures up to 450 °C. The change in the strengthening mechanism of the fcc-Al affects the overall plastic performance of the alloys; the maximum compressive strengths at 300 °C of the high-Cu alloys after thermal exposure are considerably lower than those of the as-cast alloys (Figs. 4.6–4.7). With an increase in temperature, the difference becomes smaller because of the less effect of the fcc-Al phase at HTs (Fig. 4.8).

3. Phase stability and thermal stability of the alloys

The results of the Thermo-Calc simulations indicate that all ICs in the experimental alloys (Al_2Cu, $Al_{45}Cr_7$, Al_7Cu_2Fe, and Al_3Ti) were thermodynamically stable up to 500 °C (Fig. 4.1). Fig. 4.13 shows the DSC curves of the as-cast high-Cu Alloys 4–6. Up to the melting point (~523 °C) of the eutectic phases of Al_2Cu and fcc-Al, no phase transformation was observed. This further confirmed that all ICs (Al_2Cu, $Al_{45}Cr_7$, Al_7Cu_2Fe, and Al_3Ti) observed in the microstructure were thermally stable. This is consistent with the YS values of the high-Cu alloys negligibly changing after thermal exposure at 300 °C–450 °C for 100 h (Figs. 4.6–4.8); the high-Cu alloys contained a large portion of ICs (~70 vol.%) in the microstructure. Owing to the intermetallic phase stability, excellent thermal stability and good mechanical performance at temperatures even higher than 450 °C could be expected. It is reported that Al_2Cu does not develop appreciable plasticity below 527 °C [43]. However, at

temperatures ranging from 300 °C to 450 °C, the high-Cu alloys developed herein exhibited considerable plasticity, indicating the positive interaction between the fcc-Al and ICs in the alloys for HT applications.

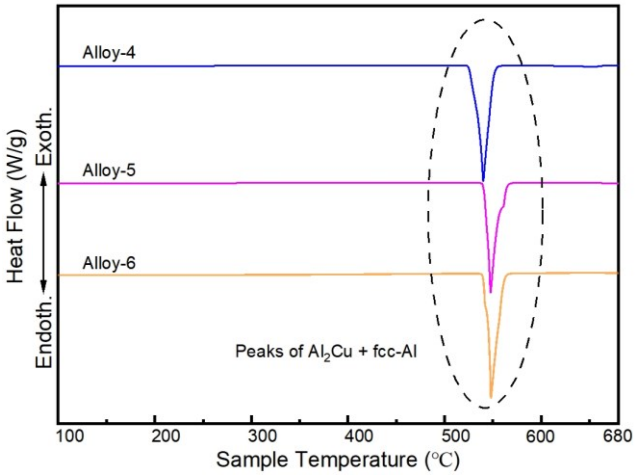

Fig. 4.13 DSC heating curves of as-cast Alloys 4-6 showing no phase transformation until the melting point (~523 °C).

4.4.3 Comparison of elevated temperature strength for various aluminum alloys

Owing to the lower melting temperature of aluminum, most aluminum alloys generally exhibit poor mechanical properties for HT applications compared to common structural metals (e.g., steel). The conventional aluminum cast alloys that are widely used in the automotive and aerospace industries are divided into three groups: (1) Al-Cu alloys containing 4–5.5 wt.% Cu, (2) Al–Si–Mg 356-type alloys containing 6–8 wt.% Si and 0.25–0.45 wt.% Mg, and (3) Al–Si–Cu 319-type alloys containing 5–9 wt.% Si and 3–4 wt.% Mg. Table 4.6 summarizes the YS values at 300–315 °C for the as-prepared experimental alloys and other representative aluminum alloys. The conventional 356/319-based alloys are known to have an excellent combination of

ductility and strength at RT, but their elevated temperature YS values are significantly low (33–50 MPa after 100 h of thermal exposure, #9 and #11 in Table 4.6). The conventional Al–Cu alloys possess relatively high elevated temperature strengths with YS ranging from 90 to 110 MPa after 100 h of thermal exposure (#5, #6, and #7). These values are similar to those of low-Cu Alloy 1 (#1).

Recently, significant efforts have been devoted to improving the elevated temperature mechanical properties of various aluminum cast alloys by microalloying with transition elements and/or introducing thermally stable dispersoids [23, 40, 44-45]. The elevated temperature properties of the cast alloys in the three groups are significantly improved (#8, #10, and #11) but are still limited, which is similar to the case of aluminum wrought alloys. The conventional wrought alloys exhibited considerably low YS values at elevated temperatures (40–55 MPa after 100 h of thermal exposure, #13, #14, and #16). With modified alloy chemistry and processing, their elevated temperatures were considerably enhanced (#15 and #17). However, their YS values at 300 °C/100 h remained below 100 MPa [46-47]. The three high-Cu alloys (#2, #3, and #4) in this study showed very high YS values of ~200 MPa at 300 °C and good thermal stability after prolonged thermal exposure. These values are beyond the attainable level of the current aluminum alloys. Therefore, this study demonstrates a novel approach to significantly improve the elevated temperature properties.

The mechanical performance of the representative Alloy 5 at HTs of 350 °C–450 °C (Fig. 4.8) is considerably superior to that of most conventional aluminum alloys [41]. Owing to the favorable mechanical behavior at HTs and the excellent thermal stability, the concept of lightweight entropy alloys adopted here, particularly the high-

Cu entropy alloys, provides promising prospects for HT applications, including cartridge cases that can withstand HTs and high chamber pressures, infrastructural materials servicing fire-prone areas for prolonging the escape time and maintaining the structural integrity, and automotive engine parts functioning at rising operation temperatures.

Table 4.6 Comparison of the YS at 300-315 °C (MPa) between various aluminum alloys.

No	Alloys	YS at 300-315 °C		Reference
		0.5 h	After 100h exposed	
1	Alloy 1 ($Al_{93}Cu_4Zn_1Cr_1Fe_1$)	111	108	This work
2	Alloy 4 ($Al_{78}Cu_{18}Zn_2Cr_1Fe_1$)	224	217	This work
3	Alloy 5 ($Al_{78}Cu_{18}Zn_1Cr_2Ti_1$)	223	218	This work
4	Alloy 6 ($Al_{78}Cu_{18}Zn_1Cr_2V_1$)	204	197	This work
5	Conventional 206-T7 Al-Cu cast alloy	160	92	48
6	Conventional 240-T7 Al-Cu cast alloy	110*	105*	41
7	Conventional 224-T7 Al-Cu cast alloy	125*	110*	41
8	Modified 224-T7 Al-Cu cast alloy	175	142	40
9	Conventional 356 Al-Si-Mg cast alloy	--	33	23
10	Modified 356 Al-Si-Mg cast alloy	--	47	23
11	Conventional 319 Al-Si-Cu cast alloy	100	51	45
12	Modified 319 Al-Si-Cu cast alloy	113	61	45
13	Conventional 2024-T6 Al-Cu wrought alloy	95*	55*	41
14	Conventional 3004-T7 Al-Mn wrought alloy	41*	41*	41
15	Modified 3004-T7 Al-Mg wrought alloy	93	93	46
16	Conventional 5083-T7 Al-Mg wrought alloy	52*	52*	41
17	Modified 5083-T7 Al-Mg wrought alloy	88	88	47

Note: * Test temperature and thermal exposure temperature is 315 °C [41].

4.5 Conclusions

1) Six lightweight Al-based entropy alloys were designed and investigated. All six alloys possessed a low density varying from 2.99 to 3.74 g/cm^3 and contained three basic phases (fcc-Al, Al_2Cu, and $Al_{45}Cr_7$). Alloys 1 and 5 exhibited four phases with the Al_7Cu_2Fe phase in Alloy 1 and the Al_3Ti phase in Alloy 5. The actual alloys showed simpler phase formation compared with the Thermo-Calc simulation and Gibbs phase rule results.

2) Owing to the large chemical difference and high negative enthalpy between Al and the alloying elements, the appearance of a large quantity of intermetallic compounds (ICs) was inevitable in Al-based entropy alloys. With increasing Cu content, the volume fraction of the ICs significantly increased and resulted in increased strength and reduced plasticity.

3) The high-Cu Alloys 4–6 exhibited excellent compressive strength (σ_{max} > 580 MPa) with low plasticity (ε_{max} of ~1%) at RT owing to the high volume fraction of ICs. At 300 °C, all alloys exhibited considerably higher plasticities, and the YS values of Alloys 4–6 surpassed 200 MPa.

4) After thermal exposure at 300 °C for 100 h, the YS values at 300 °C of Alloys 4–6 changed negligibly and retained at the level of ~200 MPa. The results were considerably superior to those obtained for most conventional aluminum alloys.

5) Among the six alloys studied, Alloy 5 ($Al_{78}Cu_{18}Zn_1Cr_2Ti_1$) exhibited the highest mechanical performance and thermal stability after thermal exposure at 300 °C/100 h; its σ_{max} and σ_y at 300 °C reached 272 and 218 MPa, respectively.

6) The excellent thermal stability of the high-Cu alloys up to 450 °C was further confirmed. Combined with their high YS values, the novel lightweight entropy alloys provide promising prospects for high temperature applications.

References

[1] I. J. Polmear, M. J. Couper, Design and development of an experimental wrought aluminum alloy for use at elevated temperatures, Metall. Trans. A 19(4) (1988) 1027-1035. https://doi.org/10.1007/BF02628387

[2] M. Asadikiya, S. Yang, Y. Zhang, C. Lemay, D. Apelian, Y. Zhong, A review of the design of high-entropy aluminum alloys: a pathway for novel Al alloys, J. Mater. Sci. 56(21) (2021) 12093-12110. https://doi.org/10.1007/s10853-021-06042-6

[3] J.W. Yeh, S.K. Chen, S.J. Lin, J.Y. Gan, T.S. Chin, T.T. Shun, C.H. Tsau, S.Y. Chang, Nanostructured high-entropy alloys with multiple principal elements: novel alloy design concepts and outcomes, Adv. Eng. Mater. 6(5) (2004) 299-303. https://doi.org/10.1002/adem.200300567

[4] B. Cantor, I.T.H. Chang, P. Knight, A.J.B. Vincent, Microstructural development in equiatomic multicomponent alloys, Mater. Sci. Eng. A 375 (2004) 213-218. https://doi.org/10.1016/j.msea.2003.10.257

[5] J.M. Sanchez, I. Vicario, J. Albizuri, T. Guraya, J.C. Garcia, Phase prediction, microstructure and high hardness of novel light-weight high entropy alloys, J. Mater. Res. Technol. 8(1) (2019) 795-803. https://doi.org/10.1016/j.jmrt.2018.06.010

[6] W. Zhang, P.K. Liaw, Y. Zhang, Science and technology in high-entropy alloys, SCMs 61(1) (2018) 2-22. https://doi.org/10.1007/s40843-017-9195-8

[7] J. Chen, X. Zhou, W. Wang, B. Liu, Y. Lv, W. Yang, D. Xu, Y. Liu, A review on fundamental of high entropy alloys with promising high–temperature properties, J. Alloys Compd. 760 (2018) 15-30. https://doi.org/10.1016/j.jallcom.2018.05.067

[8] Y. Zhang, T.T. Zuo, Z. Tang, M.C. Gao, K.A. Dahmen, P.K. Liaw, Z.P. Lu, Microstructures and properties of high-entropy alloys, Prog. Mater. Sci. 61 (2014) 1–93. https://doi.org/10.1016/j.pmatsci.2013.10.001

[9] D.B. Miracle, O.N. Senkov, A critical review of high entropy alloys and related concepts, Acta Mater. 122 (2017) 448-511. https://doi.org/10.1016/j.actamat.2016.08.081

[10] J.W. Yeh, Alloy design strategies and future trends in high-entropy alloys, JOM 65(12) (2013) 1759-1771. https://doi.org/10.1007/s11837-013-0761-6

[11] J.M. Sanchez, I. Vicario, J. Albizuri, T. Guraya, E.M. Acuña, Design, microstructure and mechanical properties of cast medium entropy aluminium alloys, Sci. Rep. 9(1) (2019) 1-12. https://doi.org/10.1038/s41598-019-43329-w

[12] Y.E.H. Jien-Wei, Recent progress in high entropy alloys, Ann. Chim. Sci. Mat. 31(6) (2006) 633-648. 10.3166/acsm.31.633-648

[13] K.S. Tun, P. Murugan, T.S. Srivatsan, M. Gupta, Synthesis and Characterization of aluminium based multicomponent alloys, Mater. Today 46 (2021) 1210-1214. https://doi.org/10.1016/j.matpr.2021.02.066

[14] L. Shao, T. Zhang, L. Li, Y. Zhao, J. Huang, P.K. Liaw, Y. Zhang, A low-cost lightweight entropic alloy with high strength, J. Mater. Eng. Perform. 27(12) (2018) 6648-6656. https://doi.org/10.1007/s11665-018-3720-0

[15] X. Yang, S.Y. Chen, J.D. Cotton, Y. Zhang, Phase stability of low-density, multiprincipal component alloys containing aluminum, magnesium, and lithium, JOM 66(10) (2014) 2009-2020. https://doi.org/10.1007/s11837-014-1059-z

[16] R. Li, X. Li, J. Ma, Y. Zhang, Sub-grain formation in Al–Li–Mg–Zn–Cu lightweight entropic alloy by ultrasonic hammering, Intermetallics, 121 (2020) 106780. https://doi.org/10.1016/j.intermet.2020.106780

[17] E.J. Baek, T.Y. Ahn, J.G. Jung, J.M. Lee, Y.R. Cho, K. Euh, Effects of ultrasonic melt treatment and solution treatment on the microstructure and mechanical properties of low-density multicomponent Al70Mg10Si10Cu5Zn5 alloy, J. Alloys Compd. 696 (2017) 450-459. https://doi.org/10.1016/j.jallcom.2016.11.305

[18] C. Ji, A. Ma, J. Jiang, Mechanical properties and corrosion behavior of novel Al-Mg-Zn-Cu-Si lightweight high entropy alloys, J. Alloys Compd. 900 (2022) 163508. https://doi.org/10.1016/j.jallcom.2021.163508

[19] J.M. Sanchez, I. Vicario, J. Albizuri, T. Guraya, N.E. Koval, J.C. Garcia, Compound formation and microstructure of as-cast high entropy aluminums, Metals 8(3) (2018) 167. https://doi.org/10.3390/met8030167

[20] T.Y. Ahn, J.G. Jung, E.J. Baek, S.S. Hwang, K. Euh, Temperature dependence of precipitation behavior of Al–6Mg–9Si–10Cu–10Zn–3Ni natural composite and its impact on mechanical properties, Mater. Sci. Eng. A 695 (2017) 45-54. https://doi.org/10.1016/j.msea.2017.04.015

[21] R. Li, Z. Ren, Y. Wu, Z. He, P.K. Liaw, J. Ren, Y. Zhang, Mechanical behaviors and precipitation transformation of the lightweight high-Zn-content Al–Zn–Li–Mg–Cu

alloy, Mater. Sci. Eng. A 802 (2021) 140637. https://doi.org/10.1016/j.msea.2020.140637

[22] B. Zhang, P.K. Liaw, J. Brechtl, J. Ren, X. Guo, Y. Zhang, Effects of Cu and Zn on microstructures and mechanical behavior of the medium-entropy aluminum alloy. J. Alloys Compd. 820 (2020) 153092. https://doi.org/10.1016/j.jallcom.2019.153092

[23] A.R. Farkoosh, X.G. Chen, M. Pekguleryuz, Dispersoid strengthening of a high temperature Al–Si–Cu–Mg alloy via Mo addition, Mater. Sci. Eng. A 620 (2015)181-189. https://doi.org/10.1016/j.msea.2014.10.004

[24] Y. Lu, Y. Dong, S. Guo, L. Jiang, H. Kang, T. Wang, B. Wen, Z. Wang, J. Jie, Z. Cao, H. Ruan, A promising new class of high-temperature alloys: eutectic high-entropy alloys, Sci. Rep. 4(1) (2014) 1-5. https://doi.org/10.1038/srep06200

[25] Y. Lu, X. Gao, L. Jiang, Z. Chen, T. Wang, J. Jie, H. Kang, Y. Zhang, Y., S. Guo, H. Ruan, Y. Zhao, Directly cast bulk eutectic and near-eutectic high entropy alloys with balanced strength and ductility in a wide temperature range, Acta Mater. 124 (2017) 143-150. https://doi.org/10.1016/j.actamat.2016.11.016

[26] M. Wang, Y. Lu, T. Wang, C. Zhang, Z. Cao, T. Li, P.K. Liaw, A novel bulk eutectic high-entropy alloy with outstanding as-cast specific yield strengths at elevated temperatures, Scr. Mater. 204 (2021) 114132. https://doi.org/10.1016/j.scriptamat.2021.114132

[27] Y. Lu, Y. Dong, H. Jiang, Z. Wang, Z. Cao, S. Guo, T. Wang, T. Li, P.K. Liaw, Promising properties and future trend of eutectic high entropy alloys, Scr. Mater. 187 (2020) 202-209. https://doi.org/10.1016/j.scriptamat.2020.06.022

[28] Y. Zhang, X. Yang, and P.K. Liaw, Alloy design and properties optimization of high-entropy alloys, JOM 64(7) (2012) 830-838. https://doi.org/10.1007/s11837-012-0366-5

[29] R. Li, J. Gao, K. Fan, Study to microstructure and mechanical properties of Mg containing high entropy alloys, Materials Science Forum, Trans Tech Publications Ltd, 650 (2010) 265-271. https://doi.org/10.4028/www.scientific.net/MSF.650.265

[30] K.Y. Tsai, M.H. Tsai, J.W. Yeh, Sluggish diffusion in co–cr–fe–mn–ni high-entropy alloys, Acta Mater. 61(13) (2013) 4887-4897. https://doi.org/10.1016/j.actamat.2013.04.058

[31] C.T. Liu, J.H. Zhu, M.P. Brady, C.G. McKamey, L.M. Pike, L.M., Physical metallurgy and mechanical properties of transition-metal Laves phase alloys, Intermetallics 8(9-11) (2000) 1119-1129. https://doi.org/10.1016/S0966-9795(00)00109-6

[32] D. Li, K. Liu, J. Rakhmonov, X.G. Chen, Enhanced thermal stability of precipitates and elevated-temperature properties via microalloying with transition metals (Zr, V and Sc) in Al–Cu 224 cast alloys, Mater. Sci. Eng. A 827 (2021) 142090. https://doi.org/10.1016/j.msea.2021.142090

[33] P. Chauhan, S. Yebaji, V.N. Nadakuduru, T. Shanmugasundaram, Development of a novel light weight Al35Cr14Mg6Ti35V10 high entropy alloy using mechanical alloying and spark plasma sintering, J. Alloys Compd. 820 (2020) 153367. https://doi.org/10.1016/j.jallcom.2019.153367

[34] S.G. Shabestari, M. Ghanbari, Effect of plastic deformation and semisolid forming on iron–manganese rich intermetallics in Al–8Si–3Cu–4Fe–2Mn alloy, J. Alloys Compd. 508(2) (2010), 315-319. https://doi.org/10.1016/j.jallcom.2010.08.043

[35] M. Aravind, P. Yu, M.Y. Yau, D.H. Ng, Formation of Al2Cu and AlCu intermetallics in Al (Cu) alloy matrix composites by reaction sintering, Mater. Sci. Eng. A 380(1-2) (2004) 384-393. https://doi.org/10.1016/j.msea.2004.04.013

[36] Z. Liu, M. Rakita, X. Wang, W. Xu, Q. Han, In situ formed Al3Ti particles in Al alloy matrix and their effects on the microstructure and mechanical properties of 7075 alloy, J. Mater. Res. 29(12) (2014) 1354-1361. https://doi.org/10.1557/jmr.2014.123

[37] M.V. Glazoff, A. Khvan, V.S. Zolotorevsky, N.A. Belov, A. Dinsdale, Casting aluminum alloys: their physical and mechanical metallurgy, second ed., Butterworth-Heinemann. https://doi.org/10.1016/C2015-0-02446-7

[38] R. Ding, I.P. Jones, Influence of carbides on the strength and toughness of a niobium alloy, J. Mater. Sci. Technol. 26(3) (2010) 323-332. https://doi.org/10.1179/174328409X408884

[39] B. Morere, J.C. Ehrström, P.J. Gregson, I. Sinclair, Microstructural effects on fracture toughness in AA7010 plate, Metall. Mater. Trans. A 31(10) (2000) 2503-2515. https://doi.org/10.1007/s11661-000-0195-y

[40] J. Rakhmonov, K. Liu, L. Pan, F. Breton, X.G. Chen, Enhanced mechanical properties of high-temperature-resistant Al–Cu cast alloy by microalloying with Mg, J. Alloys Compd. 827 (2020) 154305. https://doi.org/10.1016/j.jallcom.2020.154305

[41] J.G. Kaufman, Properties of aluminum alloys: tensile, creep, and fatigue data at high and low temperatures, ASM international, 1999.

[42] T. W. Clyne, P. J. Withers, An introduction to metal matrix composites, Cambridge university press, 1995.

[43] L.F. Mondolfo, Aluminum alloys: structure and properties, Elsevier, 2013.

[44] K. Liu, X.G. Chen, Development of Al–Mn–Mg 3004 alloy for applications at elevated temperature via dispersoid strengthening, Mater. Des. 84 (2015) 340-350. https://doi.org/10.1016/j.matdes.2015.06.140

[45] L. Jin, K. Liu, X.G. Chen, Evolution of dispersoids and their effects on elevated-temperature strength and creep resistance in Al-Si-Cu 319 cast alloys with Mn and Mo additions, Mater. Sci. Eng. A 770 (2020) 138554. https://doi.org/10.1016/j.msea.2019.138554

[46] K. Ma, E.M. Elgallad, Z.X. Chen, B.L. Xiao, X.G. Chen, Improving the elevated-temperature mechanical properties of AA3004 hot-rolled sheets by microalloying with Mo and optimizing the process route. J. Mater. Res. Technol. 19 (2022) 4489-4503. https://doi.org/10.1016/j.jmrt.2022.06.171

[47] A.Y. Algendy, K. Liu, P. Rometsch, N. Parson, X.G. Chen, Effects of AlMn dispersoids and Al3(Sc,Zr) precipitates on microstructure and ambient/elevated-temperature mechanical properties of hot-rolled AA5083 alloys, Mater. Sci. Eng. A. 855 (2022) 143950. https://doi.org/10.1016/j.msea.2022.143950

[48] J. Rakhmonov, K. Liu, X.G. Chen, Effects of Compositional Variation on the Thermal Stability of θ′-Al2Cu Precipitates and Elevated-Temperature Strengths in Al-Cu 206 Alloys, J. Mater. Eng. Perform. 29(11) (2020) 7221-7230.

Chapter 5

Spatial reconstruction, microstructure-based modeling of compressive deformation behavior, and prediction of mechanical properties in lightweight Al-based entropy alloys

(Under submission)

Abstract

Lightweight Al-based entropy alloys are newly emerged materials with promising potential for structural applications; however, their modeling and strengthening prediction require further exploration. In this study, the spatial distributions of various phases in three Al-based entropy alloys were investigated. A closely interconnected intermetallic compound (IC) network comprising Al_2Cu and $Al_{45}Cr_7$ phases was identified. Finite element (FE) modeling was conducted based on the reconstructed three-dimensional microstructure to simulate compressive deformation behavior. The IC network served as the main stress bearer during deformation. Thin sections in the Al_2Cu network were the weak sites where stress concentration and damage first occurred. However, the breakage of this limited region contributes to relatively coordinated deformation and extended plasticity. The breakage of large particles accounts for the final alloy failure. The results of the FE model were compared with the experimentally measured stress-strain behavior and mechanical properties, showing very good agreement. Given the non-uniform distribution of strain and stress during deformation, a strengthening model, merging the Voigt and Reuss models, was

also developed to predict the mechanical properties of Al-based entropy alloys with the aim of facilitating Al-based entropy alloy development.

Keywords: Al-based entropy alloys; 3D reconstruction; Finite element modeling; Mechanical properties; Intermetallic network.

5.1 Introduction

In recent years, the development of a green economy has led to a substantial increase in demand for lightweight Al alloys in the automotive, aerospace, and infrastructure industries [1, 2]. The advancement of traditional Al alloys has encountered some challenges, including their relatively low strength and high sensitivity to elevated temperatures [3, 4]. Recently, a class of newly emerging lightweight materials, Al-based entropy alloys, also known as multicomponent Al alloys [5, 6], has garnered the attention of researchers. Inspired by the concept and excellent properties of high-entropy alloys, these alloys have incorporated multiple secondary elements in significant proportions. Through their combination with various elements, Al-based entropy alloys have been reported to surpass the limits of conventional Al alloys, exhibiting exceptional material and mechanical properties with relatively low densities [7-10].

Yang et al. [11] developed two multicomponent alloys, $Al_{80}Li_5Mg_5Zn_5Cu_5$ and $Al_{80}Li_5Mg_5Zn_5Sn_5$, featuring a low density of 2.85 g/cm³ and exhibiting a high compressive strength exceeding 800 MPa while retaining a plasticity of up to 17%. Baek et al. [12] reported that the $Al_{70}Mg_{10}Si_{10}Cu_5Zn_5$ alloy exhibited excellent

compressive strength at temperatures below 200 °C when compared to the conventional A356, A390, and piston alloys. In our previous work [5], a series of Al-Cu entropy alloys were designed, and some of them, namely $Al_{78}Cu_{18}Zn_2Cr_1Fe_1$, $Al_{78}Cu_{18}Zn_1Cr_2Ti_1$, and $Al_{78}Cu_{18}Zn_1Cr_2V_1$ alloys, achieved high mechanical strengths at room temperature as well as excellent strength and thermal stability up to 450 °C. Therefore, Al-based entropy alloys are promising structural materials with exceptional mechanical properties at both room temperature and elevated temperatures.

Several studies have explored the mechanisms underlying the exceptional strength of Al-based entropy alloys. Precipitation and solution strengthening have been reported to make substantial contributions [7, 13, 14]. However, these factors alone are not sufficient to explain why as-cast alloys, characterized by sparse precipitates and relatively limited solute atoms, may possess high strength. The lightweight Al-based entropy alloys always exhibit a microstructure characterized by multiple phases [10], which significantly contribute to their strength [15]. For instance, Biswas et al. [16] reported that an interconnecting network of Mg_2Si increased the compressive strength of Al-Mg_2Si composites from 205 to 567 MPa. Our previous work [17] showed that intermetallic compounds (ICs) can form a well-connected network in entropy alloys that significantly improves both the room- and elevated-temperature mechanical properties. Nevertheless, further investigation is required to understand the strengthening mechanisms associated with ICs and damage mechanisms in entropy alloys.

Numerical modeling and fundamental understanding are essential for developing new materials with enhanced properties [18]. The finite element method (FEM) is an

important tool for conducting engineering analyses including heat transfer, fluid flow, and material fracture. By employing constitutive equations and numerical methods, the FEM can provide insights into material behavior under varying conditions, offering the potential to streamline research efforts and minimize the time and resources typically required for analogous experimental studies [19]. As previously indicated, Al-based entropy alloys consist of numerous phases. The challenge confronting contemporary material designers lies in comprehending the implications of nonuniformities and elucidating the mechanisms underlying failure or damage in multiphase materials [20-22]. Over the last two decades, FEM has demonstrated reliability for evaluating the deformation characteristics of alloys comprising multiple phases [23-26]. Liu et al. [27] investigated the crack propagation behavior of die-cast AlSiMgMn alloys using in situ scanning electron microscopy (SEM) observations and finite element (FE) simulations, and concluded that pores of lower sphericity were more likely to cause serious stress concentration and local microcracks. Jiang et al. [28] investigated the effect of particle size on reinforcing in composites with FEM analysis and found that the decrease in size improved the mechanical response. Williams et al. [29] studied the effect of particle/matrix interface debonding in Al/SiC composites using a three-dimensional (3D) microstructure-based FEM and reported that angular particles exhibited a higher degree of load transfer and were more sensitive to debonding. Therefore, FEM could be an appropriate approach for studying the strengthening and damage behaviors of multiphase Al-based entropy alloys.

This study aims to investigate the compressive deformation behavior and predict the mechanical properties of Al-based entropy alloys using 3D microstructure-based

FE modeling. The three entropy alloys in our previous study [5], namely $Al_{93}Cu_4Zn_1Cr_1Fe_1$, $Al_{85}Cu_{11}Zn_2Cr_1Fe_1$, and $Al_{78}Cu_{18}Zn_2Cr_1Fe_1$, were deliberately chosen because they possessed widely different amounts of fcc-Al and IC phases in the microstructure, and hence, different mechanical properties. The IC networks of the three alloys were characterized using 3D visualization and reconstruction. The 3D data based on the actual microstructure were incorporated into the FE model to simulate the compressive deformation behavior and corresponding mechanical properties. Furthermore, the damage behaviors and strengthening mechanisms of Al-based entropy alloys are discussed. Finally, a strengthening model merging the Voigt and Reuss models was developed to predict the strengths of Al-based entropy alloys.

5.2 Materials and experimental procedure

Three Al-based entropy alloys were prepared in the graphite crucible of an induction-melting furnace. The melting temperature was set to 880 °C in an induction melting furnace under an Ar atmosphere. The alloying elements with various melting points were thoroughly mixed by melting and diffusion. To obtain a homogeneous distribution of the alloying elements, each ingot was remelted at least three times. The molten metal was finally cast into a Cu permanent mold, which was preheated at 250 °C. Details of alloy preparation and casting can be found in our previous study [5]. The chemical compositions of the three experimental alloys were analyzed using inductively coupled plasma mass spectrometry. The results are presented in Table 5.1.

Table 5.1 Chemical compositions of the experimental alloys (at.%).

Alloy	Al	Cu	Zn	Cr	Fe

Alloy 1 ($Al_{93}Cu_4Zn_1Cr_1Fe_1$)	93.18	4.34	0.45	0.99	1.04
Alloy 2 ($Al_{85}Cu_{11}Zn_2Cr_1Fe_1$)	84.26	12.04	1.88	0.83	0.99
Alloy 3 ($Al_{78}Cu_{18}Zn_2Cr_1Fe_1$)	77.44	19.04	1.72	0.79	1.01

Specimens with diameters and lengths of 8 and 12 mm, respectively, were machined for compression tests. Compression tests were conducted at room temperature using a Gleeble 3800 thermomechanical simulator unit with a strain rate of 10^{-4} s^{-1} according to the ASTM E9–09 standard. To ensure the reproducibility of the results, a minimum of two specimens were tested for each alloy. The microstructures of the polished samples were observed by SEM (JEOL JSM-6480LV).

To visualize the spatial distribution of the phases, 3D reconstruction was conducted using a sequence of two-dimensional (2D) SEM images obtained in the vertical direction through manual serial sectioning. Mounted samples were ground and polished for observation. Vickers indentation marks were made on the samples to calculate the material thickness loss after each polishing cycle [30]. By adjusting the polishing parameters, the distance between each section was approximately 0.7 μm. Over 30 images were captured for each alloy during the spatial reconstruction.

Fig. 5.1 shows typical SEM images of the top surface of the reconstructed volume for Alloys 1–3. In each alloy, the three main regions, marked A, B, and C, were identified as the fcc-Al, Al_2Cu, and $Al_{45}Cr_7$ phases, respectively. Region D in Alloy 1 corresponds to the Al_7Cu_2Fe phase [5]. Because of the small amount of Al_7Cu_2Fe (1.56 vol.%) and its similarity to Al_2Cu in terms of properties, it was treated as Al_2Cu in the following process. The images were aligned and cut to obtain continuous changes in the ICs in a rectangular space. The processed SEM images were subsequently imported

into the image analysis software, ImageJ. The Weka segmentation plugin was employed to classify and assign a uniform color to each phase within the SEM images, accommodating variations in brightness and contrast, as shown in Fig. 5.2. The distinct dark, gray, and bright regions are denoted as A, B, and C, respectively, and correspond to the fcc-Al, Al_2Cu, and $Al_{45}Cr_7$ phases, respectively. This labeling follows the same pattern as shown in Fig. 5.1. The unified color of each phase facilitates the recognition of various phases in the subsequent 3D rendering [31, 32].

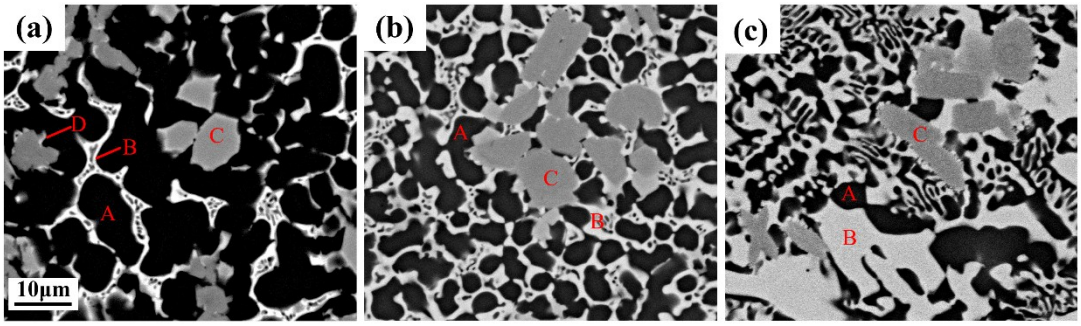

Fig. 5.1 SEM images of (a) Alloy 1, (b) Alloy 2, and (c) Alloy 3.

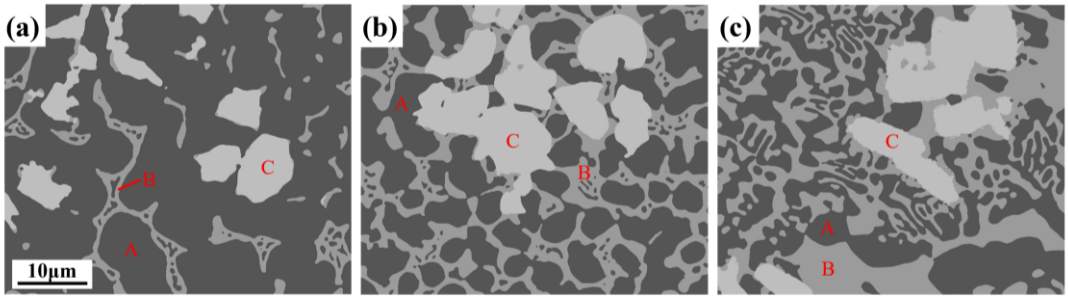

Fig. 5.2 Corresponded images of Fig. 5.1 processed by ImageJ software to assign a uniform color to each phase, (a) Alloy 1, (b) Alloy 2, and (c) Alloy 3.

The 3D reconstruction and numerical simulation processes are illustrated in Fig. 5.3. A series of processed images orthogonal to the Z-direction was imported into the 3D visualization software Mimics [27]. These images were stacked to generate a 3D virtual model, which was then used to analyze the spatial distribution of the phases.

This model represents only the shells of 3D particles. It was subsequently exported into the pre-processor FE meshing software 3-matic to create volume meshes with an element type of 4 nodes tetrahedral (Tet4). Finally, the model was imported into the commercial FE analysis software Abaqus for FEM simulation.

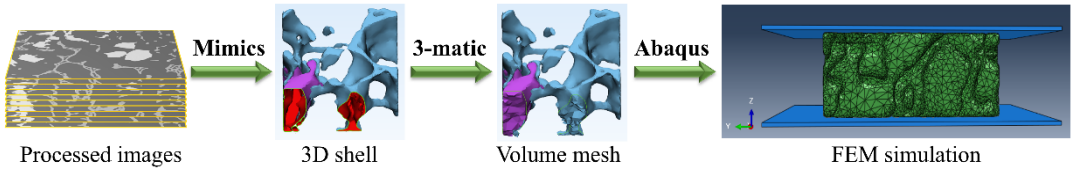

Fig. 5.3 Flow chart for the 3D reconstruction and numerical simulation process.

5.3 Results and discussion

5.3.1 Microstructural characterization from 3D visualization

The spatial distributions of the phases in Alloys 1–3 are shown in Figs. 5.4–5.6. A total volume of 50 × 40 × 20 μm^3, representing the typical phase morphology and distribution, was reconstructed for each alloy. The purple, yellow, and cyan blocks represent the fcc-Al, Al_2Cu, and $Al_{45}Cr_7$ phases, respectively. The volume fractions of each phase obtained from the spatial structures in Figs. 5.4–5.6 are listed in Table 5.2. These results are very close to those obtained from numerous 2D images that cover a wide range of regions of the alloys [5], confirming the reliability of the 3D reconstruction.

The Cu content in Alloys 1–3 increased from 4.34 to 19.04 at.%, as indicated in Table 5.1. Consequently, the volume fraction of Al_2Cu in Alloys 1–3 increased significantly. As shown in Figs. 5.4c, 5.5c, and 5.6c, the Al_2Cu skeleton becomes progressively robust. The interconnectivity of the Al_2Cu skeleton was calculated by

dividing the volume occupied by the largest object by the total volume of Al_2Cu [33]. In Alloys 1–3, the interconnectivities of Al_2Cu were 0.950, 0.998, and 0.999, respectively. It has been reported that higher interconnectivity enables a hard IC network to carry more load from the matrix, resulting in higher strength [25, 34].

Because of the similar Cr content in Alloys 1–3, the volume fraction of the $Al_{45}Cr_7$ phase was close in each alloy (approximately 10%). The $Al_{45}Cr_7$ blocks are independently dispersed without significant interconnectivity. However, they are well connected to the Al_2Cu skeleton, as shown in Figs. 5.4b, 5.5b, and 5.6b, forming a complete IC network.

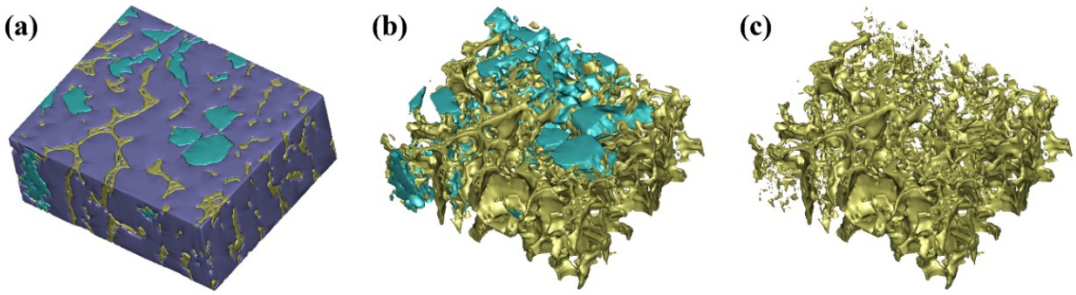

Fig. 5.4 3D phase distribution in Alloy 1: (a) all phases, (b) Al_2Cu and $Al_{45}Cr_7$ phases, and (c) Al_2Cu phase.

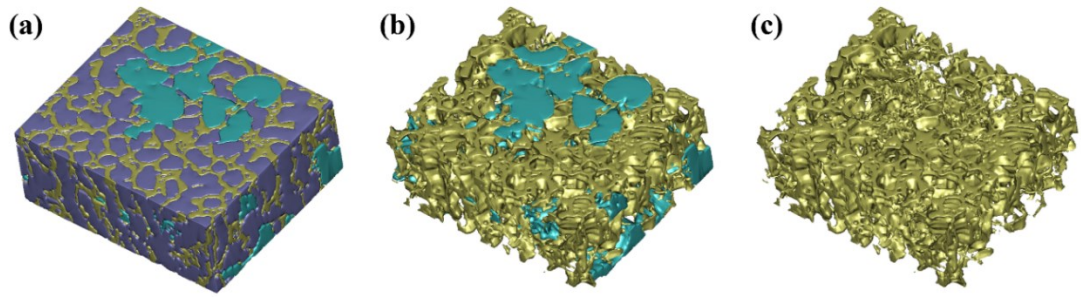

Fig. 5.5 3D phase distribution in Alloy 2: (a) all phases, (b) Al_2Cu and $Al_{45}Cr_7$ phases, and (c) Al_2Cu phase.

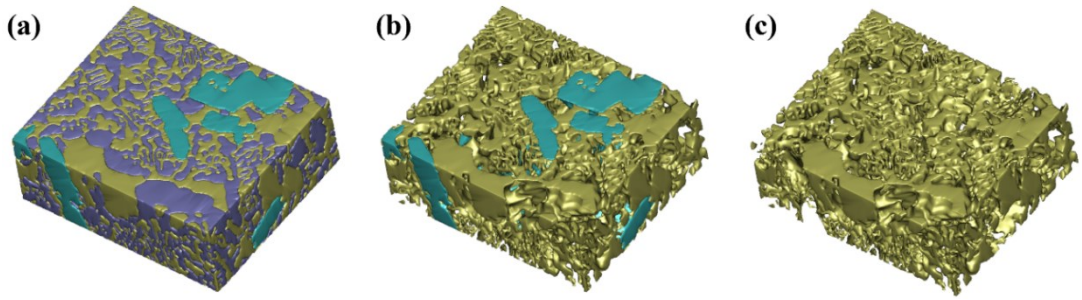

Fig. 5.6 3D phase distribution in Alloy 3: (a) all phases, (b) Al_2Cu and $Al_{45}Cr_7$ phases, and (c) Al_2Cu phase.

Table 5.2 Volume fraction of each phase from 3D reconstruction in Figs. 5.4–5.6 and compared to 2D quantification.

Alloy	Phase type	Volume fraction, vol.%	
		From 3D volume	From 2D quantification [5]
Alloy 1	fcc-Al	74.25	74.74
	Al_2Cu + Al_7Cu_2Fe	15.39	16.16
	$Al_{45}Cr_7$	10.36	9.10
Alloy 2	fcc-Al	51.99	55.75
	Al_2Cu	36.47	34.52
	$Al_{45}Cr_7$	11.54	9.73
Alloy 3	fcc-Al	32.69	31.58
	Al_2Cu	54.90	57.51
	$Al_{45}Cr_7$	12.41	10.91

5.3.2 FE simulation of compression tests

The FE models of Alloys 1–3 were constructed based on the actual phase distribution. To keep a balance between simulation speed and accuracy, a representative volume element (RVE) model measuring 14 × 14 × 7 μm³ was selected for each alloy from the 3D volume to represent their effective properties [35]. The model volume was meshed into 4-node tetrahedral elements C3D4 in 3-matic. Adaptive and uniform remeshing were adopted to generate a good-quality mesh with a

finer mesh between the interfaces, which could help better capture and transfer deformation between phases. The total number of volumetric elements was approximately 100,000.

The volumetrically meshed models were subsequently imported into Abaqus to simulate the compression tests. Fig. 5.7 shows an example of the mesoscale volume mesh for the FE model of Alloy 2. The top and bottom plates were defined as rigid bodies, wherein the bottom plate was fixed, and force was applied to the top plate to compress the RVE model along the Z-axis.

The material property of each phase was set as isotropic hardening, which follows the von Mises-type elastoplastic constitutive law, indicating a strain-hardening behavior after the phase passes the yield stage. The density ρ of each phase is calculated based on Eq. 1 and the corresponding phase chemical compositions reported in a previous study [5].

$$P = \frac{\sum_{i=1}^{n} c_i A_i}{\sum_{i=1}^{n} c_i A_i / \rho_i} \quad (1)$$

where c_i, A_i, and ρ_i are the atomic percentage, atomic weight, and density of the i^{th} element in the n-element constitution phase.

Table 5.3 provides the values of the Young's modulus and Poisson's ratio to describe the elastic deformation. To capture plastic deformation accurately, a set of points derived from the strain-stress curves of each phase were incorporated based on previous studies [36-40]. The purpose of inputting these points was to establish precise hardening laws and enhance the simulation of material behavior during plastic

deformation. The initial point serves to delineate the commencement of plastic deformation in the material, signifying the attainment of yield strength with zero plastic strain, and the concluding point encapsulates the fully plastic stage, indicating the achievement of compressive strength. The inclusion of a greater number of these points results in a more precise depiction of plastic hardening behavior. Table 5.3 lists the yield and compressive-strength inputs for each phase.

The fracture strain of each phase was defined as the damage initiation criterion in Table 5.3. During simulation, when the equivalent strain reaches the fracture strain, damage evolution will be triggered, the stress tensor σ will be degraded from the undamaged stress tensor $\bar{\sigma}$ (Eq. 2), and stress relaxation will occur [41].

$$\sigma = (1 - D)\bar{\sigma} \tag{2}$$

where D is the scalar damage variable, which is determined by the effective plastic displacement $\bar{u}^{pl}$ and the specified effective plastic displacement at failure $\bar{u}_f^{pl}$, which can be calculated based on the characteristic length of element L and equivalent plastic strain at damage initiation $\bar{\varepsilon}_0^{pl}$ and failure $\bar{\varepsilon}_f^{pl}$ [41]:

$$\bar{u}_f^{pl} = L(\bar{\varepsilon}_f^{pl} - \bar{\varepsilon}_0^{pl}) \tag{3}$$

When $\bar{u}^{pl} = \bar{u}_f^{pl}$, D is 1, and the material loses its load-carrying capacity, leading to the deletion of the elements. However, unlike in the tensile test, in the actual compression test, the failed elements do not disappear but remain inside the material

and may even contribute to the stress during further compression. Therefore, the value of $\bar{u}_f^{pl}$ used for the simulation was deliberately set to be higher.

The material properties listed in Table 5.3 were obtained from previous studies [36-40, 42-44]. However, given the distinctive nature of newly developed materials, certain parameters are difficult to measure and are not explicitly documented in the literature. Consequently, these parameters were further optimized using a combination of experimental data and multiple simulation iterations. For instance, the fcc-Al phase contains more solute atoms than conventional Al alloys. As a result, its yield strength of 95 MPa was estimated by combining the strength of the pure Al matrix (approximately 30 MPa [36]) and the solid-solution strengthening effect (approximately 65 MPa according to [5]). Similarly, reports on the properties of $Al_{45}Cr_7$ are limited. The hardness tests performed in this study revealed that the $Al_{45}Cr_7$ phase exhibited a hardness 1.5 times that of Al_2Cu. Consequently, its strength was estimated to be approximately 1.5 times that of Al_2Cu.

An explicit solver was used to perform the quasi-static simulation. A general contact option was used for interactions on all interior surfaces, with a friction coefficient of 0.2 in the tangential behavior and hard contact for the normal behavior, to balance both computational accuracy and efficiency. To ensure that the simulation produced a quasi-static response, the ratio of kinetic energy to total energy was maintained below 5% throughout the time history output [45, 46].

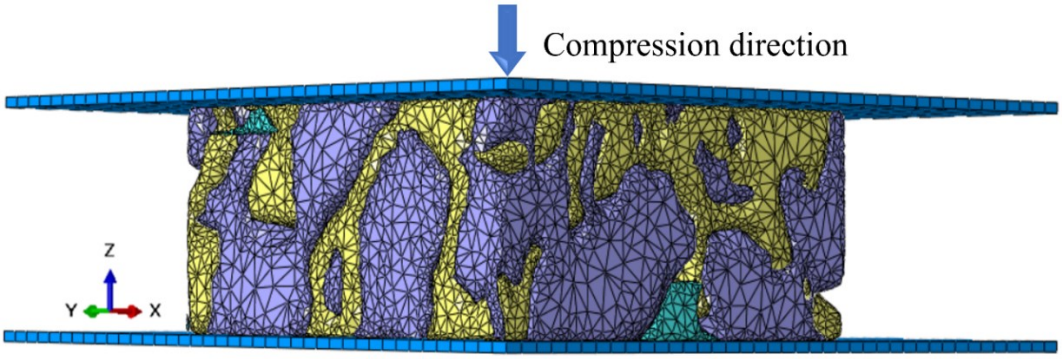

Fig. 5.7 FE modeling assembly for Alloy 2, where the purple, yellow, and cyan regions representing the fcc-Al, Al_2Cu, and $Al_{45}Cr_7$ phases, respectively.

Table 5.3 Parameters used for the FE simulation [36-40, 42-44].

Phase type	fcc-Al	Al_2Cu	$Al_{45}Cr_7$
Density, g/cm^3	2.9	4.3	3.6
Young's modulus, GPa	70 [42]	117 [43]	150
Poisson's ratio	0.33 [42]	0.32 [43]	0.30
Yield strength, MPa	95	875 [38]	1300
Compressive strength, MPa	220	975	1500
Fracture strain, %	30	0.76	0.35
$\bar{u}_f^{pl}$	0.0015	0.0002	0.0007

The compressive curves from the experimental tests and the simulated results from the RVE model of Alloys 1–3 are displayed in Fig. 5.8. Table 5.4 compares the experimental and simulated strengths. With increasing IC network content, Alloys 1–3 exhibited enhanced strengths but reduced plasticities. Alloy 3 exhibited the highest yield strength (YS) and compressive strength among the tested alloys. The measured values were 351 and 589 MPa, and the predicted values were 366 and 581 MPa, respectively. Notably, these alloys are cast alloys that do not undergo heat treatment or work hardening, and they differ from conventional heat-treatable wrought Al alloys in

their high strengths [36]. Good agreement is achieved between the experimental and FE simulation results, indicating the acceptable accuracy of the FE analysis.

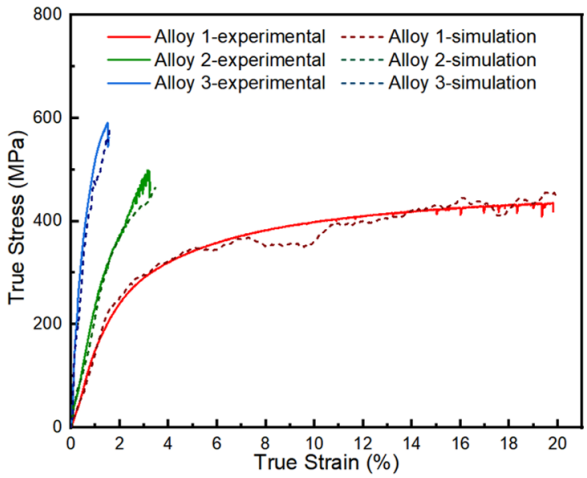

Fig. 5.8 True strain-stress curves of experimental and simulation results of Alloys 1–3.

Table 5.4 Experimental and simulated strengths of Alloys 1–3.

Alloys	Yield strength, MPa		Compressive strength, MPa	
	Experiment	Simulation	Experiment	Simulation
Alloy 1	218	237	432	448
Alloy 2	258	266	498	462
Alloy 3	351	366	589	581

5.3.3 Structural efficiency of IC network

The analysis of the local stress during the FE simulation can provide valuable insights into the deformation behavior of the different phases. Fig. 5.9 shows the distribution of local stress in Alloy 1 at an overall strain of 3%. The main body, displayed in blue in Fig. 5.9a, primarily corresponds to the fcc-Al phase, indicating the low stress carried by this soft phase. Meanwhile, the IC network is predominantly depicted in green and red (Fig. 5.9b), indicating that the IC network carried a

significantly higher level of stress than the fcc-Al phase. This suggests that during deformation, the Al_2Cu and $Al_{45}Cr_7$ phases, which have higher strengths than the fcc-Al phase, acted as stress bearers. Comparing Figs. 5.9b and 5.9c reveals that the hardest $Al_{45}Cr_7$ phase experienced the highest stress load.

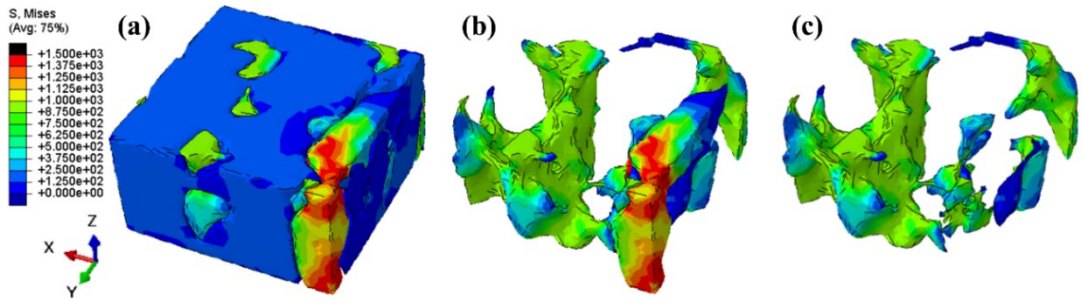

Fig. 5.9 Distribution of local stress in Alloy 1 at a total strain of 3%: (a) all phases, (b) Al_2Cu and $Al_{45}Cr_7$ phases, and (c) Al_2Cu phase.

To intuitively reflect the structural efficiency of the IC network on strengthening, a compressive simulation of a single fcc-Al structure in Alloy 1 is performed, as depicted in Fig. 5.10a. A comparison of the compressive curves between all the phases and the single fcc-Al phase is presented in Fig. 5.10b. Without the reinforcement provided by the ICs, the YS of the alloy decreased from 237 to 97 MPa, indicating the importance of the IC network in strengthening, which resulted in a strength improvement of 144%. The stress differences between the two curves at the total strains of 2% and 8% were measured to be 142 and 183 MPa, respectively. This suggests that the IC network primarily exerts a strengthening effect during the early stages of deformation. As the compression progresses, the reinforcing efficiency gradually decreases. The fluctuations in stress, as marked by the arrows in Fig. 5.10b, are a result of the relaxation of the concentrated stress owing to the local damage of the ICs, which is discussed in Section 3.4.

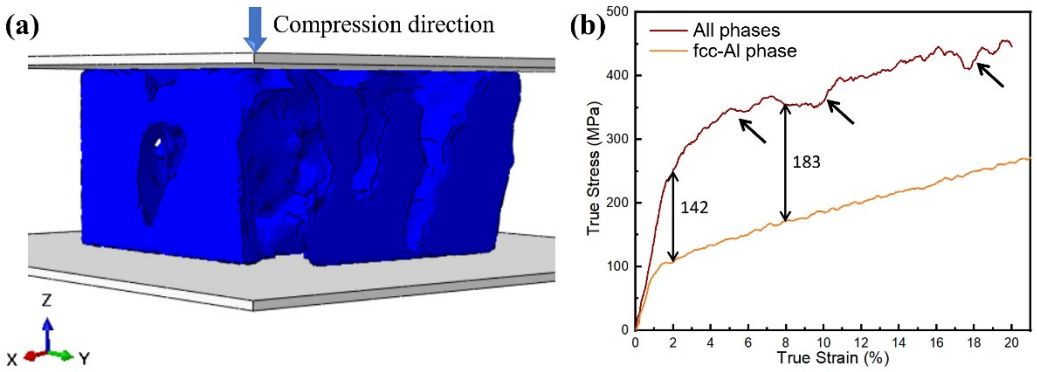

Fig. 5.10 (a) Compression simulation on single fcc phase and (b) simulated true strain-stress curves of overall phases and single fcc-Al phase in Alloy 1.

Fig. 5.11 shows the distribution of local stress on the cross-sectional area of Alloy 3. The interconnected structures in green and orange represent the Al_2Cu phase in the eutectic morphology, whereas the remaining blue and cyan regions correspond to the fcc-Al phase. Because the IC network is the main stress carrier, the Al_2Cu phase exhibits a higher stress level than the fcc-Al phase (Fig. 5.11a). As the deformation increases (Fig. 5.11b and c), a more orange/red color appears in the Al_2Cu regions, indicating increasing stress endured by the Al_2Cu phase. The sharp corners of the Al_2Cu phase tend to undergo higher stress, as indicated by the white arrows in Fig. 5.11a. This is because a sharp morphology has been reported to be favorable for sensing high stress concentrations [47]. As indicated by the black arrows in Fig. 5.11b, when plastic deformation occurs in fcc-Al, a higher stress in the fcc-Al phase is detected around the reinforcing Al_2Cu phase. During compression, the hard Al_2Cu phase restricts the local deformation of the surrounding fcc-Al matrix, resulting in the buildup of high stress near the interface [16]. Subsequently, this higher stress extends to the remaining portion of the fcc-Al, as indicated by the black arrows in Fig. 5.11c. Therefore, the IC network plays an important role in determining the mechanical properties, which not

only act as a stress carrier during deformation but also induces stress accumulation in the surrounding fcc-Al phase.

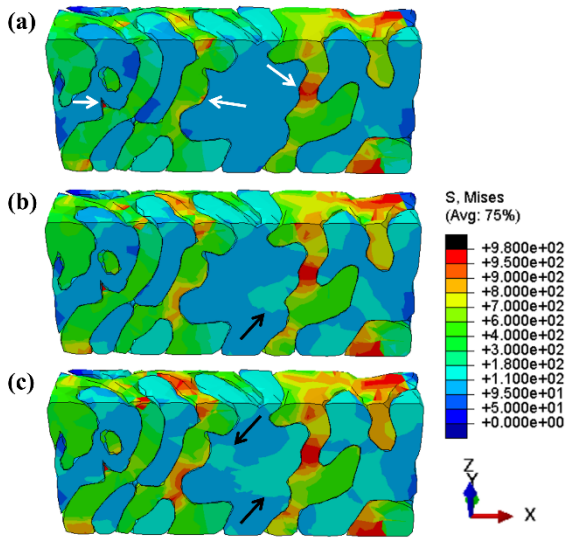

Fig. 5.11 Distribution of local stress in Alloy 3 of fcc-Al and Al_2Cu phases at a total strain of (a) 0.5%, (b) 0.7%, and (c) 0.9 %. The green and red colors represent the Al_2Cu phase, and the remaining blue and cyan regions correspond to the fcc-Al phase.

5.3.4 Damage of IC network

As shown in Fig. 5.10b, the spatial interconnection within the IC network served as the primary strengthening mechanism at low strains; however, its strengthening effectiveness decreased as the strain increased. The fcc-Al matrix exhibits excellent plasticity, in contrast to the brittle nature of the ICs. During the early deformation stage, the strain magnitude is insufficient to induce deformation incompatibility. This indicates that the limited deformation capacity of the ICs allowed them to conform to the deformation of the fcc-Al phase. However, rigid ICs cannot deform compatibly at large deformations, leading to damage to the IC network.

Fig. 5.12a depicts the local stress distribution of Al_2Cu in Alloy 1 at an overall strain of 1%. Stress concentration initially appears in the thin sections of the IC network, as indicated by the black arrows. These regions are the sites where damage first occurs, as shown in Fig. 5.12b. However, owing to the limited scale of damage, this does not lead to the ultimate failure of the alloy. Once structural breakage occurs, the local stress in the thin sections decreases owing to relaxation [35], allowing the deformation of the alloy to continue. During compression, fragile sections were fragmented into multiple pieces and flowed through the Al matrix to coordinate the overall deformation [16]. Therefore, Alloy 1 could reach a high plasticity of ~20%. However, structural damage can alleviate local stress, causing a reduction in the hardening rate, leading to the decreased strengthening efficiency [48]. Furthermore, the damage to larger particles can result in the dissipation of concentrated stress over a larger scale, contributing to noticeable stress fluctuations, as depicted in Fig. 5.10b.

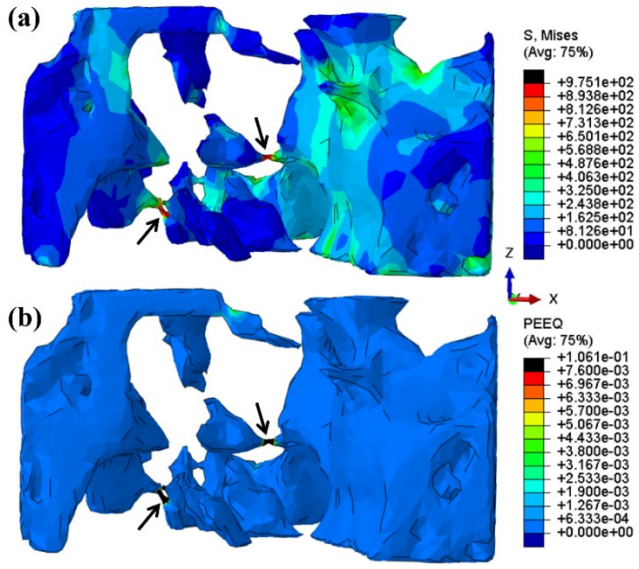

Fig. 5.12 Distribution of (a) local stress at a total strain of 1% and (b) local strain at a total strain of 1.1% of Al_2Cu phase in Alloy 1.

Under compressive loading, the initiation of alloy failure occurs primarily because of the presence of large, hard particles [16, 25]. Fig. 5.13 presents the SEM images of the deformed Alloy 1. Unlike the Al_2Cu network, which comprises thin sections, $Al_{45}Cr_7$ always exists in bulk form and is stiffer than the Al_2Cu phase, as shown in Table 5.3. Particle breakage was predominantly observed in the large bulk of $Al_{45}Cr_7$ (Fig. 5.13a). The enlarged view in Fig. 5.13b provides more details. Al_2Cu also undergoes breakage, as indicated by the white arrows in Fig. 5.13b. The breakage of the thin sections appeared in a localized area without causing additional damage to the matrix. However, the breakage of large-sized $Al_{45}Cr_7$ bulks results in the further development of cracks at the interface between the fcc-Al and $Al_{45}Cr_7$ phases, as indicated by the yellow arrow in Fig. 5.13b. This breakage could potentially serve as the initial site for large cracks and ultimately lead to alloy failure through void initiation, propagation, and coalescence [47].

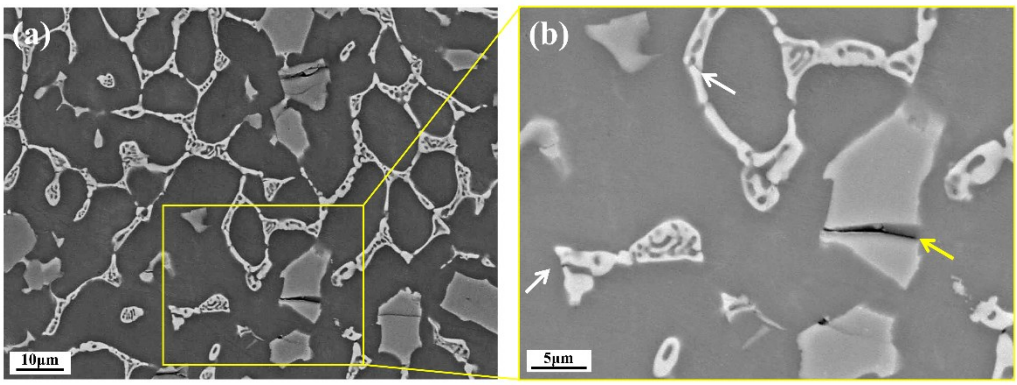

Fig. 5.13 SEM images of broken particles in the deformed Alloy 1.

As the Cu content increased from Alloy 1 to Alloy 3, the volume fraction of the Al_2Cu phase increased, along with the appearance of more robust bulks. This significantly accelerates the alloy failure process, resulting in reduced plasticity. Fig.

5.14 depicts the local strains within the IC network in Alloy 3 during deformation. In the early stages of deformation, phase damage is first observed in the $Al_{45}Cr_7$ particles, as indicated by the arrows in Fig. 5.14b, primarily because of their higher brittleness. Alloy failure ultimately occurs when cracks propagate throughout the material, as shown in Fig. 5.14c–d.

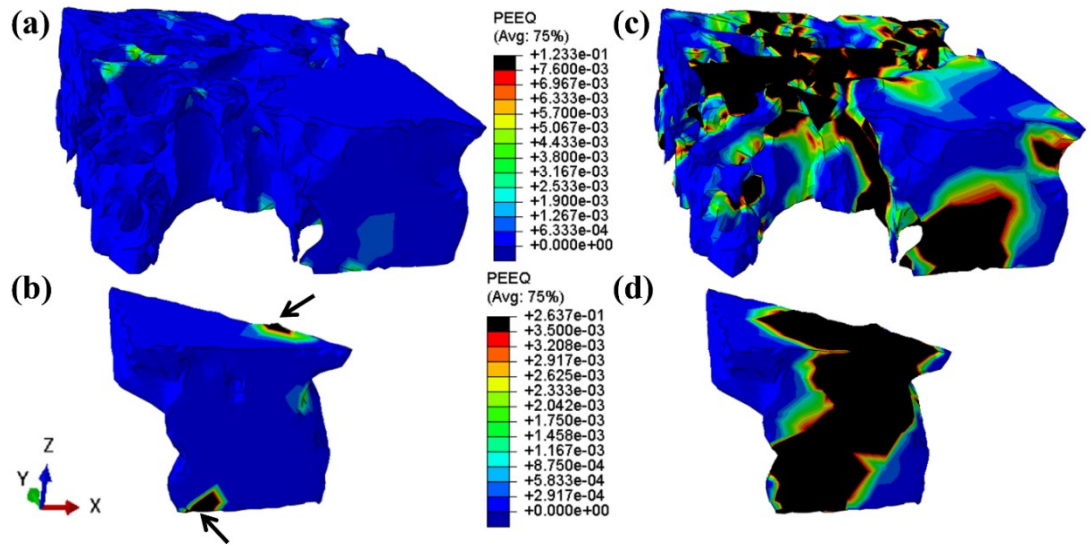

Fig. 5.14 Distribution of local strain of (a, c) Al_2Cu and (b, d) $Al_{45}Cr_7$ phases in Alloy 3 at a total strain of (a, b) 0.05% and (c, d) 1.7%.

5.3.5 Strengthening model of Al-based entropy alloys

During FE simulation results revealed the strain–stress distribution during deformation, which predicted the yield and compressive strengths of the alloys based on the material properties of the individual phases. However, the simulation requires the actual microstructure. The prediction of the overall mechanical performance of multicomponent alloys is important in material design. Consequently, building on the aforementioned simulation findings, the subsequent discussion pursues the further

exploration of a simplified strengthening model to contribute positively to the advancement of alloy development.

For composite materials, the rule of mixtures (ROM) is an intuitive method for conducting predictions by considering the volume fraction and properties of each component [49, 50]. Two ROM methods have been widely employed: Voigt and Reuss models. The Voigt model is known as a parallel model and assumes that all components have a uniform strain. The Reuss model is a series model and assumes that all components have uniform stress. The results obtained from the Voigt and Reuss models can be used to represent the upper and lower bounds of the true values [35].

For studies on multiphase alloys, the Voigt model has been widely adopted to simplify the analysis of the strengthening mechanism [23, 25, 51]. However, as discussed in Sections 3.3 and 3.4, different phases do not experience uniform strain and stress during deformation owing to the significant property differences among the various phases or variations in morphology. Obviously, a single Voigt or Reuss model is not accurate for analyzing strengthening mechanisms. Consequently, the two models were jointly employed in this study, and it was discovered that the true material strengths were related to the two calculated values. The following expressions are used to calculate the YS (σ_y) and compressive strength (σ_m) of Alloys 1–3 by Voigt and Reuss models [49].

$$\sigma_y^V = f_{fcc-Al}\sigma_{y-fcc-Al} + f_{Al_2Cu}\sigma_{y-Al_2Cu} + f_{Al_{45}Cr_7}\sigma_{y-Al_{45}Cr_7} \quad (4)$$

$$\sigma_y^R = \frac{1}{\frac{f_{fcc-Al}}{\sigma_{y-fcc-Al}} + \frac{f_{Al_2Cu}}{\sigma_{y-Al_2Cu}} + \frac{f_{Al_{45}Cr_7}}{\sigma_{y-Al_{45}Cr_7}}} \quad (5)$$

$$\sigma_m^V = f_{fcc-Al}\sigma_{m-fcc-Al} + f_{Al_2Cu}\sigma_{m-Al_2Cu} + f_{Al_{45}Cr_7}\sigma_{m-Al_{45}Cr_7} \quad (6)$$

$$\sigma_m^R = \frac{1}{\frac{f_{fcc-Al}}{\sigma_{m-fcc-Al}} + \frac{f_{Al_2Cu}}{\sigma_{m-Al_2Cu}} + \frac{f_{Al_{45}Cr_7}}{\sigma_{m-Al_{45}Cr_7}}} \quad (7)$$

where f_{fcc-Al}, f_{Al_2Cu}, and $f_{Al_{45}Cr_7}$ are the volume fractions of the fcc-Al, Al_2Cu, and $Al_{45}Cr_7$ phases, respectively; $\sigma_{y-fcc-Al}$, σ_{y-Al_2Cu}, and $\sigma_{y-Al_{45}Cr_7}$ are the YS of the fcc-Al, Al_2Cu, and $Al_{45}Cr_7$ phases, respectively; and $\sigma_{m-fcc-Al}$, σ_{m-Al_2Cu}, and $\sigma_{m-Al_{45}Cr_7}$ are the compressive strengths of the fcc-Al, Al_2Cu, and $Al_{45}Cr_7$ phases, respectively.

According to Eqs. 4–7 and Tables 5.2–5.3, the calculated and experimental YS and compressive strengths based on the aforementioned two models are plotted in Fig. 5.15. The experimental results were consistently within the range of the Voigt and Reuss results, which were calculated based on the strengths of the individual phases. This confirms the credibility of the FE simulation. As shown in Fig. 5.15a, the experimental YS values aligned more closely with the Reuss model. Additionally, with a decrease in the fcc-Al content from Alloy 1 to Alloy 3, the deviation from the Voigt model increased. As shown in Fig. 5.15b, the compressive strengths are closely aligned with the Voigt model for Alloy 1, and the correspondence gradually shifts towards the Reuss model for Alloys 2 and 3.

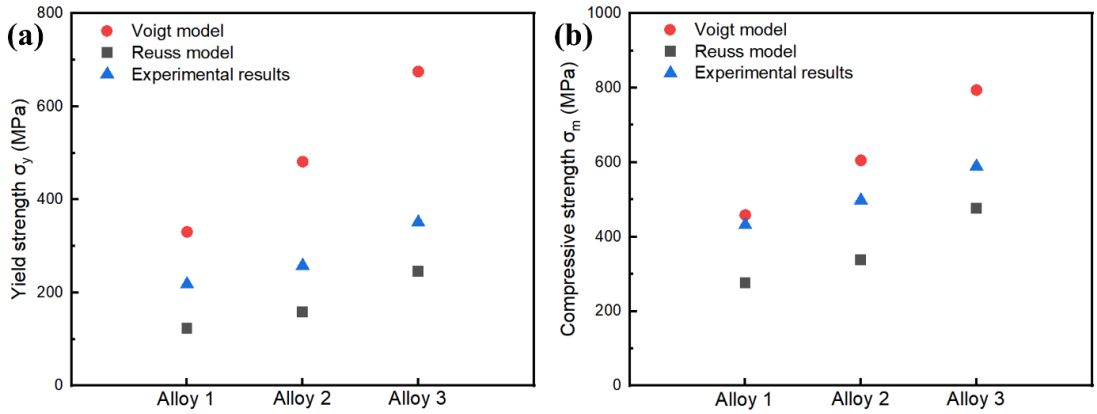

Fig. 5.15 (a) YS and (b) compressive strengths calculated from the Reuss and Voigt models and obtained from experimental results.

Combined with the FE simulation results, it was revealed that the soft fcc-Al phase contributed to the main strain in the early stage of deformation. When the σ_y was measured, fcc-Al had entered the plastic regime with a relatively large strain, while the hard phases started to have limited deformation [48]. As the soft fcc-Al content decreases from Alloy 1 to Alloy 3, this phase experiences a higher strain at the yield point in all three alloys, as shown in Fig. 5.16. Across Fig. 5.16a–5.16c, the proportion in green and orange colors, which represent higher strains, gradually increases. This indicates that the reduced volume of the fcc-Al phase led to a more uneven distribution of strain at the yield point, leading to a deviation in the YS results from the Voigt model (uniform strain).

As the compression proceeds, the thin IC network may break to coordinate the overall deformation. Therefore, Alloy 1, which possessed a large proportion of the soft fcc-Al phase and a thin IC network structure, displayed high plasticity and relatively uniform strain when obtaining compressive strength. The stress distribution can be highly uneven owing to the diverse properties of different phases, as shown in Fig. 5.9.

Consequently, the true strength could be closer to that of the Voigt model (uniform strain) compared with the Reuss model (uniform stress) in Alloy 1. However, with a decrease in the fcc-Al content, the IC network in Alloys 2–3 grew stronger. Coordinated deformation becomes increasingly difficult, and the breakage of the robust IC network can quickly lead to the failure of the alloy, resulting in a deviation of the true compressive strength from the Voigt model.

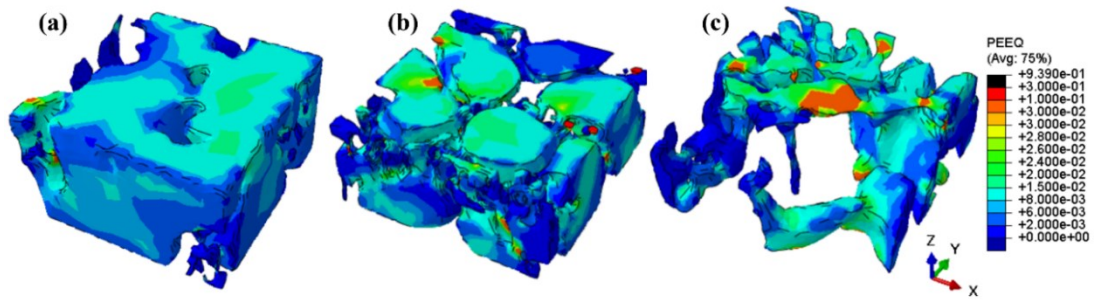

Fig. 5.16 Distribution of local strain of fcc-Al phase at yield point of (a) Alloy 1, (b) Alloy 2, and (c) Alloy 3.

Therefore, it can be seen that the true values of σ_y and σ_m were related to the Reuss value σ^R, Voigt value σ^V, as well as the volume fraction of the fcc-Al phase. Specifically, with increasing fcc-Al content, the difference between the true value and the Voigt model increases. By studying the positions of the various points in Fig. 5.15, we propose that the correlation can be quantitatively described by the following expressions:

$$\sigma_y = \frac{f_{fcc-Al}\sigma_y^V + \sigma_y^R}{1 + f_{fcc-Al}} \tag{8}$$

$$\sigma_m = f_{fcc-Al}\sigma_m^V + (1 - f_{fcc-Al})\sigma_m^R \tag{9}$$

Using the empirical equations in Eqs. 8–9, the theoretical strengths of Al-based entropy alloys can be predicted. Table 5.5 lists the theoretical σ_y and σ_m of Alloys 1–3, which showed a slight deviation from the experimental results but no more than 6.2%, indicating the accuracy of the predictive model. In collaboration with phase thermodynamic predictions such as Thermal-Calc, a strengthening model using Eqs. 4–9 can give the first estimation of the mechanical properties of the new Al-based entropy alloys, which is expected to facilitate the alloy development.

Table 5.5 Predicted strengths and their deviations with experimental data using Eqs. 8–9 in Alloys 1–3.

Alloys	Yield strength σ_y		Compressive strength σ_m	
	Theoretical results, MPa	Deviation	Theoretical results, MPa	Deviation
Alloy 1	212	2.8%	412	4.6%
Alloy 2	274	6.2%	487	2.2%
Alloy 3	349	5.7%	577	2.0%

5.4 Conclusions

1) 3D visualization revealed a highly interconnected IC network comprising Al_2Cu and $Al_{45}Cr_7$ phases. As the Cu content increased from Alloy 1 to Alloy 3, the Al_2Cu network displayed enhanced interconnectivity and a more robust morphology.

2) The IC network is the main stress bearer during deformation. This primarily exerted a strengthening effect during the first deformation stage. As compression proceeded, the reinforcing efficiency gradually diminished owing to damage to the ICs.

3) Thin sections in the Al_2Cu network were the weak sites where stress concentration and damage first occurred. However, because of their presence, alloys can exhibit relatively coordinated deformations and extended plasticity. The breakage of large particles accounts for the final alloy failure.

4) As the content of soft fcc-Al decreased from Alloy 1 to Alloy 3, causing a growing nonuniform strain distribution in the alloys, the deviation of the experimental results from the widely adopted Voigt model increased.

5) Building on the FE simulation findings, a simplified strengthening model combining the Voigt and Reuss models was proposed in this study to predict the mechanical properties. The small deviation between the predicted and experimental results indicates its accuracy in assessing the strengths of Al-based entropy alloys.

References

[1] T. Dursun, C. Soutis, Recent developments in advanced aircraft aluminium alloys, Mater. Des. (1980-2015) 56 (2014) 862-871, https://doi.org/10.1016/j.matdes.2013.12.002.

[2] A. Shyam, S. Roy, D. Shin, J.D. Poplawsky, L.F. Allard, Y. Yamamoto, J.R. Morris, B. Mazumder, J.C. Idrobo, A. Rodriguez, T.R. Watkins, Elevated temperature microstructural stability in cast AlCuMnZr alloys through solute segregation, Mater. Sci. Eng. A 765(2019) 138279, https://doi.org/10.1016/j.msea.2019.138279.

[3] L. Cui, K. Liu, Z. Zhang, X.G. Chen, Enhanced elevated-temperature mechanical properties of hot-rolled Al–Cu alloys: effect of zirconium addition and homogenization, J. Mater. Sci. 58(27) (2023) 11424-11439, https://doi.org/10.1007/s10853-023-08728-5.

[4] P. Hu, K. Liu, L. Pan, X.G. Chen, Effect of Mg microalloying on elevated-temperature creep resistance of Al–Cu 224 cast alloys, Mater. Sci. Eng. A 851 (2022) 143649, https://doi.org/10.1016/j.msea.2022.143649.

[5] L. Cui, Z. Zhang, X.G. Chen, Development of lightweight Al-based entropy alloys for elevated temperature applications, J. Alloys Compd. 938 (2023) 168619, https://doi.org/10.1016/j.jallcom.2022.168619.

[6] K.S. Tun, P. Murugan, T.S. Srivatsan, M. Gupta, Synthesis and characterization of aluminium based multicomponent alloys, Mater. Today 46 (2021) 1210–1214, https://doi.org/10.1016/j.matpr.2021.02.066.

[7] T.Y. Ahn, J.G. Jung, E.J. Baek, S.S. Hwang, K. Euh, Temporal evolution of precipitates in multicomponent Al–6Mg–9Si–10Cu–10Zn–3Ni alloy studied by complementary experimental methods, J. Alloys Compd. 701 (2017) 660-668, https://doi.org/10.1016/j.jallcom.2017.01.183.

[8] J.M. Sanchez, I. Vicario, J. Albizuri, T. Guraya, J.C. Garcia, Phase prediction, microstructure and high hardness of novel light-weight high entropy alloys, J. Mater. Res. Technol. 8(1) (2019) 795-803, https://doi.org/10.1016/j.jmrt.2018.06.010.

[9] Y. Li, Y. Zhang, Light-weight and flexible high-entropy alloys, Engineering Steels and High Entropy-Alloys, (2020) 88-322, 10.5772/intechopen.88332.

[10] L. Cui, Z. Zhang, X. Chen, Lightweight Al-based entropy alloys: Overview and future trend, Sci. China Mater. 67 (2024) 31-46, https://doi.org/10.1007/s40843-023-2699-2.

[11] X. Yang, S.Y. Chen, J.D. Cotton, Y. Zhang, Phase stability of low-density, multiprincipal component alloys containing aluminum, magnesium, and lithium, JOM 66 (2014) 2009-2020, https://doi.org/10.1007/s11837-014-1059-z.

[12] E.J. Baek, T.Y. Ahn, J.G. Jung, J.M. Lee, Y.R. Cho, K. Euh, Effects of ultrasonic melt treatment and solution treatment on the microstructure and mechanical properties of low-density multicomponent Al70Mg10Si10Cu5Zn5 alloy, J. Alloys Compd. 696 (2017) 450-459, https://doi.org/10.1016/j.jallcom.2016.11.305.

[13] C. Ji, A. Ma, J. Jiang, Mechanical properties and corrosion behavior of novel Al-Mg-Zn-Cu-Si lightweight high entropy alloys, J. Alloys Compd. 900 (2022) 163508, https://doi.org/10.1016/j.jallcom.2021.163508.

[14] R. Li, Z. Ren, Y. Wu, Z. He, P.K. Liaw, J. Ren, Y. Zhang, Mechanical behaviors and precipitation transformation of the lightweight high-Zn-content Al–Zn–Li–Mg–Cu alloy, Mater. Sci. Eng. A 802 (2021) 140637, https://doi.org/10.1016/j.msea.2020.140637.

[15] J.M. Sanchez, I. Vicario, J. Albizuri, T. Guraya, E.M. Acuña, Design, microstructure and mechanical properties of cast medium entropy aluminium alloys, Sci. Rep. 9(1) (2019) 6792, https://doi.org/10.1038/s41598-019-43329-w.

[16] P. Biswas, D. Mandal, M.K. Mondal, Compressive failure analysis of in-situ Al-Mg2Si composites: Experiment and finite element modelling, Eng. Fract. Mech. 277 (2023) 108986, https://doi.org/10.1016/j.engfracmech.2022.108986.

[17] L. Cui, Z. Zhang, X.G. Chen, Microstructure and mechanical properties of novel Al–Cu–Mg–Zn lightweight entropy alloys for elevated-temperature applications, Mater. Charact. 200 (2023) 112927, https://doi.org/10.1016/j.matchar.2023.112927.

[18] K. Matouš, M.G. Geers, V.G. Kouznetsova, A. Gillman, A review of predictive nonlinear theories for multiscale modeling of heterogeneous materials, J. Comput. Phys. 330 (2017) 192-220, https://doi.org/10.1016/j.jcp.2016.10.070.

[19] H. Daghigh Shirazi, M. Malekan, Computational Modeling of Compressive Behavior of Wire-Reinforced Bulk Metallic Glass Matrix Composites, Trans Indian Inst Met. 74 (2021) 649-658, https://doi.org/10.1007/s12666-021-02194-w.

[20] S. Katani, F. Madadi, M. Atapour, Z. Rad, Micromechanical modelling of damage behaviour of Ti–6Al–4V, Mater. Des. 49 (2013) 1016–1021, https://doi.org/10.1016/j.matdes.2013.02.021.

[21] R. Bhandari, P. Biswas, M.K. Mondal, D. Mandal, Finite element analysis of stress−strain localization and distribution in Al−4.5Cu−2Mg alloy, Trans Nonferrous Met Soc China 28 (2018) 1200–1215, https://doi.org/10.1016/S1003-6326(18)64758-2.

[22] J.N. Dastgerdi, B. Anbarlooie, A. Miettinen, H. Hosseini-Toudeshky, H. Remes, Effects of particle clustering on the plastic deformation and damage initiation of particulate reinforced composite utilizing X-ray CT data and finite element modelling, Compos. B Eng. 153 (2018) 57–69, https://doi.org/10.1016/j.compositesb.2018.07.027.

[23] B. Zhang, S. Gavras, A.V. Nagasekhar, C.H. Cáceres, M.A. Easton, The strength of the spatially interconnected eutectic network in HPDC Mg-La, Mg-Nd, and Mg-La-Nd alloys, Metall. Mater. Trans. A 45 (2014) 4386-4397, https://doi.org/10.1007/s11661-014-2416-9.

[24] N. Chawla, R.S. Sidhu, V.V. Ganesh, Three-dimensional visualization and microstructure-based modeling of deformation in particle-reinforced composites, Acta Mater. 54(6) (2006) 1541-1548, https://doi.org/10.1016/j.actamat.2005.11.027.

[25] J.G.S. Macías, T. Douillard, L. Zhao, E. Maire, G. Pyka, A. Simar, Influence on microstructure, strength and ductility of build platform temperature during laser powder bed fusion of AlSi10Mg, Acta Mater. 201 (2020) 231-243, https://doi.org/10.1016/j.actamat.2020.10.001.

[26] Y. Shao, Z. Zhang, W. Guo, X. Tang, S. Lü, X. Chen, S. Wu, Development of Zr-based metallic glass matrix composites with hybrid reinforcing structures, Intermetallics 137 (2021) 107294, https://doi.org/10.1016/j.intermet.2021.107294.

[27] F. Liu, H. Zhao, R. Yang, F. Sun, Crack propagation behavior of die-cast AlSiMgMn alloys with in-situ SEM observation and finite element simulation, Mater. Today Commun. 19 (2019) 114-123, https://doi.org/10.1016/j.mtcomm.2019.01.009.

[28] Y. Jiang, K. Qiu, Computational micromechanics analysis of toughening mechanisms of particle-reinforced bulk metallic glass composites, Mater. Des. (1980-2015) 65 (2015) 410-416, https://doi.org/10.1016/j.matdes.2014.09.013.

[29] J.J. Williams, J. Segurado, J. Llorca, N. Chawla, Three dimensional (3D) microstructure-based modeling of interfacial decohesion in particle reinforced metal matrix composites, Mater. Sci. Eng. A 557 (2012) 113-118, https://doi.org/10.1016/j.msea.2012.05.108.

[30] C.M. Dinnis, A.K. Dahle, J.A. Taylor, Three-dimensional analysis of eutectic grains in hypoeutectic Al–Si alloys, Mater. Sci. Eng. A 392 (1–2) (2005) 440–448, https://doi.org/10.1016/j.msea.2004.10.037.

[31] C. Petit, E. Maire, S. Meille, J. Adrien, Two-scale study of the fracture of an aluminum foam by X-ray tomography and finite element modeling, Mater. Des. 120 (2017) 117-127, https://doi.org/10.1016/j.matdes.2017.02.009.

[32] J.J. Williams, K.E. Yazzie, E. Padilla, N. Chawla, X. Xiao, F. De Carlo, Understanding fatigue crack growth in aluminum alloys by in situ X-ray synchrotron tomography, Int. J. Fatigue 57 (2013) 79–85, https://doi.org/10.1016/j.ijfatigue.2012.06.009.

[33] A. Asghar, G. Requena, E. Boller, Three-dimensional rigid multiphase networks providing high-temperature strength to cast AlSi10Cu5Ni1-2 piston alloys, Acta Mater. 59 (2011) 6420–6432, https://doi.org/10.1016/j.actamat.2011.07.006.

[34] D. Amberger, P. Eisenlohr, M. Göken, On the importance of a connected hard-phase skeleton for the creep resistance of Mg alloys, Acta Mater. 60(5) (2012) 2277-2289, https://doi.org/10.1016/j.actamat.2012.01.017.

[35] A.H. Assari, Investigating the deformation behavior of hot-pressed Ti/Al/Ti laminated composite, J. Manuf. Process. 95 (2023) 369-381, https://doi.org/10.1016/j.jmapro.2023.04.026.

[36] J.G. Kaufman, Properties of Aluminum Alloys: Tensile, Creep, and Fatigue Data at High and Low Temperatures, ASM International, 1999.

[37] A. Aghabalaeivahid, M. Shalvandi, Microstructure-based crystal plasticity modeling of AA2024-T3 aluminum alloy defined as the α-Al, θ-Al2Cu, and S-Al2CuMg phases based on real metallographic image, Mater. Res. Express 8(10) (2021) 106521, https://doi.org/10.1088/2053-1591/ac2eac.

[38] A. Mehditabar, G.H. Rahimi, S.E. Vahdat, Mechanical properties of Al 25 wt.% Cu functionally graded material, Sci. Eng. Compos. Mater. 26(1) (2019) 327-337, https://doi.org/10.1515/secm-2019-0014.

[39] Y.V. Milman, D.B. Miracle, S.I. Chugunova, I.V. Voskoboinik, N.P. Korzhova, T.N. Legkaya, Y.N. Podrezov, Mechanical behaviour of Al3Ti intermetallic and L12 phases on its basis, Intermetallics 9(9) (2001) 839-845, https://doi.org/10.1016/S0966-9795(01)00073-5.

[40] Q. Li, Z. Shang, X. Sun, C. Fan, R. Su, N.A. Richter, Z. Fan, Y. Zhang, S. Xue, H. Wang, X. Zhang, High-strength and tunable plasticity in sputtered Al–Cr alloys with

multistage phase transformations, Int J Plast. 137 (2021) 102915, https://doi.org/10.1016/j.ijplas.2020.102915.

[41] SIMULIA, Abaqus Analysis User's Manual, version 2016, The Dassault Systemes, Realistic Simulation, USA, 2015. http://130.149.89.49:2080/v2016/index.html

[42] Y. Li, Y.H. Zhao, V. Ortalan, W. Liu, Z.H. Zhang, R.G. Vogt, N.D. Browning, E.J. Lavernia, J.M. Schoenung, Investigation of aluminum-based nanocomposites with ultra-high strength, Mater. Sci. Eng. A 527(1-2) (2009) 305-316, https://doi.org/10.1016/j.msea.2009.07.067.

[43] L. Song, G. Fu, H. Chen, Y. Su, First-principles study of the effect of H on elastic properties of Al2Cu, Mater. Lett. 308 (2022) 131191, https://doi.org/10.1016/j.matlet.2021.131191.

[44] S. Amirkhanlou, S. Ji, Casting lightweight stiff aluminum alloys: a review, Crit. Rev. Solid State Mater. Sci. 45(3) (2020) 171-186, https://doi.org/10.1080/10408436.2018.1549975.

[45] I.K.Mohammed, M.N. Charalambides, J.G.Williams, J. Rasburn, Modelling the microstructural evolution and fracture of a brittle confectionery wafer in compression, Innovative Food Sci. Emerg. Technol. 24 (2014) 48–60, https://doi.org/10.1016/j.ifset.2013.11.015.

[46] A. Ghamarian, H.R. Zarei, M.T. Abadi, Experimental and numerical crashworthiness investigation of empty and foam-filled end-capped conical tubes, Thin-Walled Struct. 49 (2011) 1312–1319, https://doi.org/10.1016/j.tws.2011.03.005.

[47] P. Biswas, D. Mandal, M.K. Mondal, Failures analysis of in-situ Al–Mg2Si composites using actual microstructure based model, Mater. Sci. Eng. A 797 (2020) 140155, https://doi.org/10.1016/j.msea.2020.140155.

[48] B. Zhang, A.V. Nagasekhar, X. Tao, Y. Ouyang, C.H. Cáceres, M. Easton, Strengthening by the percolating intergranular eutectic in an hpdc Mg–Ce alloy, Mater. Sci. Eng. A 599 (2014) 204-211, https://doi.org/10.1016/j.msea.2014.01.074.

[49] I.M. Daniel, O. Ishai, I.M. Daniel, I. Daniel, Engineering mechanics of composite materials (Vol. 1994). New York: Oxford University Press, 2006.

[50] H.S. Kim, On the rule of mixtures for the hardness of particle reinforced composites, Mater. Sci. Eng. A 289(1-2) (2000) 30-33, https://doi.org/10.1016/S0921-5093(00)00909-6.

[51] Z. Li, Z. Li, Z. Tan, D.B. Xiong, Q. Guo, Stress relaxation and the cellular structure-dependence of plastic deformation in additively manufactured AlSi10Mg alloys, Int J Plast. 127 (2020) 102640, https://doi.org/10.1016/j.ijplas.2019.12.003.

Chapter 6

General conclusions and recommendations

6.1 General conclusions

In this project, the development of lightweight Al-based entropy alloys for elevated temperature applications was conducted. The following critical conclusions can be drawn for this thesis:

1. A comprehensive investigation of lightweight Al-based entropy alloys was conducted. Phase formation in lightweight Al-based entropy alloys exhibits multiphase features. Intermetallic compounds (ICs) are inevitable in the alloys, while alloys solely comprising ICs tend to be excessively brittle, hindering their practical use. It has been observed that maintaining a Ω value higher than 3.95 helps avoid the alloys only comprising ICs.
2. Two series, in total eleven Al-based entropy alloys were designed and investigated. All of the alloys exhibited lightweight characteristics with density values ranging from 2.95 to 3.74 g/cm^3 and revealed multiphase features. A large quantity of ICs appeared in the as-cast microstructures. With increasing Cu and other element contents, the volume fraction of ICs increased.
3. For the first series of alloys, five Al–Cu–Mg–Zn entropy alloys were developed. The alloys exhibited high compressive strength at room temperature (RT) in an as-cast state, with yield strength (YS) ranging from 330 to 588 MPa. The main strengthening mechanisms were found to be precipitation strengthening from GP zones and fine η’ precipitates in the fcc-Al phase and ICs network strengthening.

4. During thermal exposure, the precipitates in Al–Cu–Mg–Zn entropy alloys were transformed into coarse and submicron particles, which deteriorated the mechanical behavior to varying degrees, indicating that the simultaneous addition of Mg and Zn led to the thermal instability of alloys at high temperatures (HTs). Due to the small content of fcc-Al in alloy $Al_{77}Cu_{17}Zn_3Mg_2Cr_1$, its strength slightly decreased (by less than 10%) after thermal exposure and it still retained a high strength at 300 °C among the five alloys with a YS of 199 MPa and a maximum compressive strength of 234 MPa.
5. For the second series of alloys, six Al–Cu–Zn–Cr entropy alloys were developed. Wherein, the three high-Cu alloys $Al_{78}Cu_{18}Zn_2Cr_1Fe_1$, $Al_{78}Cu_{18}Zn_1Cr_2Ti_1$, and $Al_{78}Cu_{18}Zn_1Cr_2V_1$ exhibited excellent compressive strength (> 580 MPa) with low plasticity (~1%) at RT owing to the high-volume fraction of ICs. At 300 °C, the three alloys exhibited considerably higher plasticities, and the YS values surpassed 200 MPa.
6. The ICs in all six Al–Cu–Zn–Cr alloys were heat-resistant as expected. After thermal exposure at 300 °C for 100 h, the YS values at 300 °C of the three high-Cu alloys changed negligibly and retained at the level of ~200 MPa. The results were considerably superior to those obtained for most conventional aluminum alloys. Furthermore, the excellent thermal stability of the high-Cu alloys up to 450 °C was confirmed. Combined with their high YS values, the novel lightweight entropy alloys provide promising prospects for high-temperature applications.
7. The three-dimensional visualization results revealed a closely interconnected intermetallic compound (IC) network in the Al-based entropy alloys. The IC

network was the main stress bearer during compression, and it primarily exerted the strengthening effect at the early deformation stage. Small-scale damage first took place among the thin sections and the breakage of large particles accounted for the final alloy failure.

8. A simplified strengthening model combining the Voigt and Reuss models was proposed to predict the mechanical properties. The slight deviation indicates its accuracy in assessing the strength of Al-based entropy alloys.

6.2 Recommendations

Based on the recent findings of this study, the following suggestions and recommendations for future work are given as follows:

1. Due to the high concentration of multiple elements, Al-based entropy alloys could exhibit poor liquidity and castability. Therefore, eutectic microstructure is suggested to be introduced in the alloys to improve the castability. Furthermore, for fabrication, the induction melting method is recommended as it aids in stirring the molten metals, leading to improved mixing of the elements. Multiple remelting cycles can also contribute to better compositional homogeneity.
2. Most current studies in this field of Al-based entropy alloys focus primarily on the mechanical properties at RT. This project has confirmed the significant potential of Al-based entropy alloys as lightweight structural materials for high-temperature applications. Therefore, it is recommended to shift more focus

towards developing alloys designed for HTs. In addition to compression tests, tensile properties are also suggested to be investigated for future applications.

3. Considering the inevitable occurrence of ICs in most Al-based entropy alloys, it is worthwhile to exploit their presence. By intentionally introducing heat-resistant ICs, it is possible to significantly enhance the mechanical performance of materials not only at RT but also at HTs. Meanwhile, it is recommended to maintain a Ω value higher than 3.95 to avoid the alloys comprising only ICs.
4. For Al-based entropy alloys intended for elevated-temperature applications, the simultaneous addition of Mg and Zn is not recommended due to the generation of thermally unstable precipitates. It is worth noting that when Cu also exists, a transformation of secondary phases between $MgZn_2$ and Al_2CuMg may further occur, leading to the thermal instability of the microstructure.
5. Computational approaches are further trends for effectively developing entropy alloys. The strengthening model proposed to predict the YS and compressive strength of Al-based entropy alloys can be used to predict and screen alloys when combined with the high-strength-orientated alloy design strategy. This can accelerate the alloy development process.

List of publications

1. Peer-reviewed Journal Articles

1) **L. Cui**, Z. Zhang and X.G. Chen, Development of lightweight Al-based entropy alloys for elevated temperature applications, ***Journal of Alloys and Compounds***, 938 (2023): 168619. https://doi.org/10.1016/j.jallcom.2022.168619
2) **L. Cui**, Z. Zhang and X. G. Chen, Microstructure and mechanical properties of novel Al–Cu–Mg–Zn lightweight entropy alloys for elevated-temperature applications, ***Materials Characterization***, 200 (2023): 112927. https://doi.org/10.1016/j.matchar.2023.112927
3) **L. Cui**, K. Liu Z. Zhang and X.G. Chen, Enhanced elevated-temperature mechanical properties of hot-rolled Al–Cu alloys: effect of zirconium addition and homogenization, ***Journal of Materials Science***, 58 (2023): 11424–11439. https://doi.org/10.1007/s10853-023-08728-5
4) **L. Cui**, Z. Zhang and X.G. Chen, Lightweight Al-based entropy alloys: Overview and future trend, ***Science China Materials***, 67 (2024): 31-46. https://doi.org/10.1007/s40843-023-2699-2
5) **L. Cui**, Z. Zhang and X.G. Chen, Spatial reconstruction, microstructure-based modeling of compressive deformation behavior, and prediction of mechanical properties in lightweight Al-based entropy alloys, under submission.

2. Conference papers

1) **L. Cui**, Z. Zhang, D.K. Sarkar, D. Kocaefe and X.G. Chen, A Study on Aluminum-Based Lightweight Entropic Alloys with High Strength at Elevated Temperature. In: Proceedings of the 61st Conference of Metallurgists, 2022, 413-423. https://doi.org/10.1007/978-3-031-17425-4_55

3. Scientific posters

1) **L. Cui**, Z. Zhang, X.G. Chen, Microstructure and mechanical properties of lightweight entropic aluminum alloys, ***REGAL 2020***.
2) **L. Cui**, Z. Zhang, X.G. Chen, Development of aluminum-based lightweight entropic alloys for elevated temperature applications, ***REGAL 2021***.
3) **L. Cui**, Z. Zhang, X.G. Chen, Development of lightweight Al–Cu–Zn–Mg entropic alloys with high strength at elevated temperature, ***REGAL 2022***. (**Second prize**)

4) **L. Cui**, Z. Zhang, X.G. Chen, Enhanced elevated-temperature mechanical properties of hot-rolled Al-Cu alloys – Effect of zirconium addition and homogenization, ***REGAL 2023***. (**Second prize**)